ABSTRACT

Title of Document: AN EXAMINATION OF HYDROXYL RADICAL: OUR CURRENT UNDERSTANDING OF THE OXIDATIVE CAPACITY OF THE TROPOSPHERE THROUGH EMPIRICAL, BOX, AND GLOBAL MODELING APPROACHES

Julie Megan Nicely, Doctor of Philosophy, 2016

Directed By: Dr. Ross J. Salawitch, Department of Chemistry and Biochemistry, Department of Atmospheric and Oceanic Science, Earth System Science Interdisciplinary Center

Hydroxyl radical (OH) is the primary oxidant in the troposphere, initiating the removal of numerous atmospheric species including greenhouse gases, pollutants that are detrimental to human health, and ozone-depleting substances. Because of the complexity of OH chemistry, models vary widely in their OH chemistry schemes and resulting methane (CH_4) lifetimes. The current state of knowledge concerning global OH abundances is often contradictory. This body of work encompasses three projects that investigate tropospheric OH from a modeling perspective, with the goal of improving the tropospheric community's knowledge of the atmospheric lifetime of CH_4. First, measurements taken during the airborne CONvective TRansport of Active Species in the Tropics (CONTRAST) field campaign are used to evaluate OH in global models. A box

model constrained to measured variables is utilized to infer concentrations of OH along the flight track. Results are used to evaluate global model performance, suggest against the existence of a proposed "OH Hole" in the tropical Western Pacific, and investigate implications of high O_3/low H_2O filaments on chemical transport to the stratosphere. While methyl chloroform-based estimates of global mean OH suggest that models are overestimating OH, we report evidence that these models are actually underestimating OH in the tropical Western Pacific. The second project examines OH within global models to diagnose differences in CH_4 lifetime. I developed an approach to quantify the roles of OH precursor field differences (O_3, H_2O, CO, NO_x, etc.) using a neural network method. This technique enables us to approximate the change in CH_4 lifetime resulting from variations in individual precursor fields. The dominant factors driving CH_4 lifetime differences between models are O_3, CO, and $J(O_3 \rightarrow O^1D)$. My third project evaluates the effect of climate change on global fields of OH using an empirical model. Observations of H_2O and O_3 from satellite instruments are combined with a simulation of tropical expansion to derive changes in global mean OH over the past 25 years. We find that increasing H_2O and increasing width of the tropics tend to increase global mean OH, countering the increasing CH_4 sink and resulting in well-buffered global tropospheric OH concentrations.

AN EXAMINATION OF HYDROXYL RADICAL: OUR CURRENT UNDERSTANDING OF THE OXIDATIVE CAPACITY OF THE TROPOSPHERE THROUGH EMPIRICAL, BOX, AND GLOBAL MODELING APPROACHES

By

Julie Megan Nicely

Thesis submitted to the Faculty of the Graduate School of the
University of Maryland, College Park, in partial fulfillment
of the requirements for the degree of
Doctor of Philosophy
2016

Advisory Committee:
Professor Ross J. Salawitch, Chair
Professor Neil V. Blough
Professor Russell R. Dickerson
Professor Sheryl H. Ehrman, Dean's Representative
Adjunct Professor Thomas F. Hanisco

Dedication

I dedicate this body of work to my Grandmother, Yvonne Mathias, who has been wondering what in the world a person could be doing for so long in school. I promise that this marks the end of my schooling years!

Acknowledgements

I'd like to thank everyone who has supported me during my stay at graduate school: thanks to my advisor Ross for always driving me to be my best, setting a stellar example for how to do science ambitiously and with the utmost conscientiousness, and for allowing me to learn from your wisdom for the past 5½ years. Thanks to Tim Canty for teaching me all the fundamentals of IDL to get me off the ground with programming and for your many hours devoted to debugging and helping me work out research problems during my early years. Thanks to UMD, Goddard, NCAR, and JHU colleagues for enlightening discussions and meetings and for welcoming me into the atmospheric chemistry community, including Russ Dickerson, Glenn Wolfe, Tom Hanisco, Anne Douglass, Bryan Duncan, Luke Oman, Sarah Strode, Qing Liang, Paul Newman, Rich Stolarski, Darryn Waugh, Doug Kinnison, Jean-Francois Lamarque, Bill Randel, Laura Pan, and many others I'm probably forgetting. Thanks to my fellow students at UMD for providing a source of empathy through the process that is grad school, especially Linda Hembeck, Dan Goldberg, Dan Anderson, and Clare Flynn. Special thanks also to Dan Anderson for help revising drafts of various papers. Thanks to NASA and NSF for providing funding for the research conducted herein and to the University of Maryland Department of Chemistry and Biochemistry and Department of Atmospheric and Oceanic Science for supporting my graduate education.

And most of all, thanks to my family for unconditional support for what I do, even if you don't understand it; thanks especially to Mom, Dad, Josh, & Grandma.

Table of Contents

List of Tables

List of Figures

Chapter 1: Introduction

Atmospheric hydroxyl radical (OH), a molecule consisting of one hydrogen atom and one oxygen atom covalently bonded, is frequently termed the "detergent" of the troposphere due to its important role as an oxidant [*Levy*, 1971]. The radical's high reactivity due to possession of a single unpaired electron makes it efficient in initiating the removal of many atmospheric pollutants and greenhouse gases; however, this characteristic makes the species particularly difficult to measure using standard techniques. A typical mixing ratio of OH in the troposphere is a fraction of a part per trillion [*Wennberg et al.*, 1998], and the lifetime of OH is generally ≤ 1 s [*Abram et al.*, 2000]. While instrumentalists have developed methods that overcome these obstacles [*Brune et al.*, 1998; *Kovacs and Brune*, 2001; *Mauldin et al.*, 2001] and laboratory scientists have devoted much effort to evaluating the chemical kinetics of the myriad reactions in which OH participates [*Atkinson*, 1987; *Saunder et al.*, 1993], the onus of assimilating the current knowledge regarding OH and representing it accurately on a global scale falls to atmospheric modelers. The body of work presented here seeks to aid in the endeavor to model the oxidizing capacity of the troposphere accurately and, in doing so, glean valuable insights into the behavior of tropospheric OH in the true atmosphere.

1.1 Background

1.1.1 Motivation for Understanding Tropospheric OH

The OH radical is widely regarded as the primary oxidant in the troposphere, especially for hydrogen-containing species [*Forster et al.*, 2007; *Plumb et al.*, 2013; *Carpenter et al.*, 2014]. Atmospheric lifetimes of species ranging from biogenic hydrocarbons to the pollutants methane (CH_4), carbon monoxide (CO), and sulfur dioxide (SO_2) and stratospheric ozone-depleting substances are all determined to a large extent by concentrations of OH. Methane is the second-most important greenhouse gas after CO_2 [*IPCC*, 2013], and its sink by reaction with tropospheric OH accounts for almost 90% of its total loss [*Lelieveld et al.*, 1998]; other sinks include oxidation by bacteria in soil and reaction with OH, Cl, and $O(^1D)$ in the stratosphere. CO is an EPA criteria pollutant [*EPA*, 2015] with acute and chronic adverse effects on human health [*Raub et al.*, 2000], emitted by incomplete combustion of organic compounds, such as mobile internal combustion engines. Aside from its direct role in detrimentally affecting human health, CO also contributes to production of tropospheric ozone (O_3), another EPA criteria pollutant [*EPA*, 2015] that has deleterious effects on human health [*Bell et al.*, 2005] and vegetation [*Ellingsen et al.*, 2008]. As with CH_4, CO is lost primarily by reaction with OH in the troposphere [*Worden et al.*, 2013].

Other aspects of tropospheric O_3 production are integrally linked with the chemistry of OH. Oxidation of hydrocarbons such as isoprene, emitted by oak and other deciduous trees [*Guenther et al.*, 1993], or ethane, released during fossil fuel extraction and refinement and biomass burning [*Rudolph*, 1995], generates

hydroperoxy (HO_2) radicals that constitute one necessary ingredient for the production of O_3 [*Chameides et al.*, 1988]. In the presence of nitric oxide (NO), HO_2 is recycled back to OH, forming nitrogen dioxide (NO_2) in the process. Nitrogen dioxide, another EPA criteria pollutant [*EPA*, 2015], and NO form a class of radicals referred to as NO_x that constitutes the second ingredient necessary to produce tropospheric O_3; photolysis of NO_2 in sunlit conditions generates NO and a ground-state oxygen atom, $O(^3P)$, which readily reacts with ambient O_2 to produce O_3 [*Atkinson and Lloyd*, 1984]. The role of OH in this process was pointed out in the initial oxidation of CO or a hydrocarbon such as isoprene; however, OH is also involved with the removal of NO_x radicals. Reaction of OH with NO_2 on a third body forms nitric acid (HNO_3), which is removed from the atmosphere by wet or dry deposition [*Horii et al.*, 2006]. Furthermore, production of O_3 can also be limited by the self-reaction of HO_x radicals (=OH+HO_2). The reaction of OH and HO_2 to form H_2O and O_2 as well as the reaction of HO_2 and HO_2 to form H_2O_2 and O_2 cause the termination of the radical cycle that drives O_3 pollution events.

The link between OH and O_3 is not only important in the troposphere; implications of OH chemistry also affect stratospheric O_3 (i.e., the "ozone layer"). While it is an interesting phenomenon that the cycling of HO_x radicals in the stratosphere actually serves to reduce concentrations of O_3, I will instead focus on the aspects of OH chemistry that occur within the troposphere with subsequent effects on stratospheric O_3. The role of halogens in driving stratospheric O_3 loss is widely reported in the literature [*Molina and Rowland*, 1974; *McElroy et al.*, 1986]. Following the ban on chlorofluorocarbons (CFCs) implemented by the Montreal

Protocol and its amendments, the decline in the atmospheric burden of halogenated compounds has resulted in the growing relative importance of smaller sources of chlorine and bromine to the stratosphere. For example, the degree to which very short-lived (VSL) bromocarbons, including CH_2Br_2 and $CHBr_3$, account for the total amount of bromine reaching the stratosphere is a topic of much discussion in the literature [*Gettelman et al.*, 2009; *Brioude et al.*, 2010; *Salawitch et al.*, 2010; *Carpenter et al.*, 2014; *Liang et al.*, 2014]. Because the atmospheric lifetimes of VSL compounds are on the cusp of being long enough for transport to the stratosphere to occur, the determining factors in whether or not they are significant contributors to the stratospheric halogen budget include the concentration of OH.

The Montreal Protocol is also responsible for a rise, in atmospheric abundances and in scientific interest, for another class of compounds that rely on OH for removal. The banning of CFCs has led to production of the replacement compounds hydrochlorofluorocarbons (HCFCs) and hydrofluorocarbons (HFCs) for use as refrigerants, propellants, solvents, and foaming agents [*UNEP*, 2010]. HCFCs still contain chlorine atoms, meaning that the species still retain some potential to destroy O_3 in the stratosphere. However, the inclusion of hydrogen atoms in the structures of HCFC compounds results in a sink by reaction with tropospheric OH, causing a reduction in the atmospheric burden of this compound that reaches the stratosphere. HFCs, on the other hand, avoid any prospect of stratospheric O_3 destruction, the ultimate goal of the Montreal Protocol, by excluding chlorine atoms from the compound structures altogether. However, a new environmental risk is posed by the transition from CFCs to HCFCs to HFCs; the global warming potentials

(GWPs, the potential of a compound to cause positive radiative forcing) of several widely used HFCs are large and could contribute to substantial radiative forcing of climate [*Velders et al.*, 2012]. By opting for HFCs with either shorter lifetimes resulting from greater reactivity with OH or lower GWPs, we can mitigate this scenario.

The chemistry outlined thus far makes clear the role of OH in many important aspects of atmospheric gas-phase composition; however, elucidating the chemistry of OH is also critical to our understanding of atmospheric aerosols. Gas-phase SO_2, for instance, undergoes oxidation by reaction with OH to form sulfate particles. Sulfate aerosols, consisting of sulfuric acid (H_2SO_4), along with condensable HNO_3 mentioned above are of interest to the atmospheric community due to their role in causing acid rain [*Galloway et al.*, 1984]. Aerosols also have effects on climate, first by directly reflecting sunlight entering the Earth's atmosphere, and second by altering the reflective properties of clouds [*IPCC*, 2013]. Finally, sulfate aerosols enable more efficient destruction of stratospheric O_3 [*Hofmann and Solomon*, 1989]. As a result, volcanic eruptions that inject SO_2 and sulfate directly into the stratosphere are of clear concern while smaller eruptions that increase background SO_2 in the troposphere are arguably important as well [*Vernier et al.*, 2011]. Whether or not tropospheric SO_2 is transported to the stratosphere is also determined by the chemistry of OH, so there exists current interest in evaluating the lifetime of SO_2 in various OH regimes [*Rex et al.*, 2014]. While the behavior of sulfate and nitrate aerosols is relatively well understood, the secondary organic aerosol (SOA) field of study is more complex. These aerosols derived from oxidation of hydrocarbons are

produced following the initial step of oxidation. As such, OH is a natural focus of study in understanding SOA as well [*Hoffmann et al.*, 1997; *Claeys et al.*, 2004].

1.1.2 Chemistry of Tropospheric OH

Primary production of tropospheric OH occurs via photolysis of O_3 to generate an excited state oxygen atom, $O(^1D)$:

$$O_3 + h\nu\ (\lambda \leq 336\ \text{nm}) \rightarrow O_2 + O(^1D) \qquad \textbf{(R1)}$$

The excited state $O(^1D)$ atom then reacts with a H_2O molecule to produce 2 hydroxyl radicals:

$$O(^1D) + H_2O \rightarrow 2\ OH \qquad \textbf{(R2)}$$

Hydroxyl can also be produced via secondary or recycling reactions that convert HO_2 and alkyl RO_2 peroxy radicals back to OH. The term "recycling" is used to refer to the fact that formation of HO_2 and RO_2 is typically initiated by oxidation of a compound by OH radical. The reaction for the rate-limiting step of tropospheric O_3 production is an example of one such recycling process:

$$HO_2 + NO \rightarrow OH + NO_2 \qquad \textbf{(R3)}$$

The reaction of HO_2 with O_3 also contributes to secondary OH production, though not to the extent seen by reaction with NO [*Levy et al.*, 1971; *Elshorbany et al.*, 2012]:

$$HO_2 + O_3 \rightarrow OH + 2\ O_2 \qquad \textbf{(R4)}$$

In the upper troposphere, photolysis of methyl hydroperoxide (CH_3OOH), formaldehyde (HCHO), and hydrogen peroxide (H_2O_2) can provide an important source of HO_x radicals, particularly when boundary layer air is convectively lofted to the upper troposphere [*Prather and Jacob*, 1997; *Jaeglé et al.*, 1998].

The sinks that exist for OH are numerous. Hydroxyl reacts with so many species that to consider the budget of OH alone would perhaps give an infinite number of sinks. As such, there is greater utility in identifying the sinks for the HO_x family of radicals as a whole. The two radical termination reactions introduced in the discussion of tropospheric O_3 serve as the most common loss processes for HO_x:

$$OH + NO_2 + M \rightarrow HNO_3 + M \quad (\mathbf{R5})$$

$$OH + HO_2 \rightarrow H_2O + O_2 \quad (\mathbf{R6})$$

$$HO_2 + HO_2 \rightarrow H_2O_2 + O_2 \quad (\mathbf{R7})$$

In addition, CO and CH_4 are commonly referred to as sinks of OH [*Logan et al.*, 1981; *Spivakovsky et al.*, 2000]; however, this is only true in a low-NO_x environment. In this case, recycling of HO_2 back to OH via Reaction 3 is prevented due to the absence of NO. One final sink to consider involves the heterogeneous uptake of HO_2 on aerosols. Instead of converting HO_2 to H_2O_2, a redox reaction involving dissolved copper and iron ions is responsible for rapidly converting HO_2 to H_2O [*Mao et al.*, 2013a]. So, while the fundamental chemistry involved in the production of OH is quite straightforward, the reactions one must consider to account for all HO_x reactivity in the atmosphere are diverse and complex. Given this complexity, it is understandable that uncertainties in the modeling of OH remain.

1.1.3 Current Research Challenges

Much research has been conducted on tropospheric OH, ranging from the original modeling studies [*Levy*, 1971; *Levy*, 1973] to the present-day measurement and kinetics studies. However, since the focus of this dissertation is on the

representation of OH within models, I will limit my discussion of the literature to a brief overview of recent measurements of OH followed by an in-depth outline of the current challenges faced in the modeling of OH.

The short lifetime and low concentrations of OH in the atmosphere cause the measurement of OH to be technically difficult. However, in the last two decades, advancements in instruments and analytical techniques have led to more abundant accurate and precise observations of OH [*Brune et al.*, 1998; *Heard and Pilling*, 2003; *Wennberg*, 2006]. Among these are OH measurements that occur on aircraft campaigns. *Mao et al.* [2009] developed an instrument that measures OH reactivity, or the inverse of the lifetime of OH. Their measurements during the Inter-continental Chemical Transport Experiment-B (INTEX-B) over the Pacific Ocean found that OH inferred from the measurement of OH reactivity was significantly larger than a steady-state model calculation could reproduce at altitudes below 4 km. *Olson et al.* [2004] measured OH directly by laser-induced fluorescence, also over the Pacific Ocean, during the NASA Transport and Chemical Evolution over the Pacific (TRACE-P) campaign. However, the TRACE-P measurements of OH were regularly over-predicted by a photochemical box model constrained to other measured species. Many other examples of model over- and under-prediction of OH by models compared to data are present in the literature. So, while observations of OH are available and increasingly accurate, their utility in guiding true constraint of the global OH burden is limited due to their often limited spatial and temporal scales, i.e. they are "snap shots" of the conditions present at the time.

The first issue confronting the tropospheric modeling community is that models differ drastically in their portrayal of OH on a global scale. Model intercomparison projects often compare output from two different types of atmospheric chemistry models: chemical transport models (CTMs), which constrain meteorological fields (temperature and winds) to values based on observations (usually reanalysis fields, which combine observations with model output, needed to fill in spatial and temporal gaps in the observational record); and chemistry-climate models (CCMs), run using internally generated meteorological fields. Intercomparison studies of both types of models regularly show large spreads in the tropospheric mean OH burdens ($[OH]^{GLOBAL}$) and resulting CH_4 lifetimes (τ_{CH4}) evaluated for each participating model. For example, *Shindell et al.* [2006] examined 26 CTMs and found values of τ_{CH4} ranging from 6.91 to 15.05 years. The multi-model mean τ_{CH4} for this study was 9.72 years; thus, the model spread in τ_{CH4} values was 84%. A similar, though updated, study by *Fiore et al.* [2009] calculated τ_{CH4} values from 6.19 to 12.50 years for 12 CTMs, a multi-model mean of 10.19 years, and a spread of 62%. The more recent studies by *Voulgarakis et al.* [2013] and *Naik et al.* [2013] analyzed the same 14 CCMs and determined a τ_{CH4} range of 7.1-13.9 years, multi-model mean of 9.8 years, and spread of 69%. While several studies seek to identify the causes of these spreads in $[OH]^{GLOBAL}$ and τ_{CH4}, the analyses performed point to circumstantial differences in the models but do not identify the true drivers of the differences in fields of OH [*Shindell et al.*, 2006]. Thus, there exists a strong need for a quantitative analysis that isolates the factors causing the 60+% spreads in modeled τ_{CH4} values.

In addition to the large spread in model-simulated $[OH]^{GLOBAL}$ and τ_{CH4} values, current understanding of OH is hampered by a systematic low bias in model τ_{CH4} relative to observation-based estimates of τ_{CH4}. Observational constraint of τ_{CH4} comes almost exclusively from chemical inversion analysis of methyl chloroform (CH_3CCl_3, abbreviated here as MCF). The approach of calculating global mean OH concentrations based on accurate knowledge of the emissions and measurements of the abundance of a chemical lost primarily by reaction with OH was proposed as early as 1977 [*Singh*, 1977]. MCF was banned by the Montreal Protocol, so its pronounced decay in the atmosphere has been observed, and its emissions have approached zero [*Montzka et al.*, 2000]. Most studies of MCF stop short of proposing a value for τ_{CH4}, instead evaluating only the anomalies in $[OH]^{GLOBAL}$ inferred from the MCF record or the lifetime inferred for MCF only. One study that first proposes a value for τ_{CH4} based on MCF is that by *Prinn et al.* [2005], which gives a τ_{CH4} value of $10.2^{+0.9}_{-0.7}$ years. The more recent estimation of τ_{CH4} by *Prather et al.* [2012], which also includes losses of CH_4 in soils, the stratosphere, and by atomic chlorine, reports τ_{CH4} as 11.2 ± 1.3 years.

The evaluation of τ_{CH4} given by *Prinn et al.* [2005] is closer to the lifetimes calculated by the global models discussed previously. However, subsequent studies point to potential problems in using the time period examined in *Prinn et al.* [2005]; both *Montzka et al.* [2011] and *Krol and Lelieveld* [2003] suggest that small errors in the emissions assumed in the inversion of MCF could lead to large errors in the resulting calculation of $[OH]^{GLOBAL}$ and τ_{CH4}. The more comprehensive analysis in *Prather et al.* [2012] suggests that the global models are underestimating τ_{CH4} by 1.0-

1.5 years, or 9-13%, on average. Given the model disagreement that exists concerning the value of τ_{CH4}, it would be reasonable to conclude that the models are not representing the true atmosphere. However, the sensitivity of the MCF analysis to errors in MCF and CH_4 emissions could result in values of τ_{CH4} that are instead biased high relative to the true atmosphere. *Krol and Lelieveld* [2003] point out that, if countries were stockpiling MCF following the ban on the chemical's production, the resulting overestimate of MCF emissions would lead to an underestimate in τ_{CH4}; the opposite would be true upon release of the stockpiled MCF. Similar logic applies to the issue of air-sea exchange of MCF. While most inversion studies account for ocean uptake of MCF, they do not provide a mechanism for the magnitude of the ocean sink to vary in time and even outgas MCF in polar regions, as *Wennberg et al.* [2004] suggests could be the case. In particular, latitudes poleward of 45° are proposed to have a net outgassing effect after year 1998 as a result of the rapid decrease in atmospheric concentrations of MCF. As with intentional release of stockpiled MCF, ocean release of MCF that is not considered during a chemical inversion analysis could result in a high bias in calculated τ_{CH4}. This effect may not be large enough to account for the entire discrepancy that exists between the models and the MCF estimates of τ_{CH4}, but it does convey movement toward agreement. Ultimately, the community needs to ascertain the true value τ_{CH4} and evaluate and address the cause of the τ_{CH4} bias, whether it be a low bias in models or a high bias in chemical inversion analyses.

The final challenge presently confronting atmospheric modelers is how $[OH]^{GLOBAL}$ evolves with time. Past trends in $[OH]^{GLOBAL}$ and τ_{CH4} are studied via

the same MCF inversion technique discussed previously. As with the absolute value of τ_{CH4}, though, disagreements in the level of interannual variability, deduced from the same MCF data, are present in the literature. *Prinn et al.* [2005] as well as *Bousquet et al.* [2005] infer a large degree of interannual variability in $[OH]^{GLOBAL}$ and τ_{CH4}, on the order of 10%. *Montzka et al.* [2011], on the other hand, find that $[OH]^{GLOBAL}$ is more well-buffered than suggested by *Prinn et al.* [2005] and *Bousquet et al.* [2005], with an interannual variability of about 2%. Again, these differences are attributed to the time period used in the analysis and uncertainties in the emissions [*Montzka et al.*, 2011]. Meanwhile, modeling studies that attempt to elucidate how future $[OH]^{GLOBAL}$ will adapt to climate change show a high level of discord. *Voulgarakis et al.* [2013] compare output from 14 CCMs that simulate atmospheric conditions for years 2000 and 2100 for all 4 future emissions scenarios, or Representative Concentration Pathways (RCPs) [*Meinshausen et al.*, 2011; *van Vuuren et al.*, 2011]. It is telling that the scenario (RCP8.5) that achieves the greatest level of agreement in the direction of change in $[OH]^{GLOBAL}$ gives a multi-model mean trend in τ_{CH4} of +8.5 ± 10.4% (1 standard deviation) between years 2000 and 2100. Visual inspection of the results for the other RCPs presented in *Voulgarakis et al.* [2013] suggests that the sign of change in τ_{CH4} over the coming century is highly uncertain.

Modeling studies that instead focus on reproducing past trends in $[OH]^{GLOBAL}$ have been more successful in at least converging on the factors that drive variability in global OH abundances, if not on the direction of change in $[OH]^{GLOBAL}$ from preindustrial times to now. For example, *Berntsen et al.* [1997] deduced a 6%

increase in $[OH]^{GLOBAL}$ between 1850 and 1990, while *Hauglustaine and Brasseur* [2001] inferred a 33% decrease in $[OH]^{GLOBAL}$ between 1850 and 2000; results from numerous other studies purport equally diverse changes in the global oxidizing capacity, as outlined by *Naik et al.* [2013]. Despite these differences, studies of past $[OH]^{GLOBAL}$ at least demonstrate acknowledgement of the need to consider the many factors that influence OH chemistry. *Lelieveld et al.* [2002], for instance, explicitly state the need for OH simulations to incorporate responses to NO_x and O_3 changes as well as the obvious sinks of OH, including CO and CH_4. *Naik et al.* [2013] go one step further in emphasizing the need to understand how OH will respond to climate change. While the body of work examining historical trends in $[OH]^{GLOBAL}$ is moving toward constraint of τ_{CH4}, it is still likely that some important factors influencing trends in $[OH]^{GLOBAL}$ are being neglected. In short, a comprehensive evaluation of the many factors involved in OH chemistry should be undertaken so as to understand the drivers of past trends in τ_{CH4} and improve model predictions of τ_{CH4}.

1.2 Goals Addressed by this Body of Work

The body of work encompassed by this dissertation seeks to address the three needs and challenges to our current understanding of OH chemistry outlined in Section 1.1.3. The study presented in Section 2 uses observations obtained during a 2014 aircraft campaign over the tropical Western Pacific to calculate observationally constrained values of OH. These calculations are compared to those of global models. The resulting differences in OH are attributed using an in-depth analysis of

OH precursor differences. Implications of these findings for OH concentrations in the remote tropical troposphere and subsequent lifetime determinations are discussed.

The project presented in Section 3 demonstrates a novel technique to quantify the factors driving large model spreads in $[OH]^{GLOBAL}$. A neural network approach is used to simulate the chemical mechanisms of individual models so as to reproduce their 3D fields of tropospheric OH given 11 chemical, radiative, and physical parameters as input. The neural networks are then used to calculate the effect on τ_{CH4} that would result from inputting a chemical or radiative variable from one model into the chemical mechanism of another. Results across all examined models are aggregated, and the largest drivers of the model spread in τ_{CH4} are quantified.

The final study presented in Section 4 performs empirical modeling of recent trends in $[OH]^{GLOBAL}$. Responses of $[OH]^{GLOBAL}$ to observed changes in H_2O, total column O_3, and CH_4 are calculated, and the effect of widening of the climatological tropics on $[OH]^{GLOBAL}$ is simulated. The overall trend in $[OH]^{GLOBAL}$ determined by this analysis is then used to reconcile seemingly contradictory views of the interannual variability in $[OH]^{GLOBAL}$ found in the literature. Results also suggest the importance of accounting for tropical widening in studies of future OH abundance.

Chapter 2: An Observationally Constrained Evaluation of the Oxidizing Capacity in the Tropical Western Pacific

2.1 Introduction

Lifetimes of many tropospheric species are determined by concentrations of hydroxyl radical (OH). In regions where convective lofting of air to the stratosphere is most active, such as the tropical Western Pacific (TWP) [*Newell and Gould-Stewart*, 1981; *Hatsushika and Yamazaki*, 2003; *Fueglistaler et al.*, 2004], quantification of the abundance of OH is crucial to evaluating the budget of any species oxidized by OH [*SPARC*, 2013]. In the TWP, very short-lived (VSL) halocarbons can contribute to stratospheric O_3 loss upon crossing the tropopause, a process facilitated by convective lofting [*Aschmann et al.*, 2009; *Ashfold et al.*, 2012; *Hossaini et al.*, 2012; *Liang et al.*, 2014]. Of these VSL species, several are lost primarily by reaction with OH. With lifetimes on the order of days to months, the efficiency of these species passing into the stratosphere hinges on the concentration of OH [e.g., *Rex et al*., 2014]. Stratospheric transport of SO_2 released by anthropogenic activities in Asia, which has been identified as a possible cause of increased background stratospheric sulfate aerosol loading [*Hofmann et al*., 2009], is also sensitive to the abundance of OH in the TWP [*Rex et al.*, 2014]. Similarly, simulations of the geographic distribution of carbon monoxide (CO), a long-lived anthropogenic pollutant, depend on the accuracy of tropospheric [OH] (OH number density) as well as its emissions [*Shindell et al.*, 2006; *Monks et al.*, 2015; *Strode et al.*, 2015].

The short-lived, reactive nature of OH makes it a challenging compound to measure accurately. As a result, observational constraints on OH are often restricted in spatial and temporal coverage. Measurements of OH in the TWP are limited to the Stratospheric Tracers of Atmospheric Transport (STRAT) [*Gao et al.*, 2014] and Pacific Exploratory Mission – Tropics B (PEM-Tropics B) [*Tan et al.*, 2001] aircraft campaigns, which only skirted the upper troposphere over the Pacific warm pool region. However, during the STRAT campaign, the NASA ER-2 aircraft sampled an upper stratospheric air parcel near Hawaii that had originated from convective outflow in the TWP. Hydroxyl concentrations were extremely small ($\sim 0.5\times10^{6}$ cm^{-3}) given the low Solar Zenith Angle (SZA). Upper tropospheric OH generally follows a straightforward relation dependent on SZA [*Hanisco et al.*, 2001], with lower SZA corresponding to higher OH. In this parcel near Hawaii, low nitric oxide (NO) (i.e., [NO] < 1×10^{8} cm^{-3}) suppressed the normally rapid conversion of HO_2 to OH [*Gao et al.*, 2014].

Rex et al. [2014] similarly found observational evidence of a marked OH minimum throughout the TWP troposphere. In this case, the OH minimum was driven by low mixing ratios of O_3 (< 15 ppb) measured by sondes during the TransBrom ship-based campaign in October 2009 [*Kruger and Quack*, 2013]. Calculations conducted using the GEOS-Chem model, which agreed well with the low O_3 measurements, resulted in small values of [OH] ($\leq 0.75\times10^{6}$ cm^{-3}) likely as a result of suppressed primary production [*Rex et al.*, 2014]. While there are no direct measurements of OH in the central region of the TWP, the suggestion of the existence of depressed OH as a result of low concentrations of NO or O_3 (or a combination of

these two factors) motivates the need for increased observational constraints to better quantify OH in the TWP.

Another motivation for improved understanding of OH in the TWP arises from the considerable range in the global burden of OH among global models. Concentrations of OH maximize near the surface in the tropical troposphere, so the mean tropospheric burden of OH and CH_4 lifetime within global models are largely influenced by the tropics (here we denote CH_4 lifetime as τ_{CH4} and refer to CH_4 lifetime as that due to loss by reaction only with tropospheric OH, unless noted otherwise). The Atmospheric Chemistry and Climate Model Intercomparison Project (ACCMIP) analyzed 14 models and found a 62% spread (full range of values divided by the multi-model mean) in global burdens of OH [*Voulgarakis et al.*, 2013]. Most of the models analyzed were chemistry-climate models (CCMs), *i.e.* they were run using model-generated meteorology. Other projects that compare output solely from chemistry transport models (CTMs, in which meteorological fields are constrained to reanalysis fields) might be expected to have better-constrained OH due to the use of similar transport fields. Our analysis of one such project, the POLARCAT Model Intercomparison Project (POLMIP) [*Emmons et al.*, 2015], suggests the spread in τ_{CH4} across 8 models is ~38%: a smaller range, but for fewer models [*Nicely et al.*, 2016a]. Other model intercomparison studies show similar results: *Shindell et al.* [2006] reported a 65% spread in global mean OH among 26 models and *Fiore et al.* [2009] found a 62% spread in τ_{CH4} due to loss by OH among 12 models.

Considering these large spreads in OH burdens among various global models, it is not surprising that models also disagree on the future evolution of OH

concentrations. *Voulgarakis et al.* [2013] found that the ACCMIP models do not agree on the sign of change in the global burden of OH over the next century. Early estimates of the effect of climate change on atmospheric chemistry predicted that global OH burdens would decline with expected increases in global burdens of CH_4 and CO (e.g., *Houghton et al.* [1996]). However, many facets of OH chemistry were simplified in these studies. It is now believed that other factors, including increasing water vapor [*Stevenson et al.*, 2000; *Hauglustaine et al.*, 2005] and rising temperatures leading to faster CH_4 oxidation [*Johnson et al.*, 1999] could instead result in larger future burdens of OH [*Stevenson et al.*, 2006]. Given that climate modelers seek to understand a wide range of possible future conditions through consideration of multiple emissions scenarios, it seems reasonable that the community should first seek to understand how well models represent OH in the contemporary atmosphere.

Another issue confronting the modeling community is that global models systematically underestimate τ_{CH4} by ~1.75 years (~16%) relative to current empirical best estimates [e.g., *Naik et al.*, 2013]. Measurements of methyl chloroform (MCF: CH_3CCl_3) decay rates are most commonly used to determine the mean tropospheric concentration of OH as well as τ_{CH4} [*Singh*, 1977; *Prinn et al.*, 2005; *Montzka et al.*, 2011]. For example, *Prinn et al*. [2005] reported τ_{CH4} of $10.2^{+0.9}_{-0.7}$ years in 2003 based on the observed decay of MCF. More recently, *Prather et al.* [2012] reported a value for τ_{CH4} of 11.2 ± 1.3 years, based on analysis of MCF that includes loss of CH_4 by soils, the stratosphere, reaction with tropospheric atomic chlorine, as well as tropospheric OH. The burden of tropospheric OH from the ACCMIP CCMs and

POLMIP CTMs discussed earlier yield mean CH_4 lifetimes of 9.8 ± 1.6 [*Voulgarakis et al.*, 2013] and 8.1 ± 0.9 years [*Nicely et al.*, 2016a], where the uncertainties are 1 standard deviation about the multi-model mean. The discrepancy between MCF-based and model-based estimates of τ_{CH4} could be resolved if the burdens of tropospheric OH within global models were shown to be too high, based on actual tropospheric abundances. However, our study suggests otherwise, at least for the TWP during winter 2014: we show that actual tropospheric abundances of OH exceed values within eight global models. Another possible resolution to this discrepancy would be an error in the MCF-based estimate of $\tau_{CH4.}$ *Krol and Lelieveld* [2003] pointed out that stockpiling and later release of MCF, as the Montreal Protocol was being implemented, could lead to an uncertainty that during the time of release of stockpiled MCF, if not considered, would lead to an overestimate of τ_{CH4} via the MCF method and therefore could help resolve this discrepancy. *Wennberg et al.* [2004] noted the importance of air-sea exchange of MCF, which during times of oceanic release would similarly lead to an overestimate of τ_{CH4} by the MCF method. Conversely, *Wang et al.* [2008] used three-dimensional model estimates of OH, together with MCF abundance and emission data, to suggest the actual value of τ_{CH4} via the MCF method is longer than found in other studies.

We use data collected during the CONvective TRansport of Active Species in the Tropics (CONTRAST) aircraft campaign [*Pan et al.,* 2016], conducted during winter 2014 from Guam (13.5°N, 144.8°E), to model the abundance of OH in the TWP. While OH was not measured during CONTRAST, a multitude of chemical species, radiative variables, and meteorological parameters needed to model the

production and loss of OH were measured. The Dynamically Simple Model for Atmospheric Chemical Complexity (DSMACC) box model [*Emmerson and Evans*, 2009], constrained to observations of OH precursors and related species, is used to calculate instantaneous and 24 hour average OH. We then compare our results to values of OH computed by the CAM-Chem model, run as a CTM with assimilated meteorology [*Lamarque et al*., 2012]. Additional box model runs were performed to determine the OH precursor species driving the differences between the CTM and observationally derived OH. We also assess the impact on OH of high-O_3, low-H_2O structures frequently observed in the mid-troposphere throughout CONTRAST [*Anderson et al*., 2016; *Pan et al.*, 2015]. Additionally, the local lifetime of dibromomethane (CH_2Br_2) (τ_{CH2Br2}), a brominated VSL lost primarily by reaction with OH, is evaluated and compared to previously published estimates. Finally, we compare our observationally constrained OH distribution to output from the POLMIP CTMs to highlight a few shortcomings in these global models.

2.2 Data and Methods

2.2.1 CONTRAST Campaign

The CONTRAST campaign [*Pan et al.*, 2016] was based in Guam (13.5°N, 144.8°E) during January and February 2014. Observations were obtained by a suite of chemical, meteorological, and radiative instruments onboard the NSF/NCAR Gulfstream V (GV) aircraft. The foci of various research flights (RFs) consisted of either surveying the TWP, sampling convective outflow, or obtaining observations

across both the inter-tropical convergence zone as well as the subtropical jet stream. Our study uses observations acquired over the portion of the TWP sampled extensively during CONTRAST; i.e., the region bounded by latitudes 0°N to 20°N, longitudes of 132°E to 162°E (**Figure 2-1**). We further restrict the study to data collected during times when valid measurements of O_3 exist and when SZA < 60° (i.e., mid-day or higher illumination). Following these guidelines, we analyzed data collected during the portions of RF 04 to RF 15 that lie within the red box of Figure

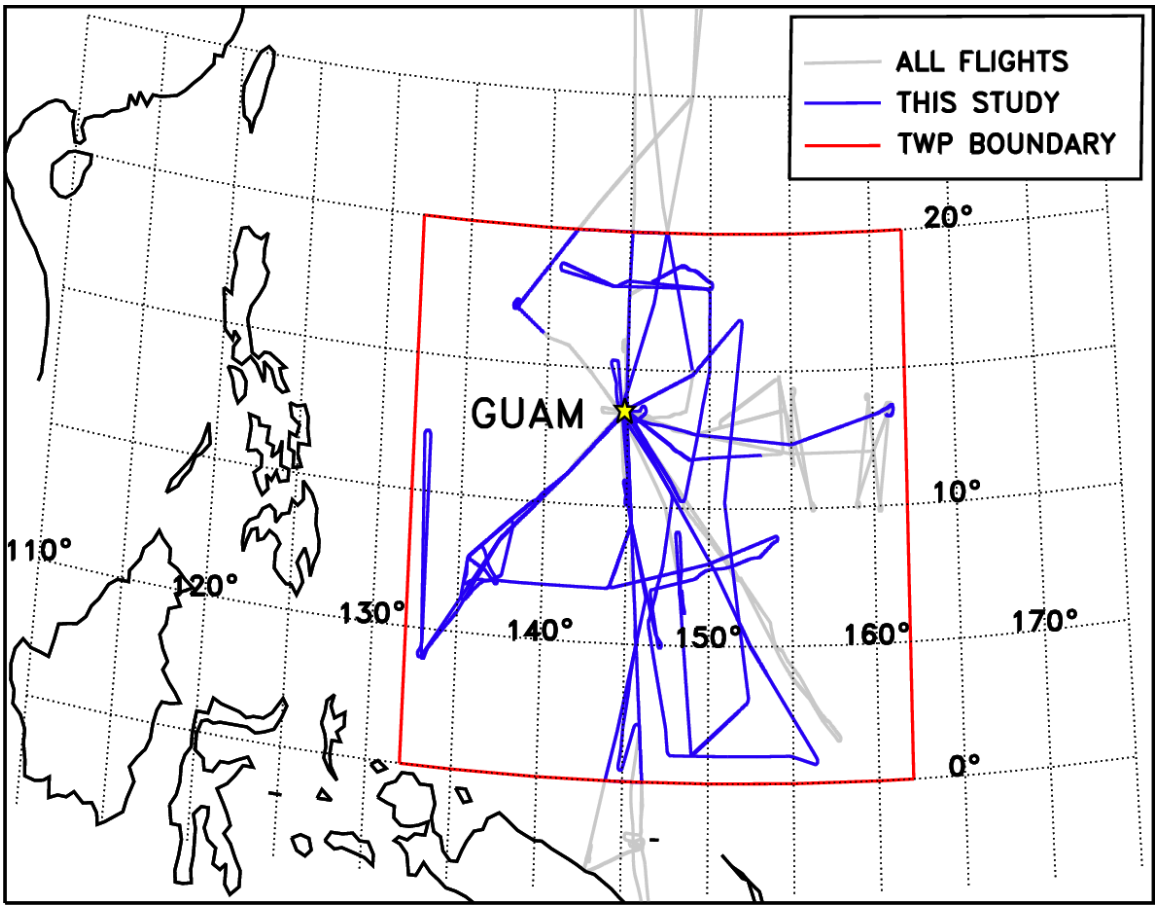

Figure 2-1. Flight tracks of the GV aircraft during the CONTRAST campaign, January – February 2014. Portions of flight tracks used in this study are shown in blue; criteria for including aircraft data are SZA ≤ 60°, latitude between 0°N and 20°N, and longitude between 132°E and 162°E (latitude/longitude bounds indicated by red box), and presence of valid data for O_3 and CO at the time and location of observation. Portions of flight tracks not included in this study are shown in grey.

2-1. Data collected during the four transit flights (RF 01, 02, 16, and 17) are excluded, as are data collected during RF 03 since measurements of CO are not available.

The CONTRAST measurements used in this study include O_3 and NO obtained onboard the GV aircraft by chemiluminescence at a frequency of 1 Hz with 1σ precisions of 0.5 ppb and 10 ppt, both with uncertainties of 5% [*Ridley and Grahek*, 1990]. CO measurements were obtained using an Aero-Laser 5002 vacuum ultraviolet fluorescence instrument at a frequency of 1 Hz and with a 2σ uncertainty of 3 ppb ± 3% [*Gerbig et al.*, 1999]. Water mixing ratios were measured by an open-path laser hygrometer at a frequency of 1 Hz and 2σ precision of < 3% [*Zondlo et al.*, 2010]. CH_4 measurements were made using a Picarro G2311-fm $CO_2/CH_4/H_2O$ cavity ring-down spectrometer with output provided at 1 Hz with a 1σ precision of 3 ppb [*Crosson*, 2008]. Formaldehyde (HCHO) was measured via laser-induced fluorescence by the *in situ* airborne formaldehyde (ISAF) instrument with reported values at 1 Hz frequency and 2σ uncertainty of ± 20 ppt [*Cazorla et al.*, 2015]. A number of organic trace gas measurements are used from the trace organic gas analyzer (TOGA) gas chromatograph/mass spectrometer (GCMS) instrument [*Apel et al.*, 2003]. Acetone (CH_3COCH_3), isoprene (C_5H_8), propane (C_3H_8), methanol (CH_3OH), and acetaldehyde (CH_3CHO) were measured with a sampling time of 35 seconds and output every 2 minutes. Additionally, HCHO from TOGA is sporadically used when data from ISAF was missing for lengths of time. Limits of detection (uncertainties) for the TOGA species are: 20 ppt (20% or 40 ppt) for CH_3COCH_3, 1 ppt (15% or 2 ppt) for C_5H_8, 10 ppt (30% or 20 ppt) for C_3H_8, 20 ppt

(30% or 40 ppt) for CH_3OH, 5 ppt (20% or 10 ppt) for CH_3CHO, and 2 ppt (100% or 80 ppt) for HCHO. Finally, photolysis frequencies for the reactions:

$$O_3 + h\nu \rightarrow O_2 + O(^1D) \qquad \textbf{R1}$$

$$NO_2 + h\nu \rightarrow NO + O(^3P) \qquad \textbf{R2}$$

are provided every 6 seconds, calculated from measurements of up- and down-welling, spectrally resolved actinic flux density by the HIAPER Airborne Radiation Package (HARP) [*Shetter and Muller*, 1999]. Total 1σ uncertainties for the photolysis frequencies of **R1** (hereafter denoted $J(O^1D)$) and **R2** (denoted $J(NO_2)$) are estimated to be 25% and 12%, respectively. These estimates account for calibration, instrumental, and spectral (including cross section and quantum yield) uncertainties.

The data set described above was adapted to a variable time resolution for this study because we conduct numerous box model simulations of data collected along each flight track. At level altitude flight legs a resolution of 10 minutes is used, whereas a finer resolution of 30 seconds is implemented while the aircraft is ascending or descending. This variable time resolution preserves fine-scale features, such as HOLW structures, often observed within vertical profiles. Measurements are averaged (i.e., along either 30 sec or 10 minute intervals) when valid data are present. This choice of variable temporal resolution results in 2600 samples of atmospheric composition across the 12 flights, which requires 12 hours of actual clock time to simulate using the box model, on a 4 core Linux computer.

2.2.2 DSMACC Box Model

We use the Dynamically Simple Model for Atmospheric Chemical Complexity (DSMACC) to perform box model calculations of OH [*Emmerson and Evans*, 2009]. This box model uses the Kinetic PreProcessor (KPP), the Tropospheric Ultraviolet and Visible radiation model version 4.2 (TUV), and a subset (644 species; 2046 chemical reactions) of the Master Chemical Mechanism (MCM) version 3.3 [*Jenkin et al.*, 1997; *Saunders et al.*, 2003; *Jenkin et al.*, 2015]. The box model is constrained to CONTRAST measurements of meteorological variables, O_3, CO, NO, HCHO, H_2O, C_3H_8, CH_4, C_5H_8, CH_3COCH_3, CH_3OH, CH_3CHO, $J(O^1D)$, and $J(NO_2)$. Constraints for all chemical species, except NO, result in that variable being held fixed at the initial value for the duration of the model run, which progresses through several solar cycles until reaching diel steady state (i.e., production and loss equal over a 24 hour period of time). The abundances of NO and other NO_y compounds fluctuate with time within the model, due to varying solar illumination, though NO is forced to return to the initial value after each complete solar cycle. Therefore, the model is initialized to the measured abundance of NO at the local solar time of observation while NO_y compounds are allowed to vary. Photolysis frequencies also vary diurnally. They are first calculated by the TUV module for the latitude, longitude, and pressure coordinates of the specific observation, but are then scaled to the observed J value at the time of observation via a constant multiplicative factor. This multiplicative factor is applied throughout the diurnal cycles simulated by the model. The J values for other species are scaled according to a combination of the $J(NO_2)$ and $J(O^1D)$ scaling factors, determined by the wavelength range in which

the species photolyze. Upon reaching diurnal steady state, the box model outputs the final 24 hours of chemical concentrations as well as photolysis and reaction rates at intervals of the chosen model time step (10 minutes), enabling us to evaluate both instantaneous OH (at the time of observation) as well as 24-hour average OH.

For the analysis of OH during the CONTRAST campaign the box model is constrained to the 11 GV chemical measurements noted above, plus $J(O^1D)$, $J(NO_2)$, temperature, pressure, latitude, longitude, and local solar time. These calculated OH values will hereafter be referred to as "GV OH". Additional box modeling calculations are performed, constrained to the output from the global models described below.

Given the nature of aircraft sampling; i.e., the necessity of calibrating mid-flight, the variable temporal resolution of specific instruments, as well as occasional gaps due to instrument performance, valid data are frequently unavailable. For example, only 311 of the aforementioned 2600 samples of atmospheric composition have valid measurements of all 13 GV variables. To obtain a robust estimate of GV OH (i.e., representative of the mean state of the TWP during January and February 2014), we have developed a method to fill in missing data values. Given the importance and atmospheric variability of O_3, all atmospheric samples used here include a valid measurement of O_3. For other species as well as $J(O^1D)$ and $J(NO_2)$, if missing data occur before measurements of a particular variable have been made for the specific flight (i.e., during takeoff or the initial leg) or after an instrument has stopped sampling for the specific flight, missing data are filled in by averaging all other valid measurements that exist within 0.5° latitude, 0.5° longitude, and 2000 m

altitude. This helps ensure that the substitute value is from a similar air mass sampled close in location to where missing data are reported. For missing data that occur when measurements exist both earlier and later in the current flight, a value is found by linearly interpolating between the two closest valid data points. An exception is made for H_2O when altitude is varying; in these cases, gaps in the H_2O mixing ratio are either filled using the latitude/longitude/altitude binning method (if available) or the data point is excluded from the analysis. For HCHO, we use measurements from the ISAF instrument whenever valid data points exist. When HCHO from ISAF is unavailable, observations from the TOGA instrument are used. In this case, regression of ISAF against TOGA HCHO is used on a flight-by-flight basis to account for instrument differences (generally, [HCHO] from TOGA > [HCHO] from ISAF).

Given that the GV aircraft was sampling in the remote TWP, the mixing ratios of the organic trace gases measured by TOGA used in this analysis (C_3H_8, C_5H_8, CH_3COCH_3, CH_3OH, CH_3CHO) were at times below the limit of detection (LOD) of the instrument. When the abundance of a compound was below the LOD, we specified abundance based on the number of "below LOD" data points reported in succession. Mixing ratio equal to 50% of the LOD was specified when fewer than 10 "below LOD" data points occurred in succession; conversely, a mixing ratio equal to 20% of the LOD was used when 10 or more "below LOD" data points occurred in succession. Isoprene (C_5H_8) is the species most commonly affected by the TOGA LOD. Our scientific results are unaffected by any reasonable assumption for [C_5H_8]

and the other organics when below the TOGA LOD, including specification of $[C_5H_8]=0$ within the model.

We have tagged each of the 13 GV variables, to assess for all 2600 samples whether and how data gaps were filled. The scientific results shown below are the same whether the analysis is based on the 300 sampling intervals when valid data exist for all species, or the 2600 intervals considered below. We have chosen to show results for the 2600 intervals, since this provides more robust sampling of the TWP.

2.2.3 CAM-Chem CTM: CONTRAST (Winter 2014)

The Community Atmosphere Model version 4.0 (CAM4) is the atmospheric component of the global chemistry-climate Community Earth System Model (CESM) [*Lamarque et al.*, 2012]. For the CONTRAST campaign, the model was run with active chemistry and specified meteorology, a configuration referred to as CAM-Chem. The meteorological fields originate from the NASA GEOS5 model, with a horizontal resolution of 0.94° latitude × 1.25° longitude and 56 vertical levels. The model chemistry scheme includes a detailed representation of tropospheric and stratospheric chemistry (~180 species; ~500 chemical reactions), including very short-lived halogens. *Fernandez et al.* [2014] provide details on surface emissions, wet and dry deposition, heterogeneous reactions, and photochemical processes of halogens used within CAM-Chem. Anthropogenic emissions are specified from the RCP 8.5 scenario, and biomass burning emissions are from the Fire INventory for NCAR (FINN) [*Wiedinmyer et al.*, 2011].

Output from the CAM-Chem model includes all the species and variables that are used to constrain and initialize the box model, described in Section 2.2.2. The model output is linearly interpolated to the aircraft latitude, longitude and local solar time for all flights in the campaign, providing us with "curtains", or output at all model vertical levels along the space/time coordinate of each research flight. The curtain file model output allows quantitative comparison of GV OH to CAM-Chem OH, GV OH to be visualized in the context of surrounding atmospheric features, and the causes of differences between GV OH and CAM-Chem OH to be assessed.

Differences between observationally-constrained box model OH and global model OH may result from a number of factors, including differences in the chemical mechanism within the two models. The chemical mechanism can be assessed by examining whether the box model can reproduce OH output by the global model when constrained to precursor output from the global model. We therefore perform box model calculations of OH based on inputs from CAM-Chem for each flight. Additionally, variations in GV OH and CAM-Chem OH may arise from differences in the OH precursor fields. This effect is examined by performing variable "swaps", in which the box model is constrained by OH precursor fields from CAM-Chem except for a single input taken instead from the GV observations. The resulting difference in OH between the "all CAM-Chem" box model run and the "all CAM-Chem + GV [variable]" run can then be ascribed to that precursor field. In this work, swap runs are performed using GV O_3, H_2O, NO_x, CO, C_5H_8, HCHO, CH_3CHO, $J(O^1D)$, and $J(NO_2)$. These swap runs are performed for all flights.

The differences between GV OH and CAM-Chem OH are quantified by calculating tropospheric column OH values. We integrate the 24-hour mean [OH] vertical profile, averaged for all flights, for each simulation of OH: GV OH, CAM-Chem OH, and the swaps of the 9 variables listed above. We also perform one additional simulation to examine the effect of a possible clear-sky sampling bias that occurred during aircraft sampling, discussed further in Section 2.3.2. In this simulation, we constrained the box model to $J(NO_2)$ and $J(O^1D)$ from CAM-Chem and GV observations for all other inputs. Columns are integrated from the surface to 13 km so as to match the vertical extent of columns calculated for the POLMIP CTM swap simulations, which are limited by the calculation of scaling factors used in the simulations (see Section 2.3.4).

2.2.4 POLMIP CTMs (2008)

POLMIP was conducted to utilize the Polar Study using Aircraft, Remote Sensing, Surface Measurements and Models, of Climate, Chemistry, Aerosols, and Transport (POLARCAT) [*Law et al.*, 2014] suite of observations acquired in 2008 for the purpose of evaluating global chemistry models [*Emmons et al.*, 2015]. While the POLARCAT aircraft campaigns were designed for focused study of the Arctic troposphere, POLMIP consists of global model simulations. These simulations were performed for January to December, 2008, using a common emissions inventory (see *Emmons et al.* [2015] for further detail). All participating models were run in CTM mode, meaning wind and temperature inputs were based on analyzed meteorological fields. Accordingly, meteorological variables are roughly consistent among the

models. Each model was also run with its standard chemistry and deposition schemes. Models provided monthly mean output for many chemical, physical, and radiative variables, including OH. Those models that provided a global field of OH – CAM4-Chem, C-IFS, GEOS-Chem, GMI-GEOS5, LMDz-INCA, MOZART-4, TM5, and TOMCAT – are analyzed here.

The POLMIP project and the CONTRAST campaign focused on different years, 2008 and 2014, respectively. The Multivariate El Niño – Southern Oscillation (ENSO) Index for January/February 2008 was in a moderate negative phase while the same months in 2014 were neutral [*Wolter and Timlin*, 1993; 1998]. Hence, the westward shift of the Pacific warm pool and associated changes in locations of active convection, biomass burning, and the northern subtropical jet stream could account for some of the differences between the POLMIP CTMs and CONTRAST observations. Differences in biomass burning, whether due to ENSO effects or other factors, could also account for differences in chemical species associated with fire emissions. However, the changes in fire count, as obtained from the MODIS instrument on board the Terra and Aqua satellites (**Figure 2-2**) suggest that fire patterns were broadly consistent between 2008 and 2014. Nonetheless, the patterns between POLMIP multi-model mean of various species and the CONTRAST observations are nearly identical to the patterns between the CAM-Chem CTM (run using 2014 meteorology) and the CONTRAST observations. Comparison of the CAM-Chem simulation included in POLMIP to that conducted for CONTRAST (not shown) shows the largest differences in OH precursors between the two years occur for H_2O, which was higher in 2014 than in 2008, accounting for the higher OH seen

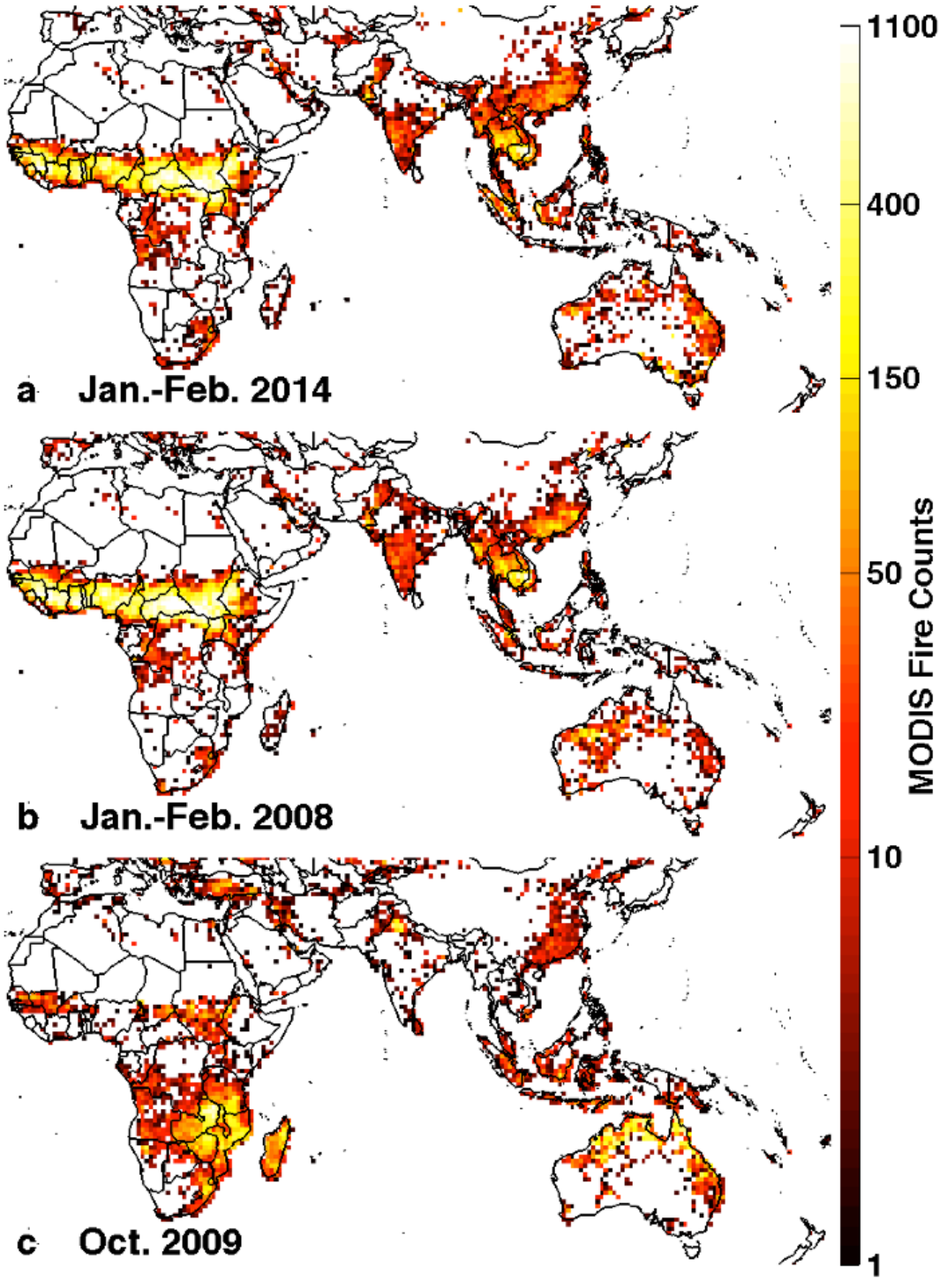

Figure 2-2. Total fire counts from MODIS in January and February for the years 2014 (panel a) and 2008 (b) and October for the year 2009 (c).

in the TWP. Mean values of CO are also larger in 2014, but are unlikely to be driving differences in OH, according to our analysis of OH sensitivity to CO shown below. By extending our analysis to the POLMIP archive, we are able assess the strengths and a few shortcomings of a suite of CTMs. The POLMIP monthly mean output is also available for all 12 months, allowing insight into the seasonal variation of OH and its precursors.

2.2.5 CH_2Br_2 Lifetime

We use the 24-hour average values of OH resulting from the box model constrained by GV observations and by output of the CAM-Chem model run performed for CONTRAST, as well as monthly mean OH from the POLMIP archive, to evaluate the tropospheric lifetime of CH_2Br_2. CH_2Br_2 is one of the previously-mentioned VSL species lost primarily by reaction with OH in the troposphere. Here we use:

$$k_{OH+CH2Br2} = 2.0\times10^{-12}\exp(-840/\mathrm{T}) \quad \textbf{(1)}$$

for the rate constant of reaction between OH and CH_2Br_2 [*Sander et al.*, 2011]. The lifetime, τ, of CH_2Br_2 is then found using:

$$\tau_{CH2Br2} = \frac{1}{k_{OH+CH2Br2}\times[OH]} \quad \textbf{(2)}$$

where [OH] is the number density of OH (units cm^{-3}). According to the WMO *Scientific Assessment of Ozone Depletion* [2011], the global tropospheric mean lifetime of CH_2Br_2 due to reaction with OH is 123 days. In the OH minimum of the TWP region, however, modeling studies suggest that τ_{CH2Br2} could be as high as 188

days at 500 hPa [*Rex et al.*, 2014]. We calculate τ_{CH2Br2} by altitude bin using the GV box modeled OH and compare to the *Rex et al.* [2014] estimate at 500 hPa (~5.3 km altitude).

2.2.6 HOLW Structures

We also evaluate the impact of high-O_3, low-H_2O (HOLW) structures on OH concentrations in the TWP. Many air parcels exhibiting high O_3 (defined as $O_3 > 40$ ppb) and low relative humidity (RH < 20%) were observed in the mid-troposphere [*Anderson et al.*, 2016; *Pan et al.*, 2016]. Relative humidity is calculated from observed H_2O and temperature (T), with respect to liquid water for T > 0°C and with respect to ice for T < 0°C. Primary production of OH occurs via **R1** followed by:

$$O(^1D) + H_2O \rightarrow 2\ OH \qquad \textbf{R3}.$$

The presence of HOLW structures, therefore, leads to competing effects on [OH]; low H_2O tends to suppress [OH] while elevated O_3 drives production of $O(^1D)$ and OH. We use the box model to investigate the net effect on [OH] of HOLW conditions and compare to the OH concentrations found in background conditions, defined as $O_3 <$ 25 ppb and RH > 70%.

2.3 Results and Discussion

2.3.1 Box Model GV OH and Comparison to CAM-Chem

The GV run of the box model, in which all model inputs are taken directly from measurements made during CONTRAST, reveals OH mixing ratios that are generally higher than those calculated by the CAM-Chem CTM. **Figures 2-3a** and **2-3b** show results from RF 07. Figure 2-3a shows GV OH values calculated by the box model as circles over-plotted on a "curtain" of OH values from CAM-Chem, in time and altitude. Figure 2-3b shows the correlation of GV OH against the OH value from CAM-Chem, extracted for the altitude of the observation. CAM-Chem underestimates OH calculated by the GV box model by about 60%. Considerable spread about the 1:1 line ($r^2 = 0.12$, Figure 2-3b) suggests an inability of the global model to precisely estimate occurrences of high and low OH. To understand whether differences between the chemical mechanisms within DSMACC and CAM-Chem are contributing to the difference in OH shown in Figures 2-3a and 2-3b, we constrain the box model using inputs of OH precursors from CAM-Chem. As shown in **Figures 2-3c** and **2-3d,** the box model using CAM-Chem inputs does a much better job of matching CAM-Chem OH. The OH mixing ratios do not lie perfectly along the 1:1 line, suggesting some differences in chemical mechanism may exist. However, the respective values of OH exhibit strong correlation ($r^2 = 0.92$), demonstrating that the chemical mechanism does not drive the differences in OH seen in Figures 2-3a and 2-3b.

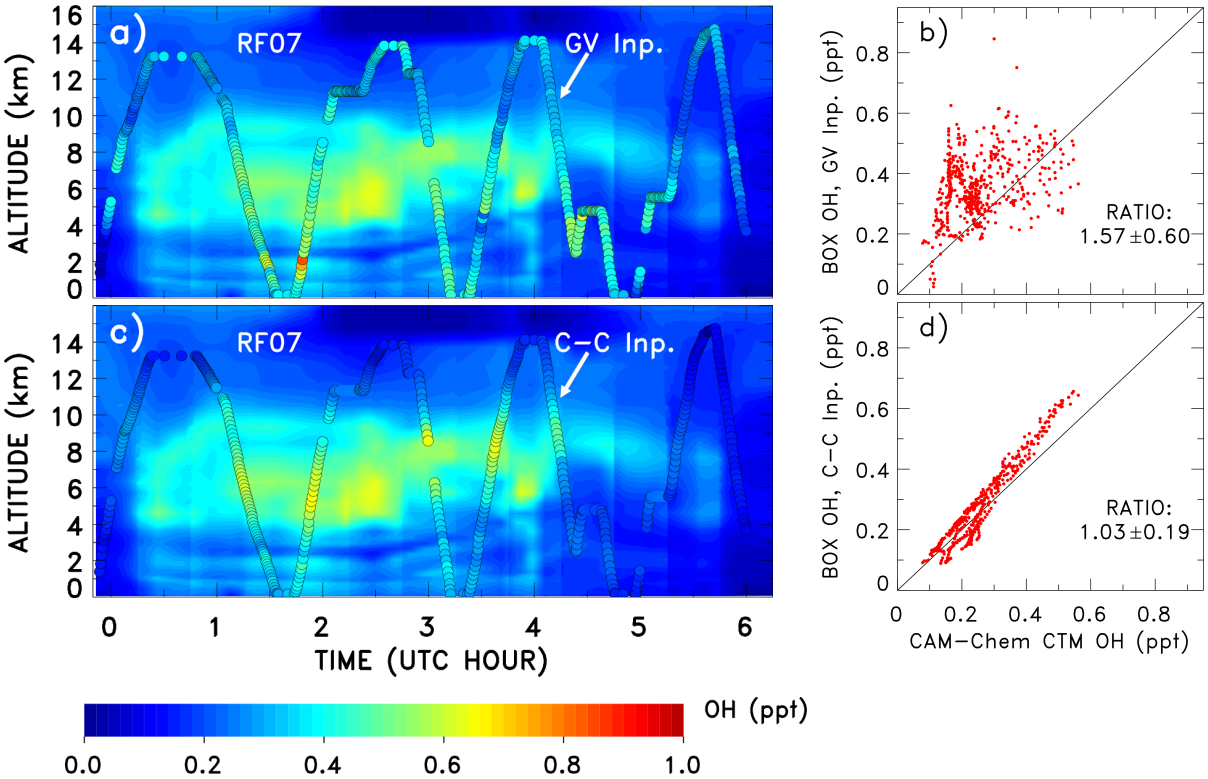

Figure 2-3. Box modeled OH compared to OH output from the CAM-Chem CTM run using meteorology for the CONTRAST campaign; results here are for RF 07 (29 January 2014): (a) the background "curtain" shows profiles of OH mixing ratios from the CAM-Chem CTM calculated for the latitude, longitude and SZA of the GV aircraft; the over-plotted circles show OH output from the DSMACC box model constrained to CONTRAST observations; (b) scatter plot of box modeled OH versus CAM-Chem OH for the altitude of the GV; (c) same as a) but with box model now constrained to OH precursors from CAM-Chem; (d) same as b) but with box model constrained to OH precursors from CAM-Chem. The black line on the scatter plots is the 1:1 line. The mean and standard deviation of the ratio (BOX OH)/(CAM-Chem OH) are indicated.

We also show results for RF 11, for which OH maxima existed aloft as well as in the mid-troposphere (**Figure 2-4**). Both GV and CAM-Chem OH approach mixing ratios of 0.8 ppt, though the notable CAM-Chem maximum around hour 4.5 is not matched by the GV OH. Swap analyses for this flight (not shown) show this mismatch results from differences in O_3 and H_2O, probably occurring in the form of an HOLW structure in the observations. Again, running the box model constrained to

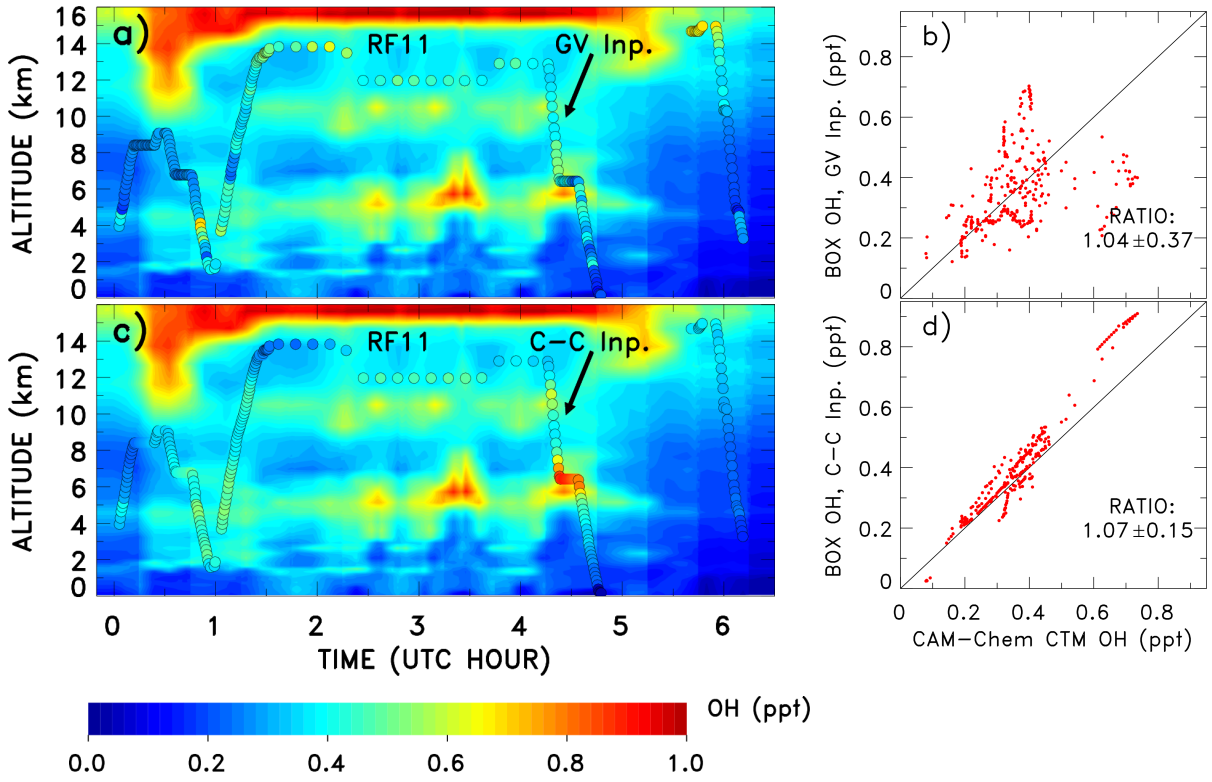

Figure 2-4. Same as Fig. 2-3, except for RF 11 (13 February 2014). The r^2 for panel b) is 0.12 and the r^2 for panel d) is 0.93.

output from CAM-Chem for this flight reveals that the chemical mechanism is not responsible for the differences in OH along the flight track (Figure 2-4c, d).

2.3.2 Evaluation of Precursor Differences, GV and CAM-Chem OH

We investigate each OH precursor using the box model "swap" method (Section 2.2.3) for all flights. Here we show results from RF 07, which occurred entirely within our latitude/longitude/SZA thresholds, conducted extensive vertical profiling, and provided mostly uninterrupted measurements of all chemical species and variables used to constrain the box model. Six variables, O_3, H_2O, $J(O^1D)$, NO_x, HCHO and CH_3CHO, account for the majority of the difference between GV and CAM-Chem OH. **Figure 2-5** shows box model results for swaps of these six

variables: i.e., the box model is constrained by the GV observation of the stated variable while all other constraints are taken from CAM-Chem. Any deviation in the scatter plot from the tight linear correlation shown in the "all CAM-Chem" run (Figure 2-3d) results from differences in the swapped variable. The closer the new OH distribution comes to matching the "all GV" run (Figure 2-3b and grey points in Figure 2-5), the larger the role of that variable in explaining the difference between GV and CAM-Chem OH.

Figure 2-6 compares profiles of these six variables measured by the GV on RF 07 to profiles found using the CAM-Chem CTM. All panels represent mean and

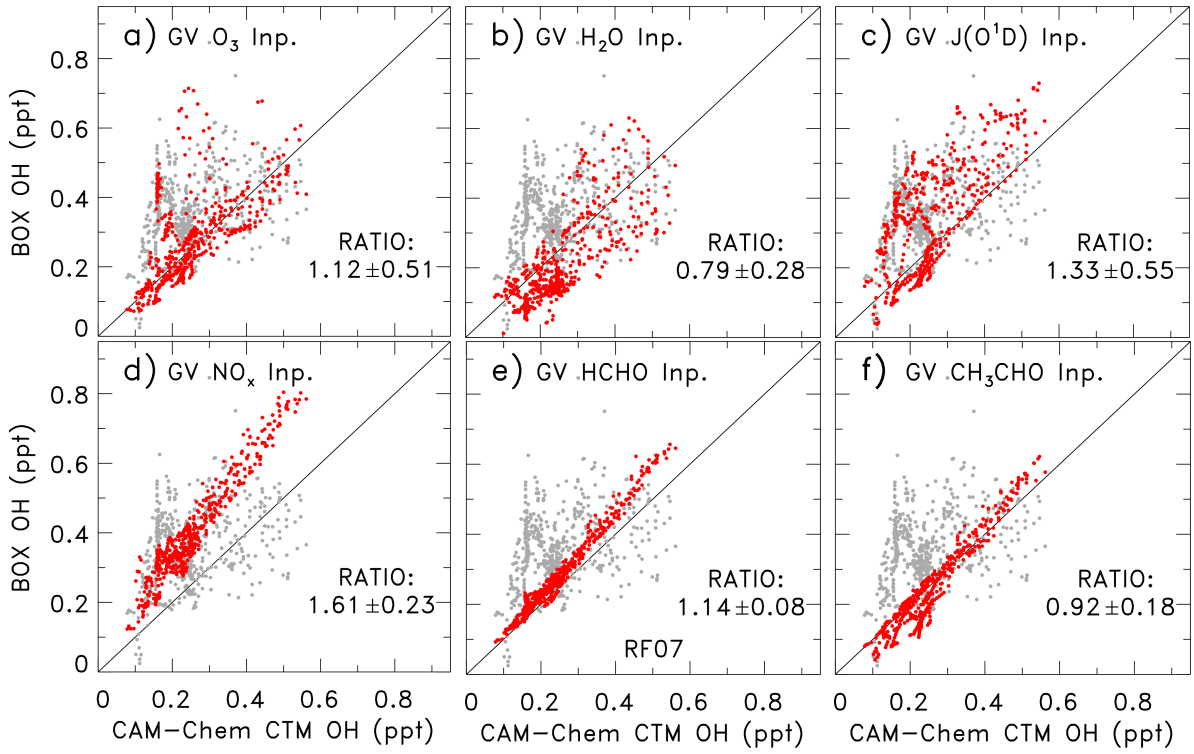

Figure 2-5. Same as scatter plots in Fig. 2-3, except box model is constrained to output from the CAM-Chem CTM for all OH precursors with the exception of the precursor indicated by the label on each plot. Values for the labeled precursor are from CONTRAST (GV) measurements. The OH precursors constrained by measurements are: O_3 (panel a), H_2O (b), $J(O^1D)$ (c), NO (with steady-state NO_2 calculated by the box model to give NO_x) (d), HCHO (e), and CH_3CHO (f). Grey points in the background are the same as those shown in Fig. 2-3b, for the sake of visual comparison. The mean and standard deviation of the ratio (BOX OH)/(CAM-Chem OH) are indicated.

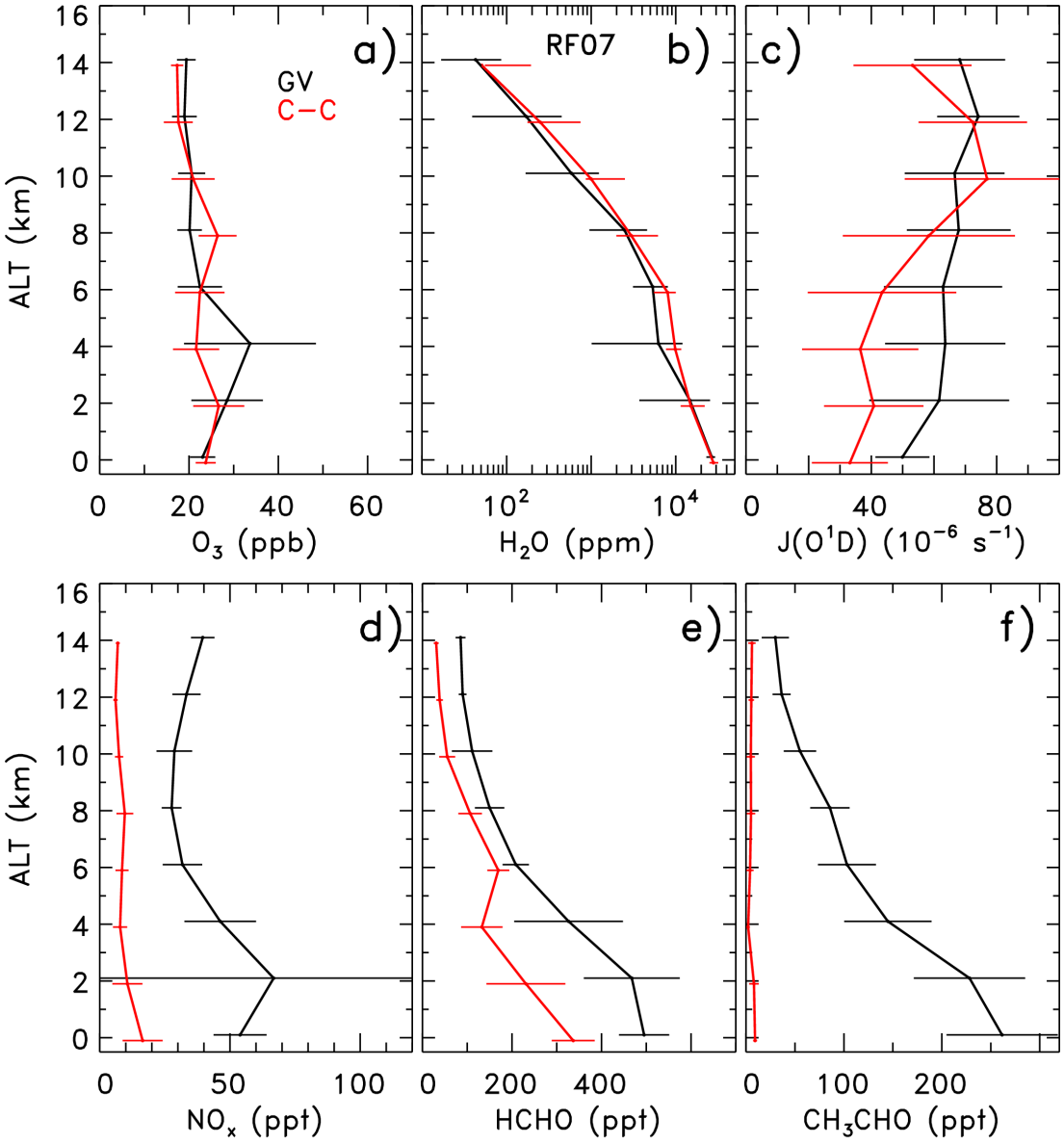

Figure 2-6. Profiles of mean O_3 (panel a), H_2O (b), $J(O^1D)$ (c), NO_x (d), HCHO (e), and CH_3CHO (f) mixing ratio, averaged for CONTRAST RF 07 only, subject to the selection filter for daytime TWP conditions described in Methods. GV observations are shown in black; output from the CAM-Chem CTM, extracted along the flight track to match the time and location of GV observations, is shown in red. Data and model output are averaged within 2 km altitude bins. Error bars show the standard deviation about the mean except for H_2O, where error bars show the 5th and 95th percentiles.

standard deviation of measured (GV, black) or modeled (CAM-Chem, red) profiles, except the NO_x panel. Here, we have added NO_2 found in local, photochemical steady state with GV NO using the DSMACC model constrained to observed NO, to

facilitate the comparison of modeled and measured NO_x ($NO+NO_2$). Finally, **Figure 2-7** shows scatter plots and profiles for CO, C_5H_8, and $J(NO_2)$, which have a small effect (less than 10%) on OH both for RF 07 and all of CONTRAST.

Differences in O_3 and H_2O, related to the placement of HOLW structures in CAM-Chem, are drivers in disagreement between GV and CAM-Chem OH (Figures 2-5a and 2-5b). Direct comparison of O_3 and H_2O mean profiles from observations and from CAM-Chem (Figures 2-4a and b) show this is the case, especially in the mid-troposphere around 3 to 5 km. Vertical profiles in **Figure 2-8** show similar comparisons for the entire CONTRAST campaign, over which time errors model O_3 (Figure 2-8a) and H_2O (Figure 2-8b) average out. The location and vertical extent of these HOLW structures are determined by the interplay of biomass burning, long-range transport, and precipitation [*Anderson et al.*, 2016], which are difficult for any model to represent with high fidelity, particularly in the TWP. As a result, variations between observed and modeled O_3 and H_2O likely arise from differing placements of the HOLW structures, in time and location. The mean ratio of box modeled OH

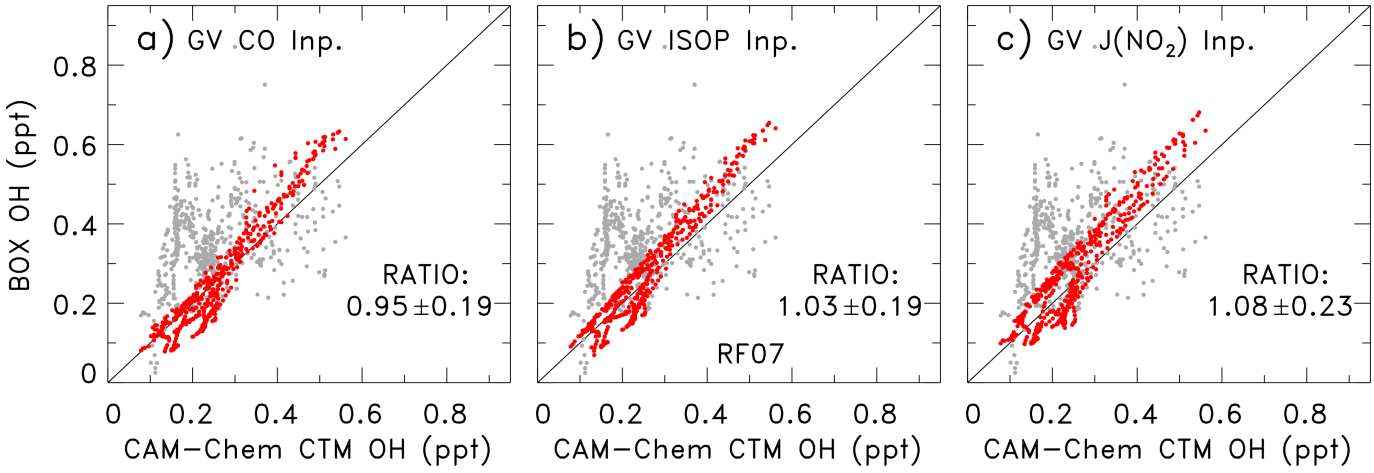

Figure 2-7. Same as Fig. 2-5 except variables used to constrain box model from CONTRAST measurements are CO (panels a and b), C_5H_8 (c, d), HCHO (e, f), $J(NO_2)$ (g, h), and CH_3CHO (i, j).

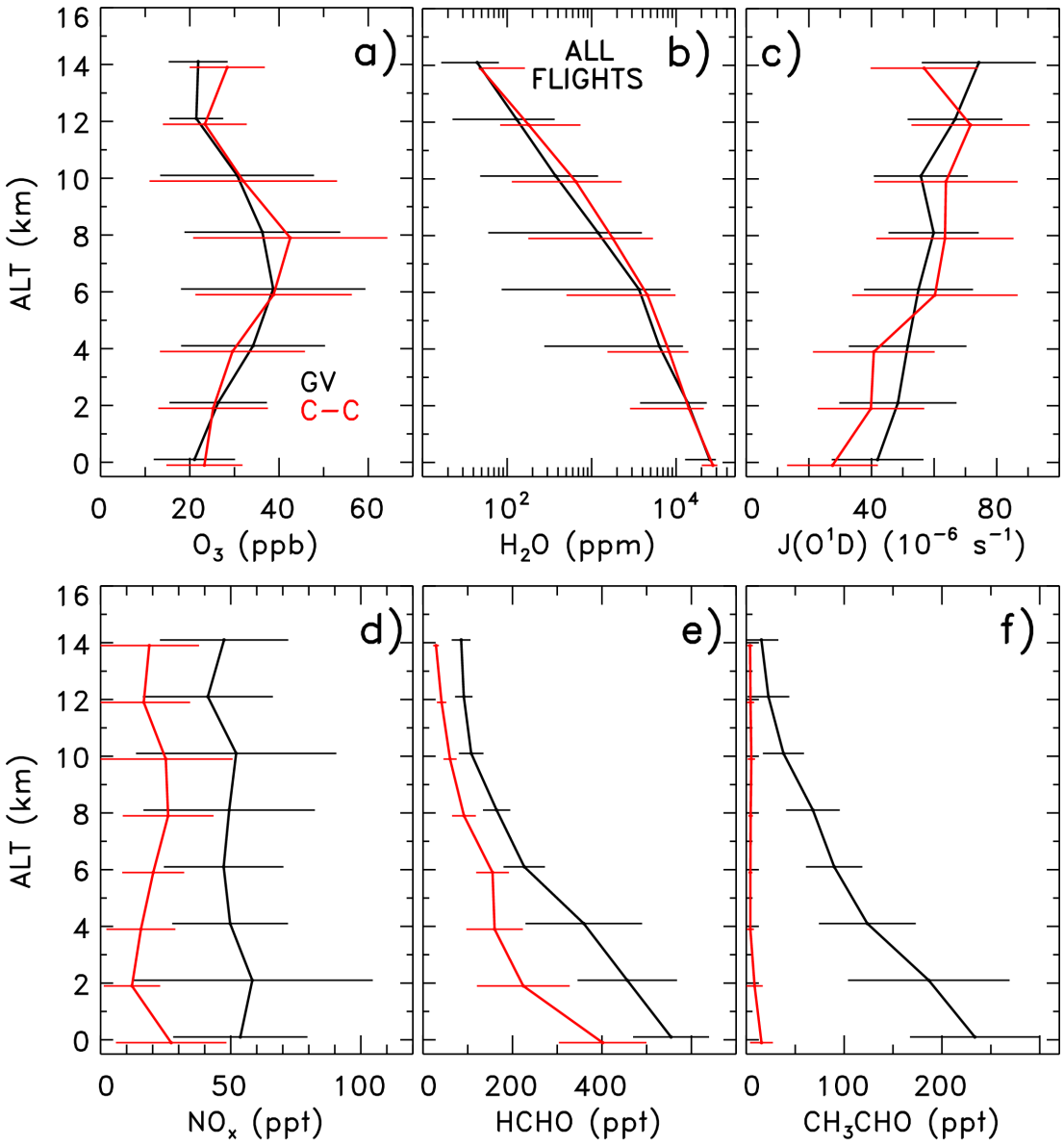

Figure 2-8. Profiles of mean O_3 (panel a), H_2O (b), $J(O^1D)$ (c), NO_x (d), HCHO (e), and CH_3CHO (f) mixing ratio, averaged over the entire CONTRAST campaign, subject to the selection filter for daytime TWP conditions described in Methods. GV observations are shown in black; output from the CAM-Chem CTM, extracted along the flight track to match the time and location of GV observations, is shown in red. Data and model output are averaged within 2 km altitude bins. Error bars show the standard deviation about the mean except for H_2O, where error bars show the 5th and 95th percentiles.

found using GV O_3 to OH from CAM-Chem is 1.12 (Figure 2-5b), while the same ratio for OH found using GV H_2O is 0.79 (Figure 2-5d). Therefore, while O_3 and H_2O drive model versus GV OH differences for specific segments of a flight track,

their net effect is only a slight negative offset in CAM-Chem OH relative to GV OH. The effect of HOLW structures is explored further in Section 2.3.4.

The box model swaps using $J(O^1D)$ from CONTRAST indicate this variable has considerable influence on OH. The distribution of OH (Figure 2-5c) found using $J(O^1D)$ from the GV and all other variables from CAM-Chem shows a clear elevation relative to CAM-Chem OH. The mean ratio of OH calculated using GV $J(O^1D)$ to OH from CAM-Chem is 1.33. Values of $J(O^1D)$ reported during CONTRAST tend to exceed values within CAM-Chem in the lower troposphere whereas CAM-Chem values of $J(O^1D)$ are higher in the mid-troposphere (Figure 2-8c). This difference is likely due to the tendency of the GV to conduct preferential sampling during clear sky conditions: even though a primary goal of CONTRAST was the sampling of the outflow of active convection, the GV avoided flying either within or beneath active convection. In addition, as with HOLW structures, placement of clouds within a global model cannot be expected to match the location of clouds in the real atmosphere. So, we expect to see differences in OH due to inherent differences between GV and model $J(O^1D)$.

The abundance of NO_x also leads to significant differences in GV and CAM-Chem OH. When the box model is constrained to observed NO, calculated OH is 61% higher than CAM-Chem OH (Figure 2-5d). The profile of NO_x inferred from observed NO is significantly larger than CAM-Chem NO_x throughout the troposphere (Figure 2-8d). As shown in Section 2.3.4, all of the POLMIP CTMs also under-estimate observed NO_x. One possible explanation is that emissions of NO_x from biomass burning regions are underestimated by the FINN emission inventory used to

drive CAM-Chem. If so, the various emission inventories used to drive the POLMIP CTMs likely suffer from the same deficit. Additionally, lightning over Africa is responsible for a large source of NO_x in the upper troposphere that could be transported to the TWP following the same pathway as biomass burning plumes [*Jacob et al.*, 1996; *Murray et al.*, 2013; *Anderson et al.*, 2016]. It is important to note that NO_x is likely converted to peroxyacetylnitrate (PAN) during transit from Africa and Southeast Asia to the TWP [*Jacob*, 1999]. Biomass burning plumes descend as they transit from Africa and Southeast Asia to the TWP [*Anderson et al.*, 2016]. As an air parcel descends, NO_x is regenerated upon thermal decomposition of PAN [*Jacob*, 1999]. While these effects related to transport of biomass burning emissions would be expected to have their largest effect in the mid-troposphere, i.e. where HOLW structures occur [*Anderson et al.*, 2016], underestimates of NO_x by CAM-Chem appear constant throughout the tropospheric column in this analysis. Further analysis in Section 2.3.3, however, shows that HOLW structures are likely responsible for large model underestimates of NO_x in the mid- to upper troposphere. Regardless of the cause, the low NO within CAM-Chem is the single largest driver of net differences in OH within this analysis, and we will see this is again the case with the POLMIP models in Section 2.3.4.

The remaining differences in OH, after accounting for the 4 variables above, are almost entirely explained by HCHO and CH_3CHO. Constraining the box model to observations of HCHO incurs a 14% increase above CAM-Chem OH (Figure 2-5e). While HCHO concentrations are underestimated by CAM-Chem throughout the troposphere (Figure 2-8e), most of the difference in OH resulting from the HCHO

swap occurs in the upper troposphere, where OH mixing ratios are lowest. At the highest altitudes of GV sampling, photolysis of HCHO constitutes one of the main sources of OH [*Jaeglé et al.*, 1998], so the larger concentrations of HCHO in the true atmosphere are driving more production of OH than is calculated by CAM-Chem for the upper troposphere. Constraining the box model to GV CH_3CHO, on the other hand, results in an 8% decrease in OH (Figure 2-5f). CAM-Chem drastically underestimates concentrations of CH_3CHO (Figure 2-8f) owing to its lack of oceanic emissions of the chemical. The atmospheric budget of CH_3CHO includes a large oceanic source [*Singh et al.*, 2003; *Singh et al.*, 2004; *Millet et al.*, 2010]. The effect of this on OH manifests predominantly in the lower troposphere, where OH serves as a sink for CH_3CHO and vice versa. Higher values of CH_3CHO in the true atmosphere relative to CAM-Chem result in lower concentrations of OH. Acetaldehyde is also an important source of HCHO [*Singh et al.*, 2004]; however, a limitation of this box modeling method prevents us from probing the effect of CH_3CHO on OH through HCHO. Lifting the box model constraint to HCHO results in the decay of [HCHO] to 0 over the course of a steady state simulation. However, our research group is currently conducting more in-depth research on the production and loss pathways of HCHO observed during CONTRAST.

In addition to the 6 OH precursors discussed above, observed values of CO, C_5H_8, and $J(NO_2)$, were also analyzed using the box model swap method. These variables exhibited little influence on modeled OH. Swaps for each of these variables for RF 07 show structures and correlations similar to the box model simulation constrained only to inputs from CAM-Chem (Figure 2-7).

Consideration of all flights produces similar results as seen through calculations of tropospheric OH columns (**Table 2-1**). Because swaps are performed with a backdrop of CAM-Chem constraints, i.e. all model inputs are from CAM-Chem except for the variable being examined (from GV observations), the OH column values are compared to the CAM-Chem box model simulation. The ratio of column values for swap run "X" to the CAM-Chem run represents the fractional difference in OH caused by variable "X". The C_5H_8 and $J(NO_2)$ ratios confirm that little to no change in OH results from differences in these variables, driving 1% and 2% elevations of OH, respectively. The CO ratio, though, reveals a larger effect on OH than was seen in RF 07. Across the campaign, constraint to observed CO causes a 6% drop in OH. Carbon monoxide is a sink for OH, so an OH deficit resulting from the underestimation of CO by CAM-Chem, apparent in **Figure 2-9,** is reasonable.

Table 2-1. Tropospheric OH Columns Calculated for the CONTRAST Mean OH Vertical Profile and CAM-Chem Model Simulations

C-C Box Model Run	OH Column (10^{12} cm^{-2})[a]	Ratio (Run X / C-C)
GV	2.17	1.12
C-C (CONTRAST)	1.94	---
C-C, GV NO_x	2.61	1.35
C-C, GV H_2O	1.61	0.83
C-C, GV $J(O^1D)$	2.16	1.11
C-C, GV CH_3CHO	1.77	0.91
C-C, GV O_3	2.06	1.06
C-C, GV CO	1.83	0.94
C-C, GV HCHO	2.01	1.04
C-C, GV $J(NO_2)$	1.97	1.02
C-C, GV C_5H_8	1.95	1.01
GV, C-C $J(O^1D)$+$J(NO_2)$	1.92	0.99

[a]Columns are integrated from the surface to 13 km

The 6 OH precursors that describe the bulk of the difference between GV and CAM-Chem OH — O_3, H_2O, $J(O^1D)$, NO_x, HCHO, and CH_3CHO — have effects on OH similar to those discussed above when considered across the entire campaign. Through calculations of tropospheric column OH (Table 2-1), we find the influence of NO_x differences on OH is the largest with a 35% increase in OH resulting from constraint to observed NO. Water vapor drives the largest decrease in OH at −17%. Changes in OH resulting from use of observed $J(O^1D)$, CH_3CHO, O_3, and HCHO are +11%, −9%, +6%, and +4%, respectively. Of these, the effects of CH_3CHO and H_2O are closest in magnitude to those examined for RF 07 (mean ratio values noted in Figure 2-5). The effects of NO_x, $J(O^1D)$, O_3, and HCHO preserve the sign of change, but are diminished in magnitude. This may indicate the averaging out of atmospheric features—e.g. biomass burning or clouds—that occurs when analyzing the entire campaign.

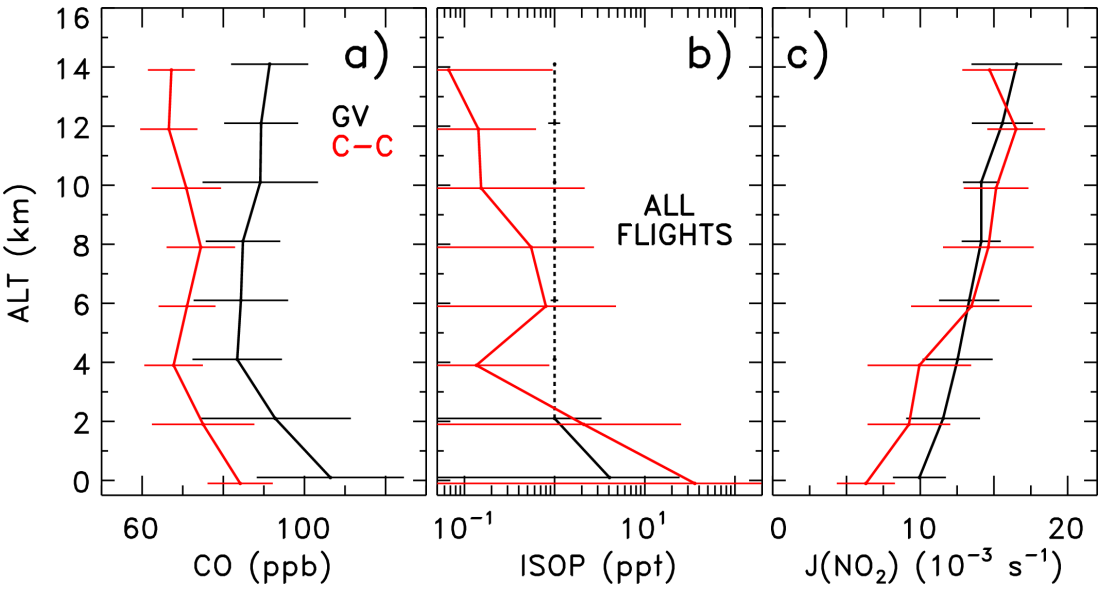

Figure 2-9. Same as Fig. 2-8 except for the variables CO (panel a), C_5H_8 (panel b), and $J(NO_2)$ (panel c). In the isoprene panel, the black dotted line depicts altitude bins for which the mean value of C_5H_8 observed aboard the GV lies within 1 standard deviation of the limit of detection.

The final CAM-Chem swap simulation performed using the box model is shown in the final entry of Table 2-1. The box model was constrained to CAM-Chem values of $J(O^1D)$ and $J(NO_2)$ along with GV observations of the remaining inputs. The close agreement with the "all CAM-Chem" run of the box model (within 1%) that this simulation achieves suggests that the sampling bias described above largely accounts for the OH discrepancies between GV and CAM-Chem OH. However, there still exist large biases in OH due to compensating factors (i.e. NO_x and H_2O) that remain problematic.

We have also evaluated the effect of measurement uncertainties on the box modeled OH fields. **Figure 2-10** shows the effect on OH resulting from a $\pm 2\sigma$ perturbation of O_3, NO, $J(O^1D)$, and $J(NO_2)$ calculated by the box model. Uncertainty in the measurement of O_3 is unlikely to influence our calculation of OH significantly with <5% variation in OH resulting from the perturbation test. Uncertainty in the NO measurement, however, could affect OH calculations by as much as 20%, $J(O^1D)$ by 20%, and $J(NO_2)$ by ~10%. Performing a root sum of squares analysis on the fractional differences for both the positive and negative OH perturbations produces a total uncertainty of ±29.2%. While it is possible to propagate measurement uncertainties throughout the entirety of our analysis, this would require significantly more computation time. Though the measurement uncertainties propagate to large uncertainties in our box model calculation of OH, they are still not large enough to account for the difference in GV and CAM-Chem OH.

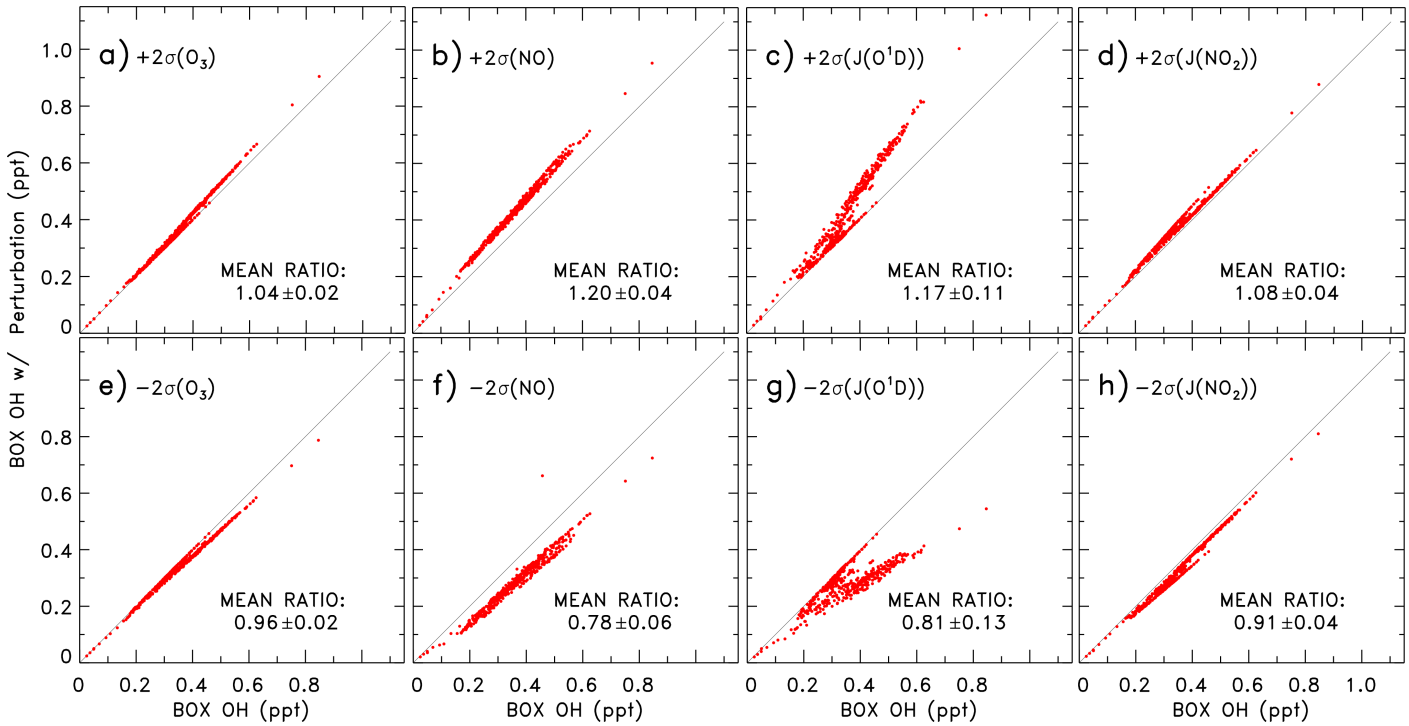

Figure 2-10. OH mixing ratios at the time of aircraft observation from sensitivity runs of the DSMACC box model constrained to CONTRAST GV observations, using measurement uncertainties to perturb a single variable in a positive (panels a, b, c, and d) or negative (panels e, f, g, and h) direction, versus OH from the base run of the box model constrained to GV observations for RF 07. Panels a) and e) show 2σ perturbations applied to O_3, b) and f) show 2σ perturbations applied to NO, c) and g) show 2σ (±50%) perturbations applied to $J(O^1D)$, and d) and h) show 2σ (±24%) perturbations applied to $J(NO_2)$. The black line on the scatter plot is the 1:1 line. The mean ratio of $OH_{PERTURBED}$:OH_{BASE} is noted on each plot.

2.3.3 Campaign-wide Results for TWP OH and CH_2Br_2 Lifetime

Values of OH calculated for the entire CONTRAST campaign, RFs 04-15, using the latitude, longitude, and SZA filter described in Section 2.2.1 are aggregated to better understand the oxidizing capacity of the TWP troposphere. **Figure 2-11** shows scatter plots of OH mixing ratios calculated by the DSMACC box model, constrained to GV observations of OH precursors, versus CAM-Chem OH (Figure 2-11a) as well as OH calculated by the box model constrained to precursors from CAM-Chem versus CAM-Chem OH (Figure 2-11b). Figures 2-11c and 2-11d show

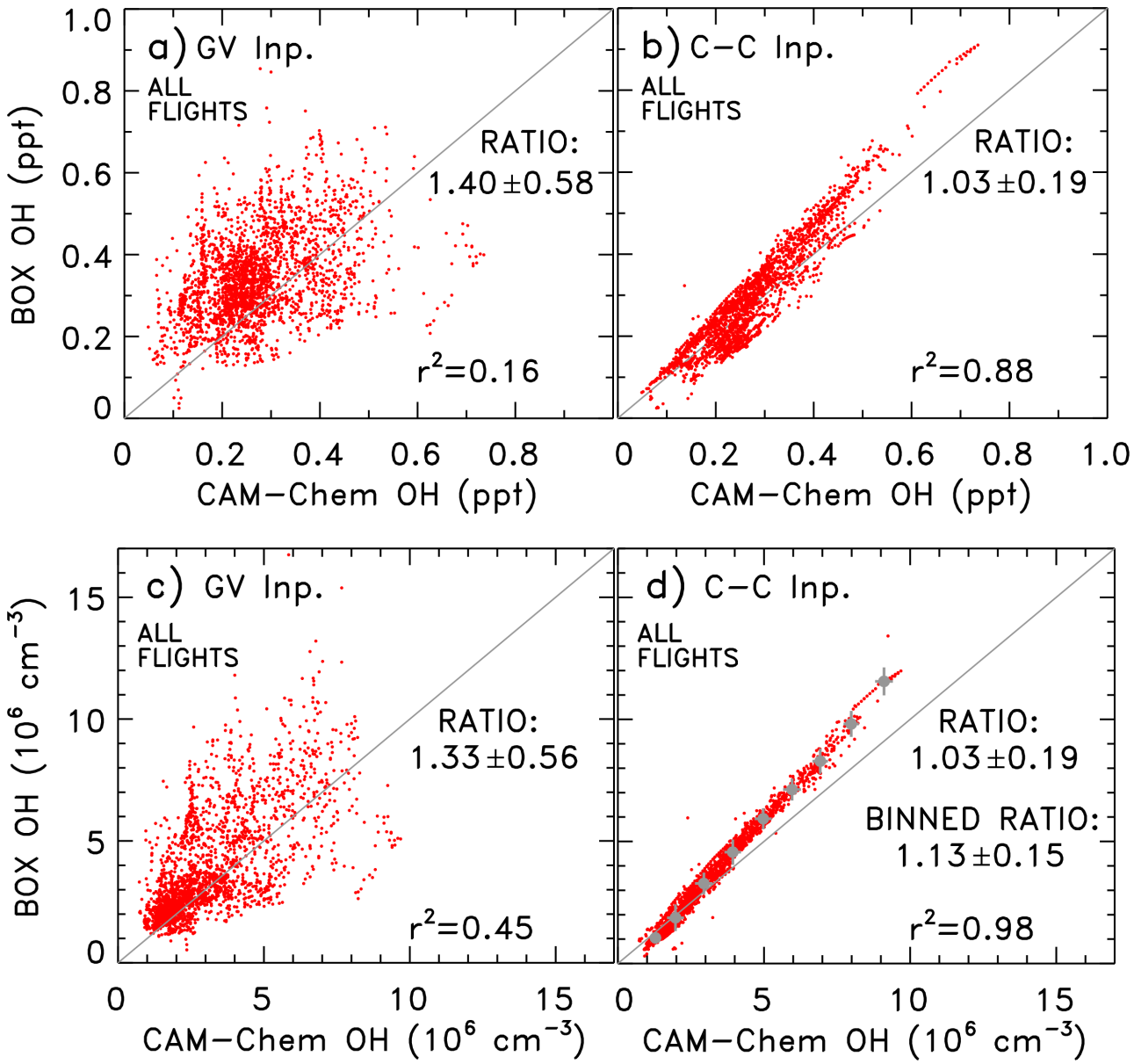

Figure 2-11. Correlation plots of box modeled OH versus CAM-Chem CTM OH for the entire CONTRAST campaign, with application of the following filter used to select daytime observations in the TWP: 132°E < longitude < 162°E, 0°N < latitude < 20 °N latitude, SZA ≤ 60°. (a) Box modeled OH found using constraints for OH precursors from the CONTRAST GV observations; (b) box modeled OH found using constraints from CAM-Chem CTM. Panels (c) and (d) are the same as panels (a) and (b), respectively, except OH is represented as number density instead of mixing ratio. The square of the correlation coefficient (r^2) and the mean and standard deviation of the ratio (BOX OH)/(CAM-Chem OH) are indicated. Panel d) also shows statistics performed by averaging the CAM-Chem OH values within 1×10^6 cm^{-3} interval bins; the mean BOX OH values are determined for those bins and the resulting mean and standard deviations are shown in grey. The ratio of (BOX OH)/(CAM-Chem OH) for the grey points is indicated as the "binned ratio".

corresponding plots of [OH] in units of number density. All results are for the local solar conditions of each observation. The mean ratio of GV OH to CAM-Chem OH

is 1.40 ± 0.58, indicating that OH constrained by the CONTRAST observations is on average 40% higher than CAM-Chem OH. Results from the previous section suggest that this difference is due to NO_x, H_2O, $J(O^1D)$, CH_3CHO, O_3, CO, and HCHO. The column OH calculation introduced in Section 2.3.2, however, suggests that GV exceeds CAM-Chem OH by only 12% (Table 2-1). This may result from integrating values of binned 24-hour average [OH]. High values of the "BOX OH:CAM-Chem OH" given equal weight as other data points in the reported mean ratio (Figures 2-11a and c) are effectively removed from the column calculation by first averaging the OH output within altitude bins. Large differences in upper tropospheric GV and CAM-Chem OH are also given less weight in the column calculation due to the lower air density at altitude.

The chemical mechanisms used in the two models are also responsible for a portion of the difference: constraining the box model to OH precursors from CAM-Chem results in a mean ratio of only 1.03 ± 0.19 and (Figures 2-11b and 2-11d). However, this analysis is weighted heavily toward the lowest [OH] values (between 1×10^6 and 5×10^6 cm^{-2}) due to more frequent aircraft sampling at high altitudes. Recalculating the ratio of box modeled CAM-Chem OH to OH from CAM-Chem CTM using a binning approach (grey points, Figure 2-11d) places equal weight on the higher values of OH that occur at lower altitudes. This ratio is 1.13 ± 0.15, so we conclude that the effect of differences between the box model and CAM-Chem chemical mechanisms on OH lies between 3% and 13%.

We now transition to analyzing 24-hour average OH values calculated as vertical profiles of the campaign-wide results. Vertical distributions and 24-hour

averages of OH provide the context for interpreting our results in a manner that is meaningful for examining the oxidizing capacity of the troposphere. Our calculations of vertical, 24-hour mean GV OH and CAM-Chem indicate that the largest differences occur in the lower (below ~3 km) and upper (above ~10 km) troposphere (**Figure 2-12**). Figure 2-12a shows vertical mean mixing ratios of OH. Here, output of 24-hour average OH was not provided from CAM-Chem. Our box model reproduction of CAM-Chem OH enables us to approximate what the CAM-Chem model would have likely supplied as its daily mean OH. Thus, when results show a comparison between CAM-Chem and GV 24-hour average OH or derivatives thereof, the CAM-Chem value is obtained from the "all CAM-Chem" box model run described in Section 2.2.3.

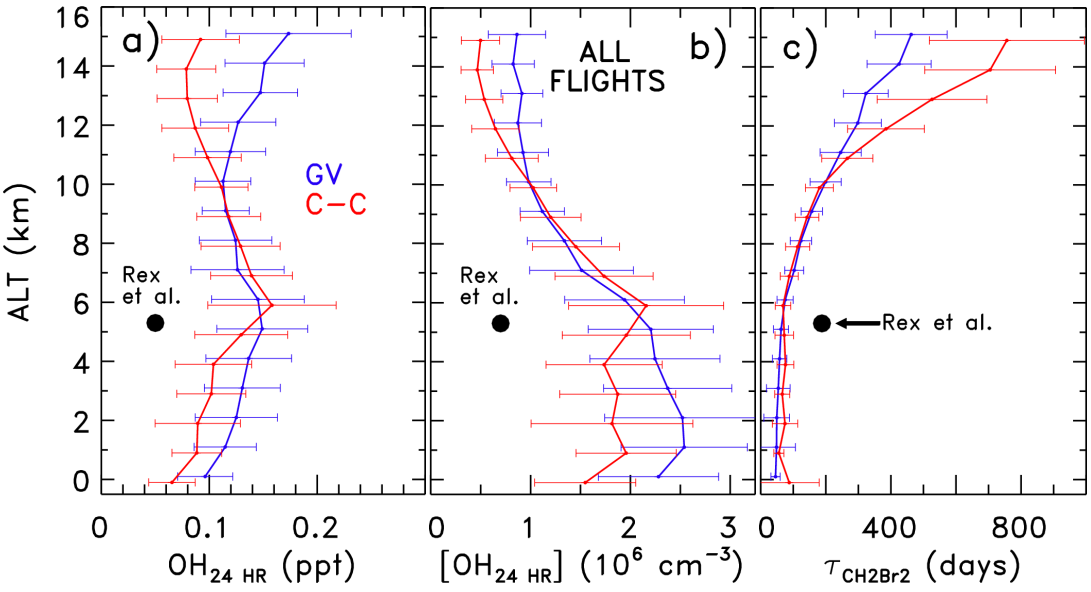

Figure 2-12. 24 hour average OH ($OH_{24\ HR}$) and lifetime of CH_2Br_2 (τ_{CH2Br2}) from the DSMACC box model for the entire CONTRAST campaign, subject to 132°E < longitude < 162°E, 0°N < latitude < 20 °N latitude, SZA ≤ 60°, separated into 1 km altitude bins. Panel a) shows $OH_{24\ HR}$ mixing ratio; panel b) shows $OH_{24\ HR}$ number density; panel c) shows τ_{CH2Br2} with respect to loss by OH. Blue line denotes box model $OH_{24\ HR}$ and τ_{CH2Br2} for runs constrained to GV measurements; red line denotes box model $OH_{24\ HR}$ for runs constrained to CAM-Chem output. Error bars signify standard deviation about the mean of $OH_{24\ HR}$ and τ_{CH2Br2}, for each altitude bin. Error bars are offset slightly in altitude for clarity. We also show $OH_{24\ HR}$ and τ_{CH2Br2} at 500 hPa (which we place at 5.3 km altitude) reported by *Rex et al.* [2014] above the equator on 1 October 2009.

The OH difference at low altitudes is primarily a result of CAM-Chem underestimation of NO_x and the GV sampling bias of $J(O^1D)$ (see discussion in Section 2.3.2), while the difference at high altitude is a result of CAM-Chem underestimation of HCHO (Figure 2-5e) in addition to CAM-Chem underestimation of NO_x. The good agreement between GV and CAM-Chem OH in the mid-troposphere occurs despite the CAM-Chem underestimation of NO_x; the effects of underestimated H_2O compensate by decreasing OH in the 4 to 10 km range. Also, Figure 2-12a contains the 24-hour average mixing ratio of OH at 500 hPa (~5.3 km) associated with the 188 day value for τ_{CH2Br2} at this pressure reported by *Rex et al*. [2014] (albeit, for October 2009). As discussed in detail below, neither GV nor CAM-Chem OH (for January and February 2014) are consistent with the middle troposphere OH minimum suggested by *Rex et al*. [2014].

Figure 2-12b shows vertical profiles of the 24-hour average number density of OH ($[OH_{24hr}]$) inferred from GV observations and CAM-Chem output. Since air pressure declines with increasing altitude, the differences in $[OH_{24hr}]$ above 10 km are smaller in magnitude relative to the total tropospheric column than the difference in the 24-hour average OH mixing ratios (Figure 2-12a). In terms of the OH number density, the tendency of CAM-Chem NO_x and $J(O^1D)$ to fall below mean observations at low altitude tends to have a larger effect than the tendency of CAM-Chem HCHO to lie below observations at high altitudes (Figure 2-12b). Both $[OH_{24hr}]$ from the GV and from CAM-Chem are considerably larger than the value at 500 hPa suggested by *Rex et al*. [2014].

Figure 2-12c shows the profiles of τ_{CH2Br2} associated with the GV and CAM-Chem profiles of [OH_{24hr}]. The lifetime of CH_2Br_2 (Figure 2-12c) is ~66 days at 5.3 km, ~200 days at 10 km, and increases to more than 400 days above 14 km. As can be inferred from the [$OH_{24\ HR}$] comparisons, CAM-Chem overestimates τ_{CH2Br2} at low altitudes (below ~3 km) and at high altitudes (above 10 km). Throughout the mid-troposphere (4 to 10 km), τ_{CH2Br2} calculated from CAM-Chem shows good agreement with that calculated using the GV observations. *Rex et al.* [2014] calculated a value of 188 days for τ_{CH2Br2} at 500 hPa for October 2009 using the GEOS-Chem CTM. This value is noted on Figure 2-12c and exceeds both the GV-based and CAM-Chem values of τ_{CH2Br2} by more than a factor of 2. As shown below, seasonal differences (January–February for CONTRAST versus October for *Rex et al*. [2014]) account for only a small portion of this difference. Therefore, our analysis is not consistent with the *Rex et al*. [2014] suggestion of an "OH hole" (i.e., steep minimum relative to adjacent regions) in the TWP.

Many factors influence the abundance of tropospheric OH. The primary production of OH depends on the concentrations of O_3 and H_2O, as well as the photolysis frequency of $O_3 \rightarrow O(^1D)$. In addition, low NO_x can suppress OH, as HO_x (=OH+HO_2) tends to preferentially exist as HO_2 rather than OH under this condition [*Gao et al.*, 2014]. *Rex et al.* [2014] suggested the occurrence of very low OH in the TWP (Figure 2-12a, b) was driven by mixing ratios of O_3 lying close to zero (and well below 20 ppbv), based on ozonesonde observations and supported by the output from GEOS-Chem. *Gao et al*. [2014] suggested low NO_x reported in an air parcel traced back to the TWP could also be responsible for very low OH in the TWP.

CONTRAST observations provide a means to independently assess the impact on O_3, H_2O, and NO_x on OH. The mixing ratio of O_3 tended to exhibit two modes: a primary mode narrowly distributed around 20 ppbv associated with high relative humidity (RH > 70%) and a secondary mode with mixing ratios above 40 ppb and RH < 20% [*Pan et al.*, 2015]. The primary mode is attributed to the outflow of recent convection of relatively clean maritime air, and is hereafter referred to as the background (BGND) mode. *Newton et al*. [2015] have focused on details of ozone sonde calibration as being an explanation for near zero levels of O_3 reported by *Rex et al*. [2014] in contrast to the ~20 ppb minimum for O_3 observed consistently throughout the TWP by the GV aircraft. *Anderson et al*. [2016] have attributed the secondary HOLW mode to long-range transport of biomass burning plumes, which exhibit low RH due to descent during transit to the TWP. Regardless of their origin, HOLW structures are characterized by higher NO_x compared to the BGND mode.

Following *Anderson et al*. [2016], we define the criteria for background conditions as RH > 70%, O_3 < 25 ppb and the criteria for HOLW structures as RH < 20%, O_3 > 40 ppb. Values of 24-hour average OH calculated for observations that meet the HOLW criteria are generally lower than OH calculated for BGND air parcels (**Figure 2-13a**). The value of NO_x in the HOLW structures exceeds that of BGND air by at least a factor of ~2 above 4 km (Figure 2-13b). This means low OH is calculated *despite* the existence of high O_3 and elevated NO_x; instead, the low H_2O of these HOLW structures is the dominant factor limiting production of OH. This finding is contrary to the suggestions of *Rex et al.* [2014] and *Gao et al.* [2014]; the CONTRAST observations are inconsistent with the near zero O_3 of the former study

and the suppressed NO_x of the latter study. CONTRAST mixing ratios of O_3 fell below the 20 ppb threshold highlighted by *Rex et al.* [2014] 36% of the time. Whereas *Rex et al.* [2014] saw O_3 well below 15 and even 10 ppb, CONTRAST O_3 only fell below 15 ppb ~3% of the time. Likewise, concentrations of NO only reached values observed by *Gao et al.* [2014] 3.5% of the time in the same altitude range (9 to 15 km; **Figure 2-14**). Additionally, CAM-Chem exhibits some skill in producing HOLW structures (Figure 2-13c), but the magnitude of NO_x enhancement in these structures is only half that of the observations.

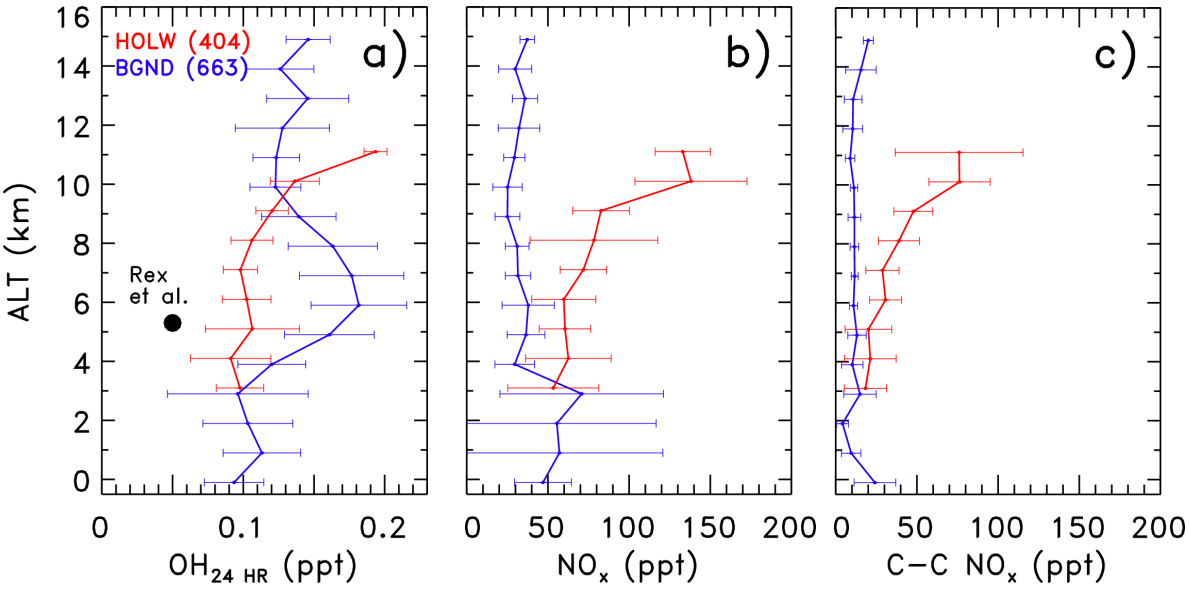

Figure 2-13. Profiles of $OH_{24\,HR}$ (panel a) and NO_x (panel b from GV and c from C-C) mixing ratios for all examined flights, separated by occurrence (red) and absence (blue) of high O_3/low H_2O (HOLW) structures. $OH_{24\,HR}$ is calculated by the DSMACC box model constrained to CONTRAST measurements within the same modeling domain as all of the prior figures, with the additional constraint that data are acquired either for background conditions (i.e. the low O_3, high H_2O mode) or for HOLW structures. NO_x is found using box model calculation of 24-hour average NO and NO_2 based on GV observations of NO, O_3, $J(NO_2)$, and hydrocarbons. Criteria for these two modes are O_3 < 25 ppb, RH > 70% (background) and O_3 > 40 ppb, RH < 20% (HOLW structure). Again, error bars represent 1 standard deviation about the mean of the respective $OH_{24\,HR}$ values within 1 km altitude bins and are offset slightly with respect to altitude for clarity. The parenthetical numbers represent the number of model simulations that went into each profile.

2.3.4 Comparison to POLMIP Models

Here we compare GV OH to archived fields of OH from eight CTMs that participated in POLMIP. The POLMIP runs used meteorology and emissions for 2008 and the archive consists of monthly mean fields. As detailed below, conclusions drawn from the POLMIP comparisons are consistent with the findings based on the comparison to CAM-Chem run in CTM mode for winter 2014, from which species abundances along the GV flight track can be obtained (Section 2.3.3).

Here we compare GV OH to archived fields of OH from eight CTMs that participated in POLMIP. The POLMIP runs used meteorology and emissions for 2008 and the archive consists of monthly mean fields. As detailed below, conclusions drawn from the POLMIP comparisons are consistent with the findings

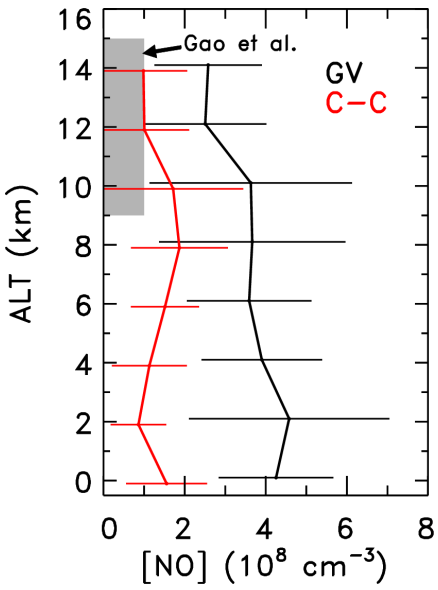

Figure 2-14. Profiles of [NO] averaged in 2 km altitude bins from all observations in the CONTRAST campaign, subject to the daytime TWP filter described in Methods (black line) and extracted from the CAM-Chem CTM for the times and locations of observation (red). The grey shaded region depicts the values of [NO] observed by *Gao et al.* [2014]. About 3.5% of measurements of [NO] made between 9 and 15 km during CONTRAST fall within the *Gao et al.* [2014] range.

based on the comparison to CAM-Chem run in CTM mode for winter 2014, from which species abundances along the GV flight track can be obtained (Section 2.3.3).

Figures 2-15 and **2-16** show comparisons of POLMIP monthly mean OH mixing ratio, OH number density, as well as OH precursors and related species to 24-hour average values of these quantities inferred from GV measurements during CONTRAST. The top row of Figures 2-15 and 2-16 show results from individual CTMs, whereas the bottom row shows results from the POLMIP multi-model mean (MMM). All POLMIP results shown in these two figures use averages of January and February 2008 monthly means for all model output that lies within the TWP boundary region shown in Figure 2-1; i.e., the POLMIP archive is sampled at the same season and location as the CONTRAST campaign (albeit, for a different year). We use the vertical coordinate of pressure, because the POLMIP archive only provides output on a pressure grid. For the diurnally varying quantities OH, NO_x, $J(O^1D)$, and $J(NO_2)$, the 24-hour average value from CONTRAST are campaign-wide averages of the 24-hour average output of DSMACC box model runs constrained to aircraft observations, whereas for HCHO the estimate of 24-hour average value is based on scaling factors from the University of Washington Chemical Model (UWCM) model [*Wolfe and Thornton*, 2011] in which HCHO concentrations vary diurnally (which is not the case for the DSMACC box model). Additionally, POLMIP values of C_5H_8 are represented in Figure 2-15e as the median C_5H_8 concentrations from the individual models, and in Figure 2-15j as the multi-model mean of those median values. This is done to prevent the non-Gaussian distribution

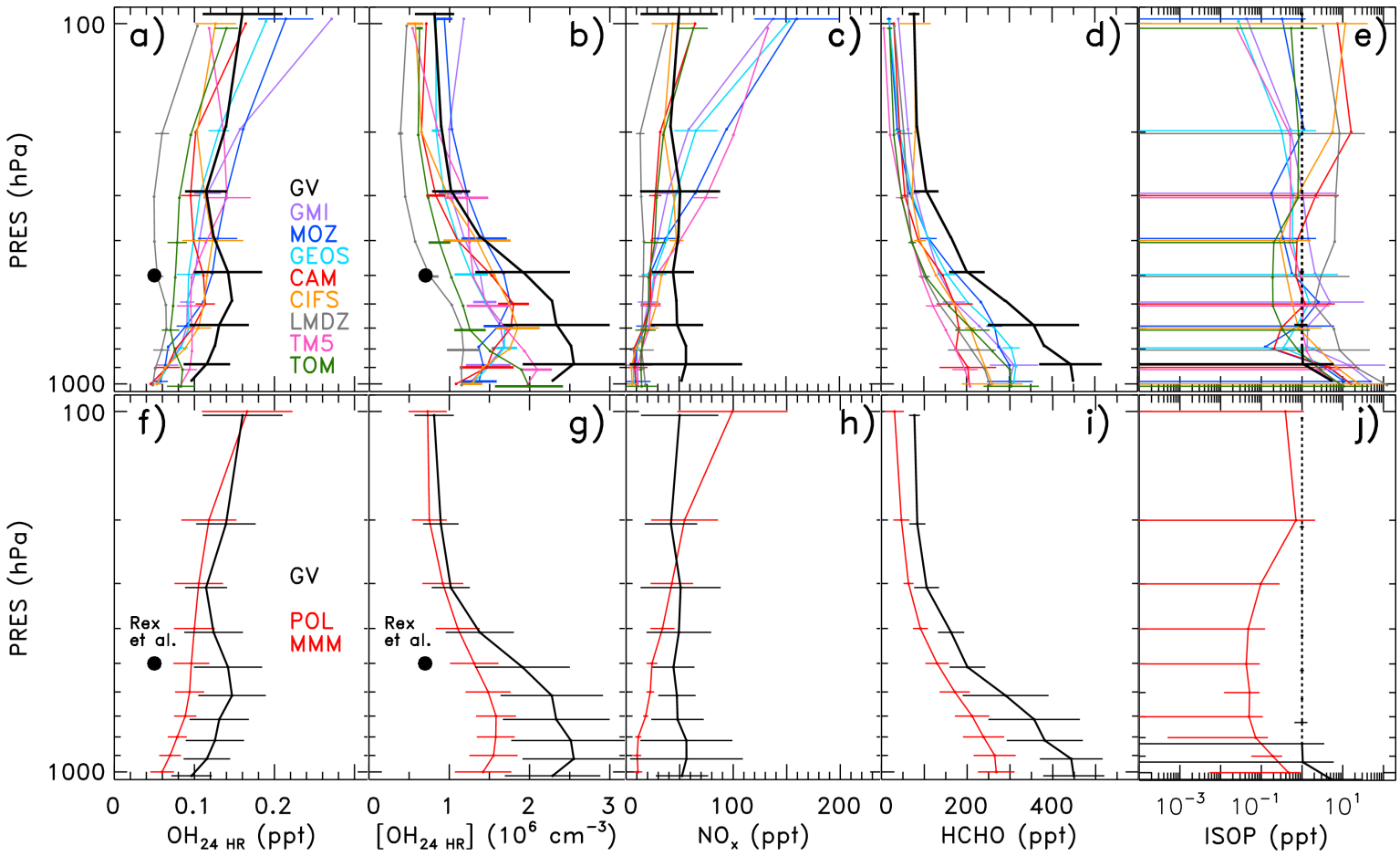

Figure 2-15. Profiles of monthly mean OH mixing ratio (panels a and f), OH concentration (b, g), NO_x (c, h), HCHO (d, i), and C_5H_8 (e, j) from the POLMIP archive for 8 CTMs (colored lines) for January and February 2008. The black solid lines, described in greater detail below, represent either inferred OH or GV observations. The upper set of panels shows profiles from each POLMIP CTM, while the lower set shows the POLMIP multi-model mean. Error bars show 1 standard deviation about the mean of the various quantities, in 100 hPa pressure bins; they are offset slightly in the vertical for clarity. For the top panels, some of the error bars are omitted to avoid clutter. The black solid lines show 24-hour mean OH mixing ratio (panels a and f) and OH concentration (b, g) output from the DSMACC box model constrained by GV inputs. The same latitude/longitude filter, specific to the TWP, has been applied to the POLMIP archive and inferred OH values. In addition, the inference of $OH_{24\ HR}$ is based only on daytime data. The OH panels also show the October 2009 value at 500 hPa in the TWP from *Rex et al.* [2014]. The black solid lines for NO_x are 24-hour averages of the diel output (15 minute grid) of NO plus NO_2 from DSMACC, for calculations constrained to match observed NO at the SZA of observation. The black solid lines for HCHO also represent 24-hour average values, which in this case are found by scaling the observed HCHO to $HCHO_{24\ HR}$ using the UWCM chemical box model (see text). The scaling for HCHO is close to unity at all altitudes because the photochemical lifetime of HCHO is on the order of a few hours (see Figure 2-20). The CTM/observation comparison for C_5H_8 (ISOP) is handled in a different manner. The top plot (panel e) compares the mean and standard deviation from each CTM to the observed mean and standard deviation; often, C_5H_8 was below the limit of detection of the TOGA instrument, 1 ppt, because our analysis is focused on the remote TWP. The black dotted line depicts pressure bins for which the mean value of C_5H_8 lies within 1 standard deviation of the limit of detection. C_5H_8 from the POLMIP CTMs in panel j) (red line) is represented as the multi-model mean of the median values, due to the non-Gaussian distribution of values in the TWP region.

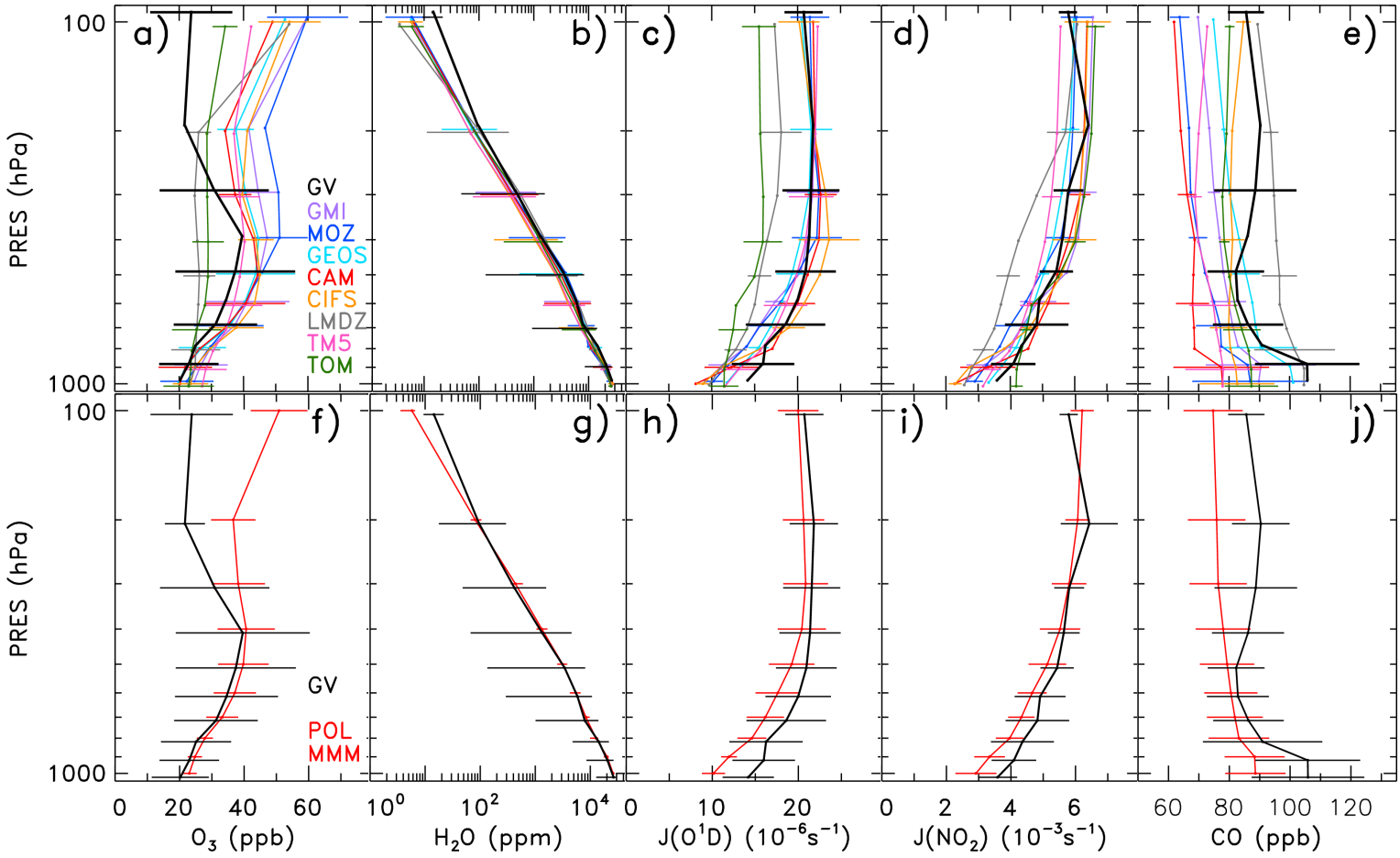

Figure 2-16. Same as Figure 2-15, except for O_3 (panels a and f), H_2O (b, g), $J(O^1D)$ (c, h), $J(NO_2)$ (d, i), and CO (e, j) from observations and from the 8 POLMIP CTMs. The comparisons for O_3, H_2O, and CO show the monthly mean values from the POLMIP archive for January and February 2008 and the mean profiles observed during CONTRAST, since all of these quantities have long photochemical lifetimes. The plots for $J(O^1D)$ and $J(NO_2)$ compare monthly mean values from the POLMIP archive to 24 hour averages of the diel output (15 minute grid) of $J(O^1D)$ and $J(NO_2)$ from DSMACC, for calculations constrained to match observed $J(O^1D)$ and $J(NO_2)$ at the SZA of observation. Error bars show 1 standard deviation about the mean, except for H_2O, where error bars represent the 5th and 95th percentiles.

of C_5H_8 concentrations, influenced by transport of air with high C_5H_8 from nearby landmasses, from exerting an artificial high bias.

The profiles of monthly mean OH in the TWP from the individual POLMIP models (Figures 2-15a and b) all lie below the campaign wide GV-based 24-hour average OH profile, from the surface to ~500 hPa (about 5 km). There is considerable variation in monthly mean OH in the TWP among the POLMIP models,

which is consistent with the results of other model intercomparison studies [*Shindell et al.*, 2006; *Fiore et al.*, 2009; *Voulgarakis et al.*, 2013]. We also show the *Rex et al.* [2014] estimate of OH at 500 hPa (circle, Figures 2-15a, b, f, and g). The LMDZ CTM is in close agreement with OH from *Rex et al.* [2014] due to low NO_x, O_3, and $J(O^1D)$ (Figures 2-15c, 2-16a, and 2-16c); all other CTMs have archived values of OH considerably higher than the *Rex et al.* [2014] estimate.

The comparison of OH precursors and related species from the POLIMP archive (year 2008) to GV observations reveals similar tendencies as found for the CAM-Chem CTM using meteorology and emissions for 2014 (Section 2.3.3) (Figures 2-15c to 2-15e; Figures 2-16a to 2-16e). The observed levels of NO_x (Figure 2-15c) and HCHO (Figure 2-15d) between the surface and 500 hPa are much larger than found in any of the POLMIP CTMs, similar to the discrepancy between the GV observations and output of CAM-Chem run for 2014 meteorology (Section 2.3.3). There is considerable spread in the profile of O_3 among the CTMs (Figure 2-16a). For most of the troposphere the observed profile of O_3 lies within the CTM distribution; however, between 100 and 200 hPa, observed O_3 is consistently lower than all of the CTM values. The lowest values of O_3 for much of the TWP troposphere are reported by LMDZ, which is consistent with the small values of OH from this CTM. Similarly, the observed profile of H_2O is within the range of CTM values for altitudes below ~200 hPa (Figure 2-16b). Between 100 and 200 hPa, observed H_2O is consistently higher than all of the CTM values. These comparisons suggest that the mean state of O_3 and H_2O in the TWP, from the surface to ~200 hPa, is represented well within most of the POLMIP CTMs. The comparisons of O_3 and

H_2O between 100 and 200 hPa suggest a stronger influence of active convection (which deposits O_3 deficient, nearly saturated air) in the TWP during January and February 2014 than simulated by the POLMIP CTMs for winter 2008.

We examine the effect of OH precursor differences between CONTRAST and the POLMIP CTMs by performing box model swap simulations, as were performed with CAM-Chem (described in Section 2.2.3). The multi-model mean of each monthly OH precursor (O_3, H_2O, CO, C_5H_8, HCHO, CH_3CHO, NO_x, $J(O^1D)$, and $J(NO_2)$) are input individually to the DSMACC box model, which is otherwise constrained to GV observations. As in Figure 2-15j, however, C_5H_8 is calculated as the median value within the POLMIP models rather than the mean. Scaling factors are applied to those species with significant diurnal variations. Since this configuration of the DSMACC box model requires constraints be specified at a specific local solar time, the monthly mean values of POLMIP HCHO, NO_x, $J(O^1D)$, and $J(NO_2)$ have been scaled to represent values for local solar noon. Scaling factors for NO, $J(O^1D)$, and $J(NO_2)$ are derived from all GV box model runs for observations that occurred within 1 hour of local solar noon and are calculated as $[NO]_{inst}$ / $[NO]_{24\text{-}hr}$, $[J(O^1D)]_{inst}$ / $[J(O^1D)]_{24\text{-}hr}$, and $[J(NO_2)]_{inst}$ / $[J(NO_2)]_{24\text{-}hr}$, respectively. All scaling factors are averaged within 100 hPa pressure bins and applied to the likewise pressure-binned POLMIP multi-model mean for input to the box model. Because calculation of these factors relies on the availability of observations that occurred close to noon, we only obtain values from 1000 to 200 hPa. **Figures 2-17 – 2-19**, respectively, show the NO, $J(O^1D)$, and $J(NO_2)$ scaling factors calculated by the box

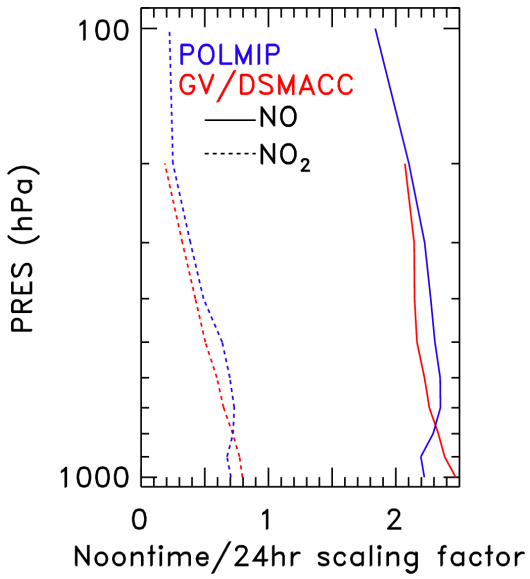

Figure 2-17. The scaling factors for NO and NO_2 used to convert monthly mean POLMIP mixing ratios of NO and NO_2 to mixing ratios representative of noon-time conditions, calculated from DSMACC box model results (red) and hourly POLMIP output (blue). The scaling factors calculated by the box model are applied in Figure 10c such that POLMIP values of NO_x can be directly compared with the daytime NO_x values, from NO observed during CONTRAST and NO_2 calculated by the box model; the NO scaling factor is also used in the POLMIP box modeling analysis, where POLMIP values of NO are input to the DSMACC box model initialized at local solar noon. Scaling factors are calculated for 100 hPa bins using the DSMACC box model, which simulates diurnally varying NO and NO_2. Scaling factors are calculated for NO and NO_2 as (NO_{INST}) / ($NO_{24\ HR}$) and ($NO_{2\ INST}$) / ($NO_{2\ 24\ HR}$), respectively, for all CONTRAST GV observations that meet the latitude/longitude filter discussed in the methods section and occurred within 1 hour of Guam local solar noon (2:00 UTC). The scaling factors calculated from POLMIP hourly output are derived from the 3 CTMs (CAM-Chem, GMI, and LMDZ) that provided hourly output for the TWP region for April (neither January nor February hourly output was available) and are calculated as (NO_{INST}) / ($NO_{24\ HR}$) and ($NO_{2\ INST}$) / ($NO_{2\ 24\ HR}$), where NO_{INST} and $NO_{2\ INST}$ are the hourly means for 1:00, 2:00, and 3:00 UTC (local solar noon at Guam ±1 hour).

model as well as scaling factors calculated from hourly output of the POLMIP CTMs, noted in the caption, that provided fields of each species. The comparison adds confidence to our method of scaling monthly mean concentrations to instantaneous noontime values.

The scaling factor for HCHO is calculated from the same output of the UWCM model used to generate 24-hour average values of HCHO shown in Figures 2-15d and 2-15i. The same method is used to calculate the scaling factor, solved as

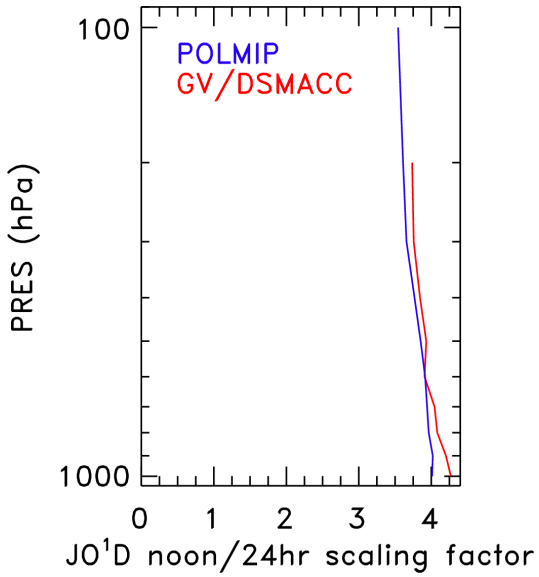

Figure 2-18. The scaling factors for J(O^1D) used to convert monthly mean POLMIP values of J(O^1D) to values representative of noon-time conditions, calculated from DSMACC box model results (red) and hourly POLMIP output (blue). The method for calculating these scaling factors follows the same method used for NO and NO_2 in Figure 2-17, except that the POLMIP value was calculated from hourly output only from POLMIP output of the CAM-Chem model due to lack of availability of J values from the other POLMIP models.

$[HCHO]_{inst}$ / $[HCHO]_{24\text{-}hr}$, but for any measurement that occurred within 2 hours of noon instead of 1, due to the coarser time resolution of the UWCM box model run. The HCHO scaling factor is shown in **Figure 2-20**.

The difference between the OH resulting from individual variable swaps and OH calculated from a base run of the box model, constrained only to GV observations, is shown for each species in **Figure 2-21a**. Particularly for pressures greater than ~400 hPa, NO_x is dominant in driving large negative differences in $[OH_{24\ HR}]$ (negative indicating that the POLMIP OH precursor is responsible for a low OH bias in the CTMs). The highest values of NO_x in the mid-troposphere coincide with HOLW structures; **Figure 2-22c** shows NO_x values calculated from observed NO and modeled steady-state NO_2, separated by our categorization of HOLW and background conditions (Section 2.2.6). Figures 2-22a and 2-22b show

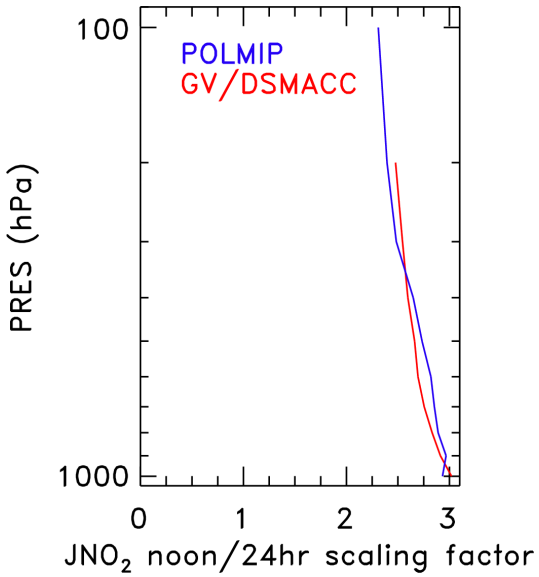

Figure 2-19. The scaling factors for J(NO_2) used to convert monthly mean POLMIP values of J(NO_2) to values representative of noon-time conditions, calculated from DSMACC box model results (red) and hourly POLMIP output (blue). The method for calculating these scaling factors follows the same method used for NO and NO_2 in Figure 2-17, except that the POLMIP value was calculated from hourly output only from POLMIP output of the CAM-Chem model due to lack of availability of J values from the other POLMIP models.

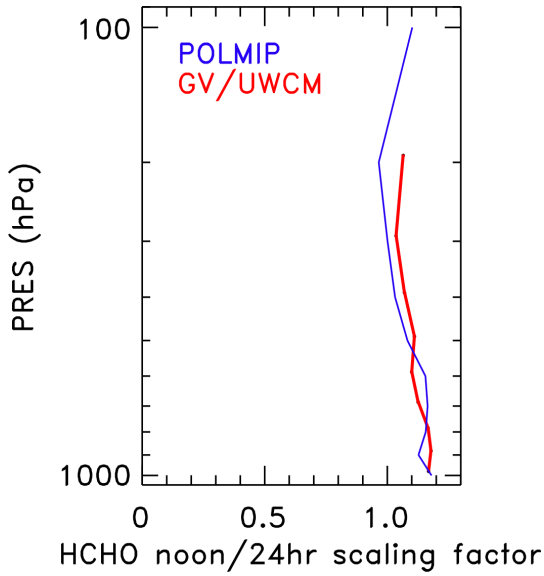

Figure 2-20. The scaling factor for HCHO used to convert monthly mean POLMIP values of HCHO to values representative of noon-time conditions, calculated from GV observations and calculations by the UWCM box model (red) and from hourly output from the POLMIP CTMs (blue). The GV/UWCM scaling factors are applied in Figures 2-21e and 2-21j such that the HCHO measurements made during CONTRAST can be compared directly to the POLMIP monthly mean values of HCHO. Scaling factors are calculated for 100 hPa bins using the UWCM box model, which simulates diurnally varying HCHO. Scaling factors are calculated as ($HCHO_{INST}$) / ($HCHO_{24\ HR}$) for all CONTRAST GV observations that meet the latitude/longitude/SZA filter discussed in the methods section and fall within 2 hours of local solar noon. The same calculation is performed to derive the POLMIP scaling factors using the hourly output from CAM-Chem, GMI, and LMDZ from April (January and February hourly output was unavailable).

the bimodal distributions of O_3 and H_2O, respectively, observed during CONTRAST. Previous work suggests the source of these HOLW structures is biomass burning emissions from Africa and Southeast Asia [*Anderson et al.*, 2016]. Therefore, the model underestimate of NO_x in the TWP is likely related to model treatment of nitrogen emissions, chemistry and/or transport from distant landmasses. As discussed in Section 2.3.2 in relation to the CAM-Chem underestimate of NO_x, there are several potential causes that may be driving low NO_x concentrations within global models.

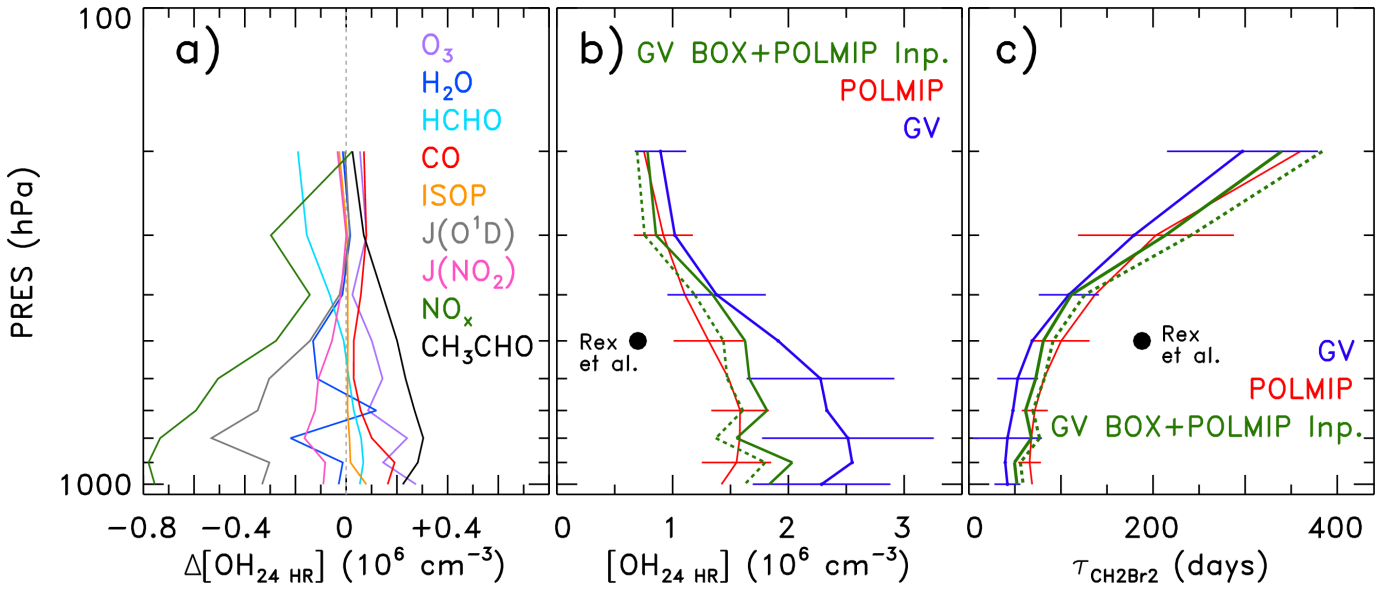

Figure 2-21. Panel a) shows the difference in $[OH_{24\,HR}]$ between a run of the DSMACC box model constrained to GV observations of all OH precursors with the exception of the indicated species and another run of the model constrained to GV observations of all OH precursors, where indicated species refers to the POLMIP multi-model mean value. These box model difference plots have been conducted at 100 hPa intervals. Panel b) shows the mean and standard deviation $[OH_{24\,HR}]$ profile calculated by the DSMACC box model constrained to GV observations of OH precursors (blue) compared to the multi-model mean and standard deviation of monthly mean [OH] in the POLMIP archive from 8 CTMs (red). The solid green line represents $[OH_{24\,HR}]^{CONTRAST}$ (blue) + $\Delta[OH_{24\,HR}]^{ALL}$, where $\Delta[OH_{24\,HR}]^{ALL}$ represents the difference between a run of the DSMACC box model constrained to POLMIP multi-model mean values of all 9 OH precursors and another run of the model constrained to GV observations of all 9 OH precursors. The profile of $\Delta[OH_{24\,HR}]^{ALL}$ is nearly identical to the sum of the 9 terms shown in panel a) (see Figure 2-24). Panel c) shows lifetime of CH_2Br_2 (τ_{CH2Br2}) with respect to loss by OH for $[OH_{24\,HR}]$ from the box model constrained to GV measurements (blue), for the multi-model monthly mean [OH] from the POLMIP CTMs (red), and for $[OH_{24\,HR}]$ from the box model constrained to the 9 OH precursors from POLMIP (solid green). The dashed green lines are adjusted to account for the 13% high bias in OH calculated by the box model, attributable to the box model chemical mechanism (from Figure 5d). The calculation of the dashed green lines is identical to the solid green lines except that values of $[OH_{24\,HR}]$ are multiplied by $^1/_{1.13}$, or 0.885. Values of $[OH_{24\,HR}]$ and τ_{CH2Br2} reported by *Rex et al.* [2014] at 500 hPa for October 2009 in the TWP are shown in panels b) and c).

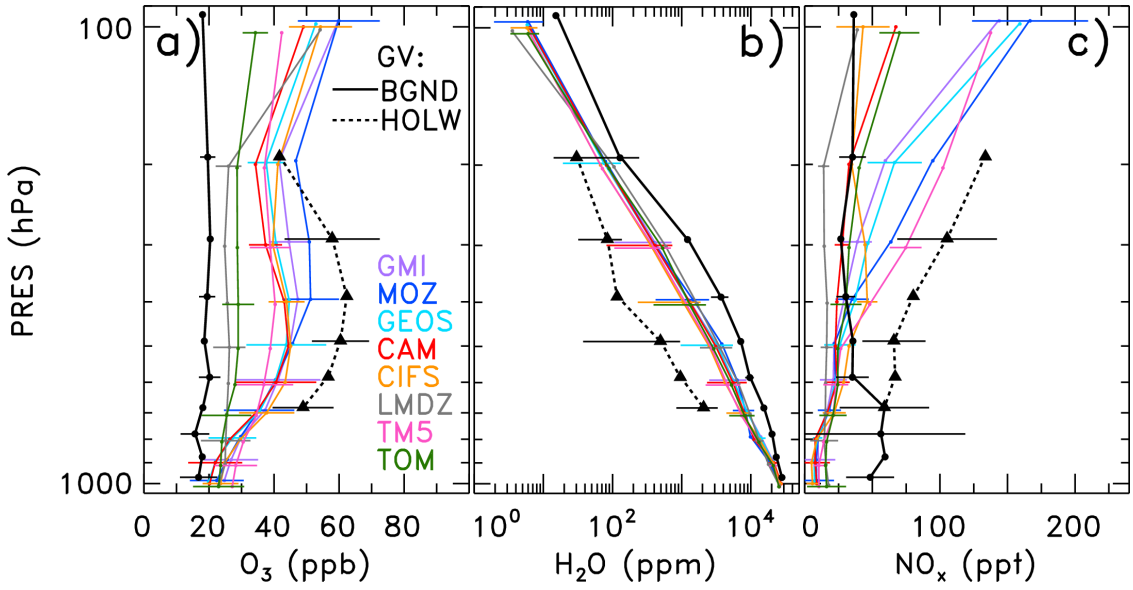

Figure 2-22. Profiles of monthly mean O_3 (panel a), H_2O (b), and NO_x (c) mixing ratio from the POLMIP archive for 8 CTMs (colored lines) for January and February 2008 compared to profiles of these 3 species measured by the GV during CONTRAST for background conditions (BGND) and well-defined high O_3, low H_2O (HOLW) structures. Criteria for BGND are simultaneous RH > 70%, O_3 < 25 ppb; criteria for HOLW are simultaneous RH < 20%, O_3 > 40 ppb. Relative humidity (RH) is calculated from observed H_2O and temperature (T), with respect to liquid water for T > 0°C and with respect to ice for T < 0°C. The GV profiles of NO_x are the sum of measured NO and box modeled NO_2 at the time of observation. Since we are showing GV profiles obtained only during daylight conditions, the POLMIP NO_x profile (archived as monthly mean) is calculated from NO and NO_2 scaled by the mean profile of ($[NO_{INST}]$ / $[NO_{24\,HR}]$) and ($[NO_{2\,INST}]$ / $[NO_{2\,24\,HR}]$) estimated from the box model simulations of the GV data. Error bars represent 1 standard deviation about the mean for 100 hPa pressure bins; they are offset slightly in the vertical for clarity. Some of the error bars are omitted to avoid clutter.

Other species investigated by constraint of the box model to POLMIP multi-model mean values include $J(O^1D)$ and $J(NO_2)$. Both account for lower OH values within the POLMIP CTMs, with $J(O^1D)$ driving the larger differences, but with $J(NO_2)$ also showing an influence OH at low altitudes. However, this finding results from the predominantly clear-sky sampling that occurred during CONTRAST, discussed in Section 2.3.2. Ozone and H_2O from the POLMIP models also drive large fluctuations in $[OH_{24\,HR}]$. The changes in $[OH_{24\,HR}]$ derived from POLMIP H_2O fluctuate and are generally centered about 0, while those due to POLMIP O_3 account

for a high bias in POLMIP OH. Indeed, we do see that the multi-model mean O_3 found for the POLMIP CTMs is higher than the mean O_3 vertical profile from CONTRAST observations (Figure 2-16f), though the individual CTMs are spread about the observations except at the lowest and highest pressures (Figure 2-16a). This could indicate a problem with reproducing the HOLW structures that were observed during CONTRAST; however, the monthly mean resolution of the model output does not allow us to explore this further.

The OH precursors HCHO and CH_3CHO also influence OH concentrations in a manner similar to that seen with CAM-Chem. Constraint to low values of HCHO from the POLMIP CTMs causes a decrease in OH at lower pressures (≤ ~200 hPa) where HCHO is an important source of HO_x [*Jaeglé et al.*, 1998], while constraint to low POLMIP values of CH_3CHO causes an increase in OH nearer the surface. As was the case with CAM-Chem, oceanic emissions of CH_3CHO are absent from the POLMIP CTMs, seen in comparisons of vertical profiles to values from CONTRAST observations in **Figure 2-23**, resulting in a large missing sink for OH in the models.

As seen with CAM-Chem, C_5H_8 drives near-zero [$OH_{24\ HR}$] differences throughout the troposphere. Isoprene in the mid- to upper troposphere, at pressures lower than ~800 hPa, is almost always below the detection limit of the TOGA instrument (1 ppt), so the small [$OH_{24\ HR}$] perturbation resulting from box model constraint to POLMIP C_5H_8 is uncertain but unlikely to be significant since these concentrations are so near 0.

The final variable from POLMIP used to constrain the DSMACC box model, CO, exhibits a small effect on [$OH_{24\ HR}$] despite large differences in the mean CO

values themselves. As with the CAM-Chem CTM, the POLMIP multi-model mean value of CO is significantly lower than the CONTRAST mean CO throughout most of the troposphere, by 10-15%. Many modeling studies have identified and sought to understand low biases in model CO [e.g., *Shindell et al.*, 2006; *Naik et al.*, 2013; *Monks et al.*, 2015; *Strode et al.*, 2015]; explanations for the bias range from underestimated CO from fossil fuel and biomass burning in emissions inventories [*Shindell et al.*, 2006] to overestimated OH (the main sink for CO) in the northern hemisphere [*Strode et al.*, 2015]. Whatever the cause, underestimation of the CO sink in the POLMIP CTMs leads to a small positive perturbation in [$OH_{24\ HR}$], much less in magnitude than the perturbations due to NO_x, $J(O^1D)$, and CH_3CHO. This finding suggests that OH concentrations in the remote TWP are controlled primarily by its sources except when a large sink is completely absent, as is the case with CH_3CHO.

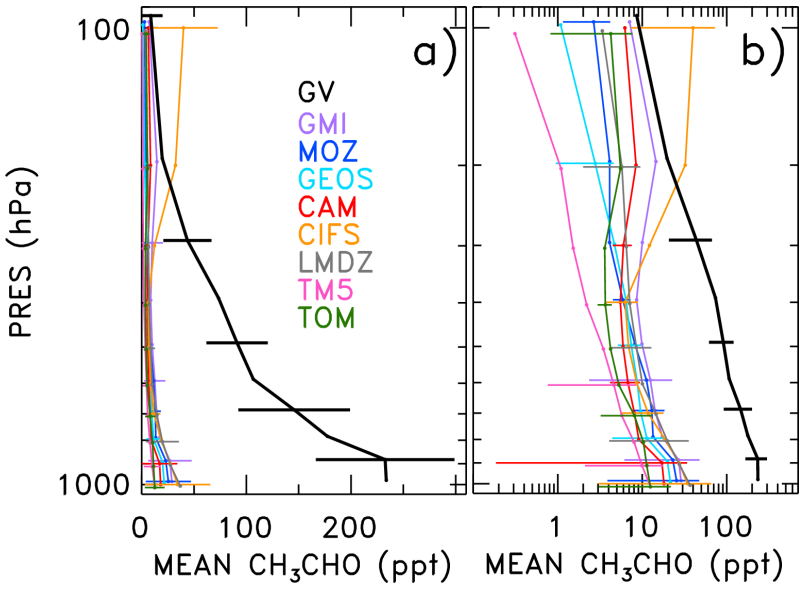

Figure 2-23. Same as Figure 2-12, except only showing mean CH_3CHO values from individual POLMIP CTMs (colors) and from CONTRAST campaign (black) using a linear scale (panel a) and a log scale (panel b).

One additional box model simulation is performed in which all 9 POLMIP OH precursors (O_3, H_2O, CO, C_5H_8, HCHO, CH_3CHO, NO_x, $J(O^1D)$, and $J(NO_2)$) are simultaneously used as constraints. The difference in $[OH_{24\,HR}]$ between a base run of the box model, constrained only to CONTRAST observations of the precursors, and this simulation is nearly identical to the sum of the $[OH_{24\,HR}]$ differences due to each species from Figure 2-21a (comparison of the two methods of finding total $\Delta[OH_{24\,HR}]$ is shown in **Figure 2-24**). The total $\Delta[OH_{24\,HR}]$ is added to the campaign-wide $[OH_{24\,HR}]$ vertical profile to determine whether these 9 factors describe the difference between GV and POLMIP OH. The result of this analysis (solid green line, Figure 2-21b) generally matches the OH from the POLMIP MMM (red line) in

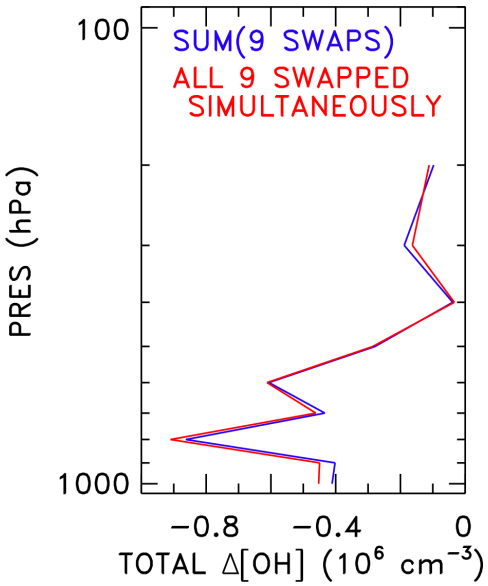

Figure 2-24. The total $\Delta[OH_{24\,HR}]$ from two sets of box model analyses of OH. The first is from 9 separate runs of the DSMACC box model constrained to GV observations of all OH precursors except for the substitution, individually, of monthly mean POLMIP values of O_3, H_2O, NO_x, $J(O^1D)$, CO, C_5H_8, HCHO, $J(NO_2)$, and CH_3CHO. A difference in $[OH_{24\,HR}]$ is calculated between each of these runs and a base run of the DSMACC box model constrained only to GV observations of all OH precursors. The sum of these 9 values of $\Delta[OH_{24\,HR}]$ are plotted (blue). The second box model analysis involves only one additional run of the DSMACC box model, where it is constrained to all 9 species listed above simultaneously. A $\Delta[OH_{24\,HR}]$ is calculated between this run and the base run of the DSMACC box model constrained only to GV observations of OH precursors (red). Box model runs were conducted, and total $\Delta[OH_{24\,HR}]$ values calculated, at 100 hPa intervals.

the upper troposphere, though values in the low to mid-troposphere overestimate those from POLMIP. Subsequently, τ_{CH2Br2} derived from these derived [$OH_{24\ HR}$] values shows that switching to box model constraint of the 9 POLMIP OH precursors matches the POLMIP τ_{CH2Br2} values in the upper troposphere (solid green line, Figure 2-21c) but underestimate τ_{CH2Br2} in the lower and mid-troposphere. However, recall from Section 2.3.3 that the box model chemical mechanism could contribute a bias in calculated OH as high as 13%. If adjusted to account for this bias, our simulations agree well with values of [$OH_{24\ HR}$] and τ_{CH2Br2} from the POLMIP MMM (dashed green lines, Figures 2-21b and 2-21c). We infer from this result that the offset in OH driven by the box model chemical mechanism is consistent when compared both to CAM-Chem and to the POLMIP suite of CTMs.

We also conduct quantitative analysis of the OH vertical profiles modeled by the POLMIP swap simulations by calculating tropospheric column OH values as was done with the CAM-Chem simulations. Values of tropospheric OH column for each simulation are shown in **Table 2-2**. The analysis confirms that NO_x values from POLMIP drive a large 22% underestimation of OH (determined by taking the inverse of the ratio in Table 2-2). POLMIP fields of $J(O^1D)$ result in a 10% decrease in OH relative to the observationally-constrained GV OH; however, this supports the notion that primarily clear-sky sampling during CONTRAST leads to an inherent sampling bias. The only other POLMIP precursor to influence OH by a factor ≥10% is CH_3CHO, which results in a 10% overestimate of column OH by the models.

Additionally, we use the POLMIP archive to determine the extent to which seasonal differences in OH precursors could explain the difference between the mean

Table 2-2. Tropospheric OH Columns Calculated for the CONTRAST Mean OH Vertical Profile and POLMIP Model Simulations

POLMIP Box Model Run	OH Column[a] (10^{12} cm^{-2})	Ratio (GV / Run X)
GV	2.17	---
C-C (POLMIP)	1.56	1.39
POLMIP MMM	1.54	1.41
GV, POL NO_x	1.70	1.28
GV, POL J(O^1D)	1.96	1.11
GV, POL CH_3CHO	2.38	0.91
GV, POL O_3	2.30	0.94
GV, POL CO	2.26	0.96
GV, POL J(NO_2)	2.09	1.04
GV, POL HCHO	2.11	1.03
GV, POL H_2O	2.12	1.02
GV, POL C_5H_8	2.17	1.00

[a]Columns are integrated from the surface to 200 hPa

$OH_{24\,HR}$ value that we calculate for the CONTRAST campaign for January–February 2014 and the TWP $OH_{24\,HR}$ value simulated by GEOS-Chem in *Rex et al.* [2014] for October 2009, both at 500 hPa (**Figure 2-25**). At this pressure level, for the corresponding months, no POLMIP model simulates mean TWP OH as high as our estimate; nor does any model simulate a mean OH as low as the *Rex et al.* [2014] estimate. Both the box model-based estimate of OH and the *Rex et al.* [2014] CTM-based estimate of OH are grounded in observations of O_3 (along with other chemical species and radiative variables, for our estimate). The O_3 sondes used during the TransBrom cruise in *Rex et al.* [2014] reveal O_3 concentrations often below the limit of detection (~15 ppb); the range of these measurements are indicated by the shaded region in Figure 2-25b. Again, POLMIP CTMs do not reproduce values of O_3 as low as those reported by *Rex et al.* [2014], though our mean O_3 from CONTRAST

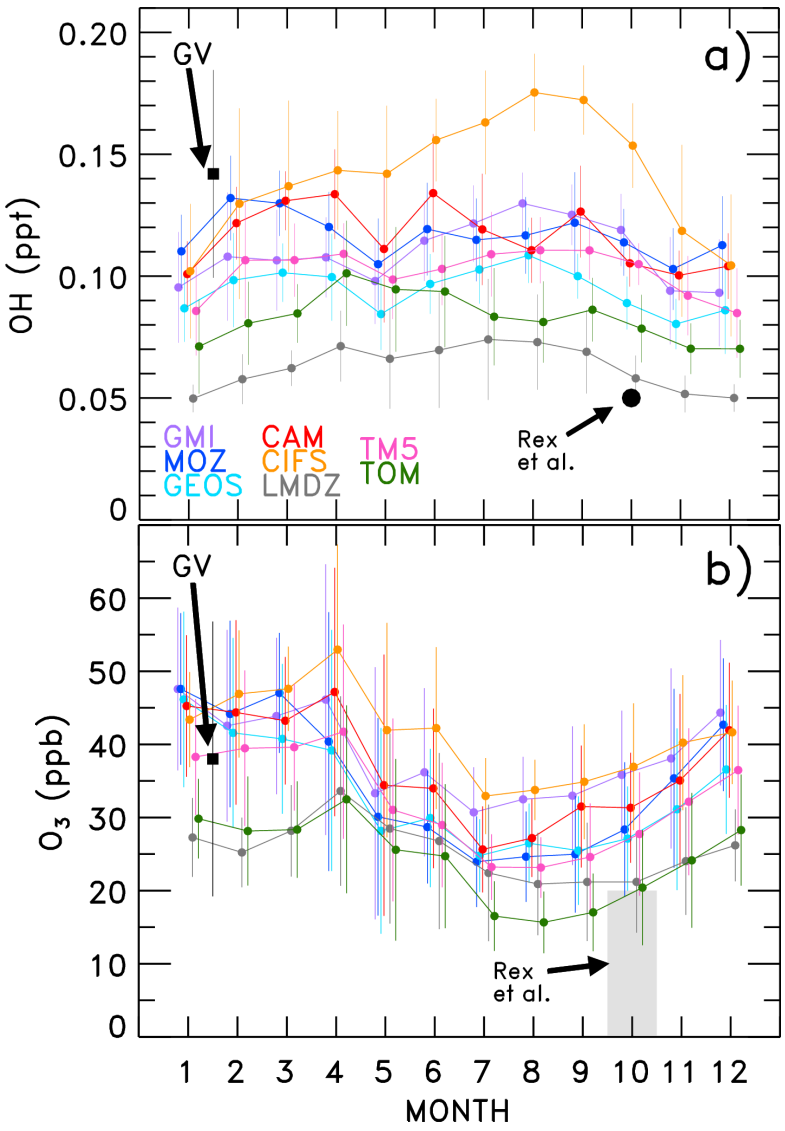

Figure 2-25. Seasonal variation of monthly mean OH mixing ratio (panel a) and O_3 mixing ratio (b) from the 8 POLMIP CTMs, for the pressure level closest to 500 hPa. The black squares show the mean and standard deviation of OH inferred from the CONTRAST GV observations of OH precursors (a) and O_3 (b), both at 500±50 hPa. The black circle shows OH (a) at 500 hPa for October 2009 from *Rex et al.* [2014]. The grey box in panel b) shows the range of O_3 reported by *Rex et al.* [2014] in the TWP at 500 hPa for October 2009.

observations lies in the middle of O_3 values from the POLMIP CTMs for January and February.

The exact role of interannual variations in explaining the large discrepancy between GV and *Rex et al.* [2014] OH is unknown due to the lack of observations in the region. Biomass burning differences between the *Rex et al.* [2014] study period

and that of CONTRAST are large (Figure 2-2, panels (a) and (c)); however, this is a result of seasonal variation and is expected. It is not within the scope of this study to quantitatively account for the impact of seasonal differences on OH in the TWP. Differences in the ENSO conditions between the two years should also be considered. The Multivariate ENSO Index for CONTRAST during January/February 2014 was neutral, whereas the *Rex et al.* [2014] study took place during a stronger El Niño event at the end of 2009 [*Wolter and Timlin*, 1993; 1998]. The expected ENSO-induced changes in O_3 are counter to what we would expect from our observations. Suppressed convection in the TWP during an El Niño event would enable O_3 concentrations to build to higher concentrations [*Ziemke et al.*, 2010]; however, *Rex et al.* [2014] observed much lower O_3 during this time period than we observed during neutral ENSO conditions. So while large-scale effects were undoubtedly in play between the two observation periods, the interannual effects most commonly examined do not easily explain the differences in observed O_3 and calculated OH between *Rex et al.* [2014] and this study.

2.4 Conclusions

Box model calculations of OH concentration were performed for the CONTRAST campaign that occurred in the TWP during January–February 2014. The box model was constrained to measurements of O_3, CO, NO, HCHO, H_2O, C_3H_8, CH_4, C_5H_8, CH_3COCH_3, CH_3OH, CH_3CHO, $J(O^1D)$, and $J(NO_2)$. Comparisons and additional box model simulations were conducted to understand the differences between the measurement-inferred GV OH and OH from two sets of global CTM

simulations. We find a tendency for OH in the TWP in global models to be biased low relative to our observationally constrained calculation of OH, with the primary driver being CTM underestimation of NO_x. The influence of this NO_x bias has the greatest impact on OH throughout the troposphere. Additional drivers of OH differences include CH_3CHO, which is underestimated in global models resulting in a high bias in OH near the surface, and HCHO which is also underestimated in global models; however, in this case the underestimate results in a low bias in OH in the upper troposphere.

Lifetimes of CH_2Br_2 calculated from the observationally constrained OH are significantly lower than found in a previous study of TWP OH [*Rex et al*., 2014], though the latter was found for a different season (October versus January/February for the CONTRAST campaign). Overall, we do not find evidence for a local minimum in OH concentrations in this region. Mean values of $[OH_{24\ HR}]$ remain above 2×10^6 cm^{-3} (or mixing ratio of ~0.1 ppt) within the lower troposphere. We attribute this to relatively elevated NO_x concentrations (for the remote TWP), sustaining OH through recycling of HO_2. Additionally, O_3 measurements reached a minimum of ~20 ppb, suggesting that past O_3 values reported as being significantly lower may have been hindered by limit of detection issues. The air parcels in which we estimate the lowest OH abundances are those with high O_3, low H_2O characteristics. Thus, we conclude that OH production is more likely limited by availability of H_2O than either O_3 or NO_x for the conditions we sampled.

While we believe that this new observationally constrained estimate of OH will help global models that run active chemistry (CTMs as well as CCMs) to

constrain their simulations of OH, it should be noted that our finding contradicts the current view of global model oxidative capacity. The majority of global models calculate values of τ_{CH4} significantly lower than the current best empirical estimate of τ_{CH4}. Our results are representative of a small region of the globe, and, while they are positioned within the crucial tropical band, they are likely not representative of global model biases in OH. Instead, we hope that the implications of our findings (low biases in NO_x possibly indicating shortfalls in NO_x transport from biomass burning regions, low biases in HCHO in the upper troposphere of the TWP, insight into the importance of CH_3CHO emissions from oceans) may spur improvements to the models that in turn may aid our understanding of the global atmosphere. Before we can truly rely on models to understand how climate change will shape the future atmosphere, it is crucial that we first demonstrate the ability to model the chemistry and global burdens of OH accurately.

Chapter 3: Quantifying the Causes of Differences in Tropospheric OH within Global Models

3.1 Introduction

Hydroxyl radical (OH) is the primary daytime oxidant in the troposphere [*Levy*, 1971] and is responsible for the breakdown of many pollutants and other atmospheric species of interest. Notably, the abundance and lifetime of methane (CH_4) are controlled by the global tropospheric OH concentrations ($[OH]^{TROP}$). The chemistry of OH, however, is not easily modeled due to its numerous sources and sinks, rapid recycling in the presence of NO_x (=NO+NO_2), and non-linear chemical feedbacks that are not fully understood [*Prather, et al.*, 2001; *Taraborrelli et al.*, 2012].

The inherent difficulty in modeling $[OH]^{TROP}$ and CH_4 lifetime (τ_{CH4}) on a global scale is evidenced by large τ_{CH4} differences encountered during model intercomparison projects [*Shindell et al.*, 2006; *Fiore et al.*, 2009; *Naik et al.*, 2013]. Here as elsewhere in this dissertation, τ_{CH4} refers to loss of CH_4 with respect to reaction with tropospheric OH, unless otherwise noted. The 3 model intercomparison studies included in **Table 3-1**, not considering this study, show model spreads in τ_{CH4} ranging from 62% [*Fiore et al.*, 2009] to 84% [*Shindell et al.*, 2006]. These spreads are the difference between maximum and minimum values of τ_{CH4} divided by the multi-model mean. The spread in τ_{CH4} values found in this study is only 38%; however, we analyze fewer models and do not have the extreme outliers of τ_{CH4} found

Table 3-1. Estimates of CH_4 lifetime due to removal by OH from recent literature and this study

Method	τ_{CH4} due to OH	Source
Best estimate from CH_3CCl_3 inversion; range from OxComp CTM evaluation	9.6 (6.5-13.8)[a]	IPCC TAR, 2001
CH_3CCl_3 inversion	11.2 (9.9-12.5)[b]	IPCC AR5, 2013
CH_3CCl_3 inversion	10.2 (9.5-11.1)[b]	*Prinn et al*., 2005
CH_3CCl_3 inversion	11.2 (9.9-12.5)[b]	*Prather et al*., 2012
CCM model intercomparison, ACCMIP (16 models)	9.7 (7.1-14.0)[a] (8.2-11.2)[b]	*Naik et al*., 2013 and *Voulgarakis et al.*, 2013
CTM model intercomparison (12 models)	10.19 (6.19-12.50)[a] (8.47-11.91)[b]	*Fiore et al.*, 2009
CTM model intercomparison (26 models)	9.72 (6.91-15.05)[a] (8.02-11.42)[b]	*Shindell et al.*, 2006
12-box model inversion	10.5 (9.3-12.8)[b]	SPARC Lifetimes Report, 2013
CTM model intercomparison (8 models)	8.1 (6.7-9.8)[a] (7.2-9.0)[b]	POLMIP/This study, 2015

[a]Full range of values provided.
[b]1σ uncertainty provided

in the other studies (τ_{CH4} as low as 6.2 years in *Fiore et al.* [2009] and as high as 15 years in *Shindell et al.* [2006]).

The cause of model differences in τ_{CH4} for the contemporary atmosphere is particularly important to address because CH_4 is the second most important greenhouse gas. The lifetime of CH_4 factors directly into the calculation of the global warming potential of this compound [Table TS.2, IPCC, 2013]. Furthermore, models disagree on how τ_{CH4} will evolve over the next century, due to variations in

atmospheric composition. *Voulgarakis et al.* [2013] found that the greenhouse gas emissions scenario that produces the highest level of agreement between 14 models still results in a multi-model mean percent change in τ_{CH4} of +8.5±10.4% between year 2000 and 2100. Of the 14 models analyzed, 3 gave negative changes, for year 2100 relative to year 2000, in τ_{CH4}, while another 3 gave changes in τ_{CH4} that exceed 25%. This level of disagreement raises concerns, and the path to fixing it lies in first accurately constraining present-day $[OH]^{TROP}$ and τ_{CH4} within the models.

Another challenge to our understanding of $[OH]^{TROP}$ is the persistent discrepancy between τ_{CH4} values calculated by models and those based on observations. Measurements of the temporal evolution of the global mean abundance of methyl chloroform (MCF: CH_3CCl_3) as well as the global emission rate of MCF are frequently used to infer the abundance of $[OH]^{TROP}$ and hence τ_{CH4}. *Prinn et al.* [2005] estimated a mean chemical τ_{CH4} of $10.2^{+0.9}_{-0.7}$ years for the 1978−2004 period following this method. *Prather et al.* [2012] adopted a more sophisticated approach, considering more terms for loss of MCF than prior studies, and estimated τ_{CH4} to be 11.2±1.3 years for year 2010. IPCC [2013] (see Section 8.SM.2) uses this *Prather et al.* [2012] value of τ_{CH4} for the latest sets of GWP calculations due to CH_4. For comparison, the multi-model mean values for present-day τ_{CH4} calculated in the analyses conducted by *Shindell et al.* [2006], *Fiore et al.* [2009], and *Naik et al.* [2013] are 9.72, 10.19, and 9.7 years, respectively. Given that CH_4 is such a potent greenhouse gas and that the sign of future changes in τ_{CH4} is uncertain [*Voulgarakis et al.*, 2013], the low bias in modeled τ_{CH4} relative to the recent empirical estimate provided by *Prather et al.* [2012] is crucial to understand. There have been two

recent attempts to assess our understanding of tropospheric OH based on observations. *Strode et al.* [2015] used satellite observations of CO to analyze the hemispheric biases in modeled OH. They found that both increasing Northern Hemisphere emissions of CO and reducing Northern Hemisphere OH bring the interhemispheric ratio of CO into better agreement with observations. However, the increase in CO emissions that is required results in overestimates of CO in source regions, relative to the satellite measurements. Further attribution simulations are unable to explain the high bias in Northern Hemisphere OH by adjusting for known model biases in O_3 and H_2O. *Nicely et al.* [2016b] (Chapter 2 of this dissertation), on the other hand, found that OH inferred from observations of precursors in the tropical western Pacific tended to exceed concentrations of OH calculated by global models.

The non-linear chemical response of OH to changes in sources and sinks, and the co-dependencies between many drivers of OH, present a challenge to modeling $[OH]^{TROP}$ on a global scale [*Spivakovsky et al.*, 1990; *Duncan et al.*, 2000]. A thorough investigation of multi-model differences in τ_{CH4} would require methodical examination of the complete chemical mechanisms of each participating model, which is an unreasonable expectation. In this study, we utilized the computational power of neural networks (NNs) [*Jain et al.*, 1996; *Gardner and Dorling*, 1998; *Heaton*, 2011; *Allison*, 2015] to mimic the behavior of the chemical mechanism of each chemical transport model (CTM) and reproduce its global OH output. The parallel computation method employed by NNs allows for the fitting of non-linear systems using codependent variables as inputs. We used NNs with the results from the POLARCAT Model Intercomparison Project (POLMIP) [*Emmons et al.*, 2015] to

quantify the effect of the input parameters in driving differences in $[OH]^{TROP}$ and τ_{CH4}.

3.2 Method

3.2.1 POLMIP CTMs

The POLMIP intercomparison project [*Emmons et al.*, 2015] was designed to take advantage of the Polar Study using Aircraft, Remote Sensing, Surface Measurements and Models, of Climate, Chemistry, Aerosols, and Transport (POLARCAT) [*Law et al.*, 2014] suite of observations taken in 2008. While the POLARCAT measurements focus on study of the Arctic troposphere, POLMIP includes model simulations with global coverage. Simulations were performed with a common emissions inventory for January to December, 2008 with output provided as monthly means for each month (see *Emmons et al.* [2015] for further detail). Participating models were run as CTMs, meaning they used winds and temperatures based on analyzed meteorological fields. As such, there is general consistency in the meteorological variables among the models. Each model provided monthly mean output for many chemical, physical, and radiative variables using standard chemistry and deposition schemes of each group. Only those models that output fields with global coverage are included in this study. Since this analysis relies on relative differences among models, output from only one (Version 4) of two available versions of CAM-Chem is considered, to eliminate a small bias due to use of output from two highly similar models.

The 8 models participating in this analysis exhibit some notable differences. Treatment of aerosols, the tropospheric chemistry scheme implemented, inclusion of stratospheric chemistry, and parameterization of lightning NO_x ($NO+NO_2$) vary among the 8 models (see *Emmons et al.* [2015] for further detail). CAM-Chem, GEOS-Chem, GMI-GEOS5, and MOZART4 use GEOS5 meteorology, while TM5 and C-IFS use ECMWF, and TOMCAT and LMDZ use ERA-interim meteorology. Latitude × longitude grids and number of vertical levels for each model are as follows: GMI-GEOS5: 2.0° × 2.5° with 72 vertical levels; MOZART4: 1.875° × 2.5° with 56 vertical levels; GEOS-Chem: 2.0° × 2.5° with 47 vertical levels; CAM-Chem: 1.875° × 2.5° with 56 vertical levels; C-IFS: 1.125° × 1.125° with 60 vertical levels; TM5: 2.0° × 3.0° with 60 vertical levels; TOMCAT: 2.81° × 2.81° with 31 vertical levels; LMDZ: 1.875° × 3.75° with 39 vertical levels. However, because of the fine spatial resolution of the C-IFS model output, the computer used for the NN analysis did not have enough RAM to train a NN using the raw archived output. Therefore, output from C-IFS was bilinearly interpolated to a 2.0° × 2.5° latitude/longitude grid for training of the NN.

Given that emissions of chemical species and atmospheric transport fields should be relatively consistent between various CTM simulations, differences in τ_{CH4} likely arise from variations in OH precursor and sink fields as well as the chemical mechanism inherent to each model. Here, we use NNs to quantify the drivers of inter-model differences in τ_{CH4} by swapping OH precursor fields from one model into the NNs of other models.

For our analysis of CTM output, values of τ_{CH4} were calculated using a mass weighting:

$$\tau_{CH4} = \frac{\sum M_{air} \times [CH_4]}{\sum [OH] \times k_{OH+CH4} \times M_{air} \times [CH_4]} \quad (1)$$

where M_{air} is the mass of air within a grid-box, "[]" denotes number density, k_{OH+CH4} is the rate constant for the OH+CH_4 reaction, and summations are performed over all tropospheric model grid-boxes [*Lawrence et al.*, 2001]. Mass weighting accounts for the latitudinal and altitudinal dependence of grid-box volume. Tropopause pressures were calculated for each model by using vertical profiles of O_3 and CO mixing ratios to identify a chemical tropopause following the method of *Pan et al.* [2004]. **Figure 3-1** shows the τ_{CH4} evaluated using Eq. 1 for each month, for the 8 CTMs that

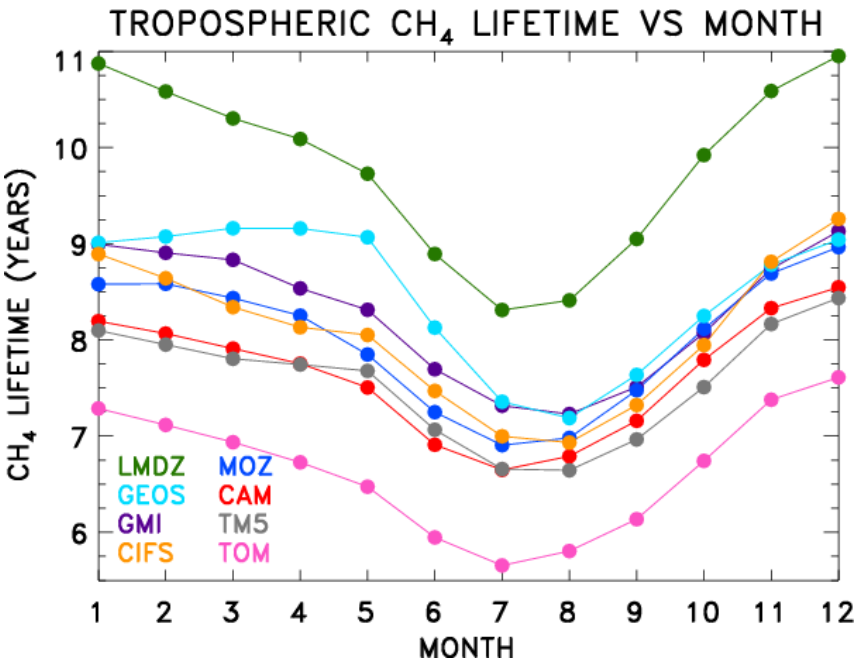

Figure 3-1. CH_4 lifetime by month calculated for each POLMIP CTM included in this analysis. CAM indicates CAM-Chem version 4. Values of τ_{CH4} are calculated with an air mass weighting from monthly mean output. Labels are listed in descending order of January lifetime values.

participated in POLMIP. The LMDZ-INCA model generally exhibits the longest τ_{CH4} (i.e. lowest values of tropospheric OH), with an annual mean τ_{CH4} of 9.8 years. The TOMCAT model has the shortest τ_{CH4}, with an annual average of 6.7 years.

The annual average values of τ_{CH4} from the 8 CTMs are listed in **Table 3-2**. The inter-model spread of τ_{CH4} for these 8 CTM simulations is 38%, found by taking the difference between the maximum and minimum values, and dividing by the multi-model mean. As noted above, this spread is smaller than reported in other comparisons, likely because these other studies involve a larger number of CTMs. Given the nature of our study, we are only able to use output from CTMs that archive global, monthly fields of a large number of chemical constituents. Most importantly, we note that all 8 values of τ_{CH4} given in Table 2 are shorter than the value of 11.2 years used by IPCC (2013) for the computation of the GWP of CH_4.

Table 3-2. Annual average CH_4 lifetime due to loss by OH evaluated for the 8 CTMs included in this study

POLMIP CTM	Annual Average τ_{CH4} (years)
CAM-Chem	7.6
C-IFS	8.1
GEOS-Chem	8.5
GMI-GEOS5	8.3
LMDZ-INCA	9.8
MOZART	8.0
TM5	7.6
TOMCAT	6.7

3.2.2 Neural Network Training

Neural networks were developed individually for each CTM, one per individual month (i.e., January, April, July, and October) that span the four seasons. The NN was trained to reproduce the 3-D monthly mean field of OH mixing ratio from the CTM; thus, inputs were chosen based on their direct influence on OH chemistry. Here we used monthly mean averages of 11 variables: volume mixing ratios of H_2O, O_3, NO_x, CO, CH_4, and isoprene, along with photolysis frequencies $J(O_3 \rightarrow O(^1D))$ and $J(NO_2)$ (units of s^{-1}) and physical parameters latitude, pressure (units of hPa), and temperature (units of K). Because CH_4 is set as a boundary condition in most global models, and little overlap exists between ranges of CH_4 values for some of the models, we have scaled the volume mixing ratio of CH_4 to a value between 0 and 1, with 1 representing the maximum tropospheric value present in a given model for that particular month.

Neural networks can be configured with many different architectures and degrees of processing power [*Gardner and Dorling*, 1998]. Here we used feed-forward NNs consisting of two hidden layers, depicted in **Figure 3-2**. The NNs for most of the CTMs contain 15 nodes per layer. However, we extended the NNs for TOMCAT, C-IFS, and GEOS-Chem to contain 30 nodes per layer, so that the OH fields from these CTMs could be reproduced by the NN with an accuracy comparable to that found using the NNs from the other CTMs. The Levenberg-Marquardt algorithm [*Heaton*, 2011] was used to adjust NN weights during training, based on the second derivatives of the errors of the simulated OH mixing ratios. Of all the tropospheric grid-points output for a single model month, 80% of those were used to

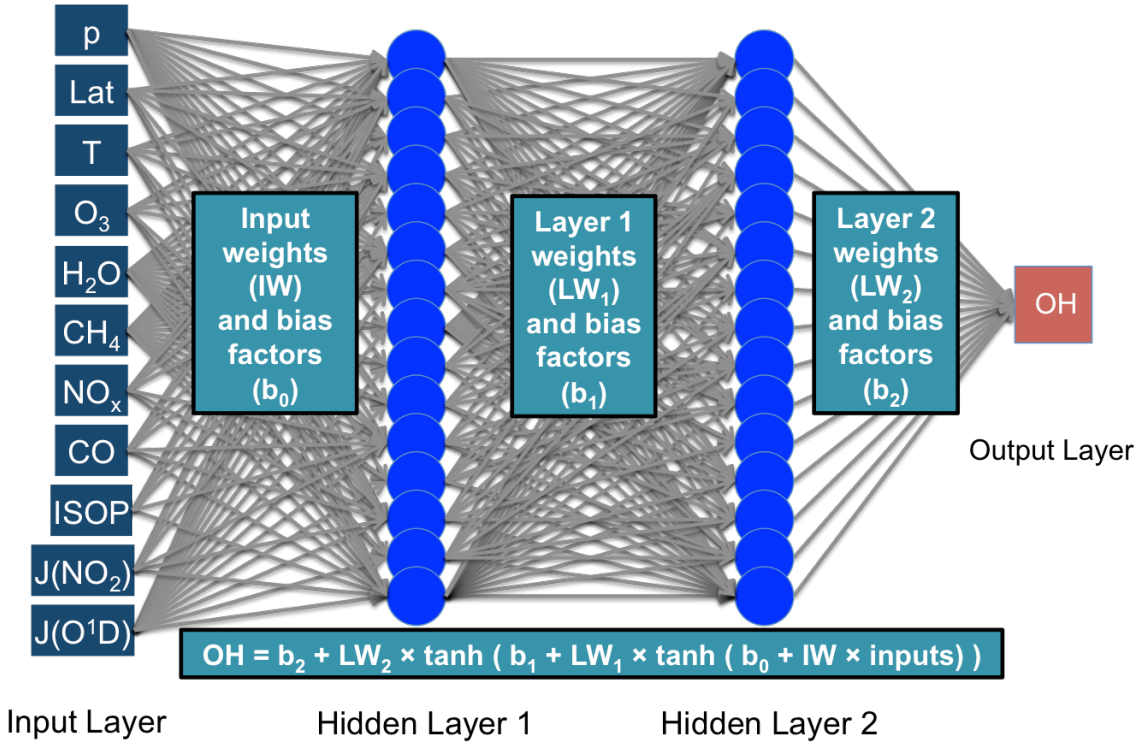

Figure 3-2. Architecture of the NNs used in the present study for all CTMs except GEOS-Chem, C-IFS, and TOMCAT. The NN consists of 2 hidden layers, each containing 15 nodes (represented by blue circles). The NNs for GEOS-Chem, C-IFS, and TOMCAT contain 30 nodes per hidden layer instead of 15. The 11 input parameters are listed on the left. Values are input as unitless mixing ratios for all chemical species except CH_4, units of s^{-1} for photolysis frequencies $J(O^1D)$ and $J(NO_2)$, K for temperature, and hPa for temperature. For CH_4, values are scaled relative to the maximum CH_4 within the troposphere for a given model such that the input value represents a ratio between 0 and 1. Hyperbolic tangent activation functions are performed on the linear combination of the inputs multiplied by their input weights (represented by grey arrows) at each node in Hidden Layer 1; those values are fed forward with additional weightings (Layer 1 weights) to the Hidden Layer 2, at which a second series of activation functions are performed. Output from Hidden Layer 2 is weighted once more (Layer 2 weights) and linearly combined to give a single OH mixing ratio for a given latitude, longitude, and pressure level.

train the NN, 10% were used to validate the NN and 10% were used as an independent test. Validation was performed by evaluation of the mean squared error (MSE); in the event that the MSE increased 6 iterations in a row, training was stopped, and the NN weights prior to the error increase were saved. In other words, the NN weightings that minimize a cost function and cannot be adjusted to decrease errors further are saved. The training process is repeated several times to identify the

NN weights that lead to the best agreement between simulated OH and CTM OH values. The training method used here is similar to methods found in *Lary et al.* [2009] and *Allison* [2015].

Upon successful training of NNs for each CTM, the performance of the NN was evaluated by calculating tropospheric OH mass columns, τ_{CH4}, and $[OH]^{TROP}$ for the NN-simulated fields of OH and comparing these NN-derived quantities to the values derived from the CTM output. Tropospheric mass columns were calculated by first summing the mass of OH within each grid box from the surface to the tropopause above a given point. These values were then interpolated to a common latitude/longitude grid (2.81° × 3.0°) and normalized by the base area of the surface grid box, such that reported units are g km^{-2}. We use column mass of OH (i.e., units of g km^{-2}) rather than column number density of OH (units of cm^{-2}) , because the former is better correlated with values of τ_{CH4} from the various CTMs. This better correlation is due to the dependence of τ_{CH4} on tropospheric mass (Equation 3-1) and the fact the mass of the troposphere differs among the various CTMs. Quantitative results of NN training are shown in Section 3.3.3.

3.2.3 Quantifying Precursor Effects on OH

Once established, NNs for each CTM were then used to quantify the effect on $[OH]^{TROP}$ of replacing one of the OH precursors fields (e.g., the distribution of O_3) with that from another CTM. This was done by running the NN with inputs from the parent CTM, except for a single input field taken from another CTM. This "swapped" input was interpolated to the native spatial grid of the parent CTM and run

through a series of checks to prevent a value outside of the range on which the NN was trained from being passed to the NN. The latter step prevents the NN from extrapolating outside of the "trained range" of an input variable, which we have found often results in anomalous values of OH being output. Our method of "extrapolation control" also ensures the substitution is acceptable for the current chemical regime. To test the effect of MOZART CO on the value of OH output by the GMI NN, each MOZART CO value is compared to ranges of CO mixing ratios acceptable for the values of GMI O_3, CH_4, isoprene, etc. that co-existed with this value of CO during training. In other words, if the MOZART CO value was indicative of pollution, while the other GMI variables indicate clean conditions, the substituted CO value will likely be too high for the NN in an otherwise clean chemical regime. In this case, the CO value would be revised down to the highest "acceptable" value over which the NN was trained. Our extrapolation control method is accomplished by compiling a series of reference matrices for each CTM and checking against the appropriate matrix whenever a variable substitution is conducted.

After running a NN with an input field substituted from another CTM, new values of tropospheric OH mass column and τ_{CH4} were calculated from the output OH mixing ratios. The change in both, relative to the parent NN base run, is attributed to the substituted variable. These swaps were performed for all chemical and radiative variables, as well as temperature, between all models.

3.3 Results

3.3.1 Neural Network Performance

The NNs reproduced OH mixing ratios from the CTMs, and resulting tropospheric OH mass columns, with good accuracy. **Figure 3-3** shows tropospheric column mass differences between the NN and the CTM. Generally the NNs perform well for most regions, with simulated column mass OH within ±5% of the CTM values. Additionally, the MSE metric by which the NNs were validated generally fell below 1.0×10^{-3}. The NNs for C-IFS and GEOS-Chem, however, exhibited errors higher than this threshold for at least one of the four months for which NNs were trained, despite use of a more powerful NN architecture. NN performance also displayed a seasonal dependence, with all producing highest MSE values in January and lowest MSE values in October or April. Finally, the most important quantity, τ_{CH4}, which reflects global tropospheric OH in each CTM, is reproduced quite well by the NNs. The largest error in τ_{CH4} shown in Figure 3-3, 0.5%, results from the NN for CIFS. This accuracy results from the tendency of overestimates of OH in some geographic regions to be balanced by underestimates in other regions.

The spatial distribution of the difference between NN and CTM tropospheric OH mass column indicates that NN errors are most concentrated either over continents or in oceanic regions downwind of strong biomass burning. This may be due to the influence of an emission source that leads to a unique set of chemical conditions for which the NN could not be sufficiently trained. In addition, monthly mean averages of the parameters used as input to the NN are not able to represent the non-linearity of the chemical conditions in the actual POLMIP CTM run that led to a

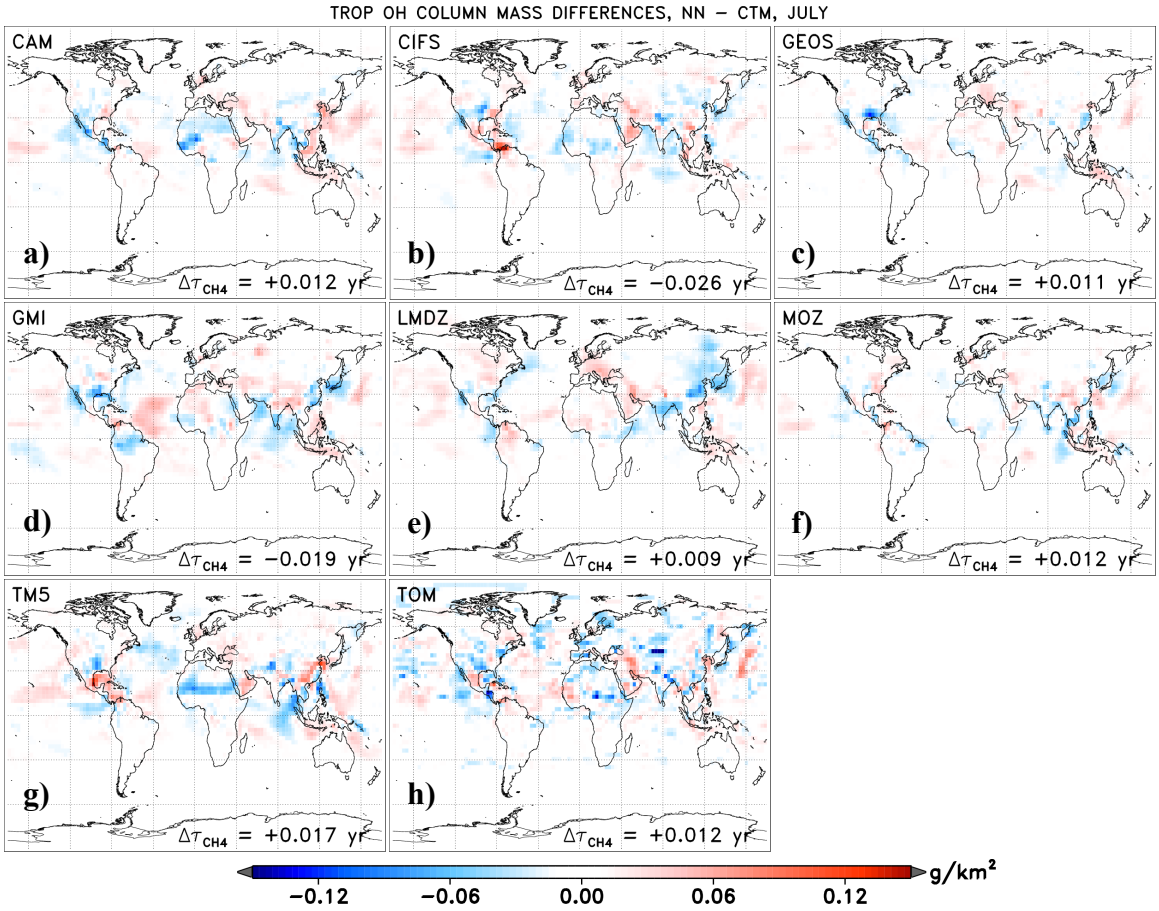

Figure 3-3. Tropospheric column mass OH absolute differences, NN – CTM, for CAM-Chem (panel a), C-IFS (b), GEOS-Chem (c), GMI-GEOS5 (d), LMDZ (e), MOZART4 (f), TM5 (g), and TOMCAT (h). Tropospheric columns are calculated with k_{OH+CH4}×[CH_4] weighting in order to highlight those differences that are most relevant in determining τ_{CH4}. Difference in τ_{CH4} between the NN and CTM is inscribed in the lower right corner of each plot.

particular monthly mean value of OH at a specific model grip point. Regardless of these localized errors, the NNs are able to reproduce τ_{CH4} values for their respective CTMs to within ±0.03 years and the worst performing NN, that for C-IFS, reproduces τ_{CH4} to within 0.026 years of the parent CTM. As such, the NN error in calculating τ_{CH4} is less than 0.5%. We speculate that NN performance could be improved if training would be based on daily output for each day of a particular month, but in this case the size of the archived files as well as the computational power needed for training would likely both exceed readily available resources at most research centers.

3.3.2 Results from Individual Precursor Analysis

Each input variable was "swapped" between all models for a given month, allowing the impact on OH to be examined for each of the primary parameters that affect OH. Comparisons of tropospheric OH mass differences due to CO, $J(O_3 \rightarrow O^1D)$, NO_x, $J(NO_2)$; CH_4, isoprene, H_2O, isoprene, and O_3 swaps between CAM-Chem and GEOS-Chem are shown in **Figures 3-4** and **3-5**. Color bars for the pair of plots on the left and right of each row are mirror images of each other, designed to represent the fact that decreases in OH in one model for a variable swap should be accompanied by an increases in OH when the swap occurs in the opposite direction. For example, widespread decreases in OH are found by the CAM-Chem NN as a result of using CO from GEOS-Chem, which is generally higher than CO from CAM-Chem (Figure 3-4a). When the swap of CO occurs in the other direction; i.e., use of CO from CAM-Chem in the GEOS-Chem NN, we expect OH to exhibit a widespread increase, since CO from CAM-Chem is generally lower than CO from GEOS-Chem (Figure 3-4b). Visual comparison of CO fields from the two models confirms that CO mixing ratios are perceptibly higher in GEOS-Chem (not shown). The visual similarity of the colors on the left hand plots to those on the right hand plots, for each row, confirms the NNs are behaving in a reasonable manner. Between the GEOS-Chem and CAM-Chem models, the largest differences in τ_{CH4} and OH are driven by differences in the fields of CO.

The effect of swapping NO_x between the CAM-Chem and GEOS-Chem within the respective NNs (Figure 3-4e and f) highlights large differences in OH over continental source regions. While the POLMIP project specified a common

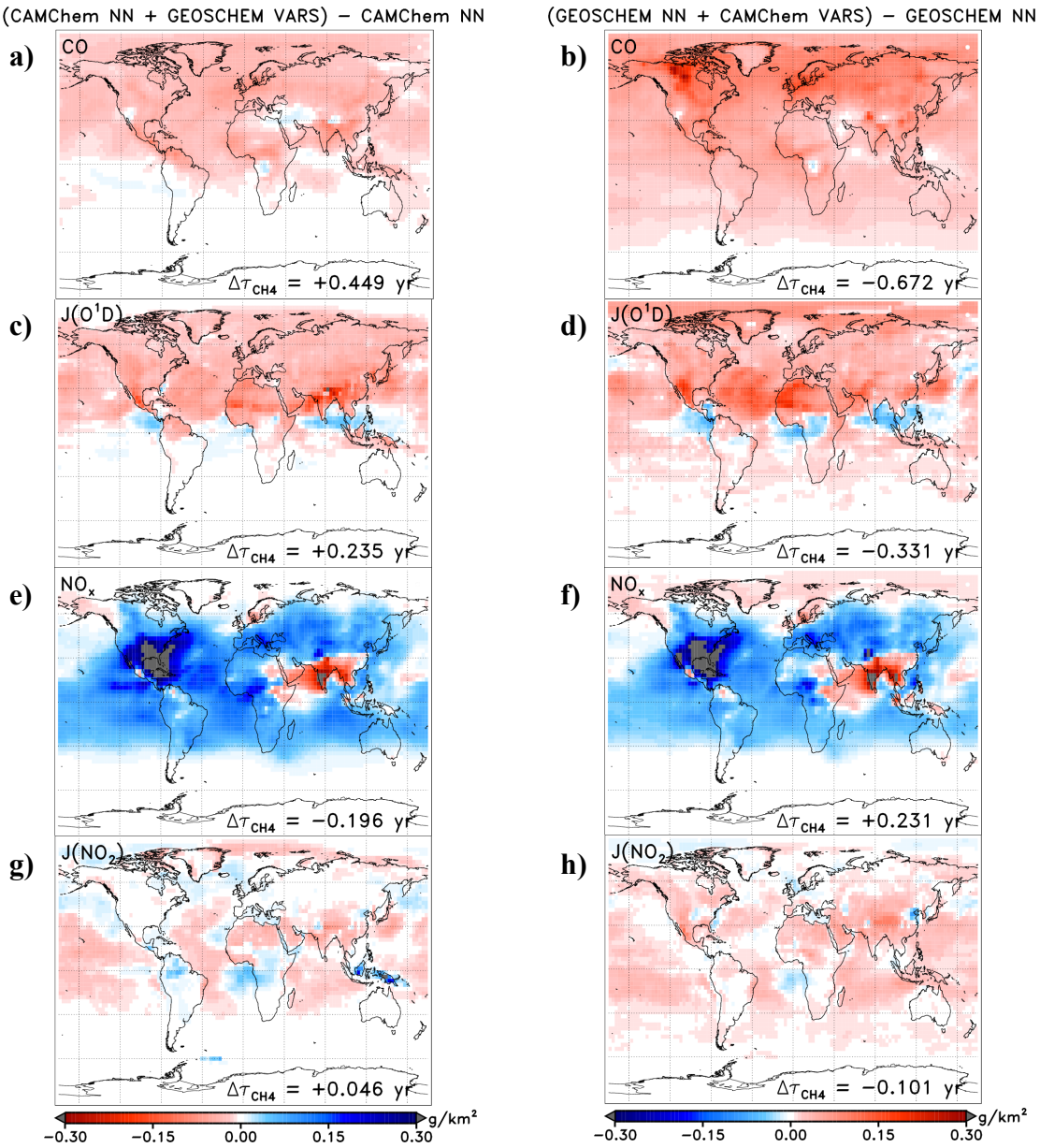

Figure 3-4. Tropospheric column mass OH differences for various inputs swapped between GEOS-Chem and CAM-Chem NNs. Left shows OH differences from CAM-Chem's NN arising as a result of replacing CO (panel a), $J(O_3 \rightarrow O(^1D))$ (c), NO_x (e), and $J(NO_2)$ (g), from top to bottom, with that from GEOS-Chem; right shows the same specie swaps from CAM-Chem into the GEOS-Chem NN (panels b, d, f, h). Tropospheric columns are calculated with $k_{OH+CH4} \times [CH_4]$ weighting. Difference in τ_{CH4} between the O_3 swap run and the base run is inscribed in the lower right corner of each plot.

emissions inventory for use by all CTMs, it is possible that the implementation of the inventory in the various models differs or that nitrogen chemistry (including sequestration of NO_x to reservoir species such as peroxyacetyl nitrate) evolves in a different manner following emission. Variations in CTM parameterizations of

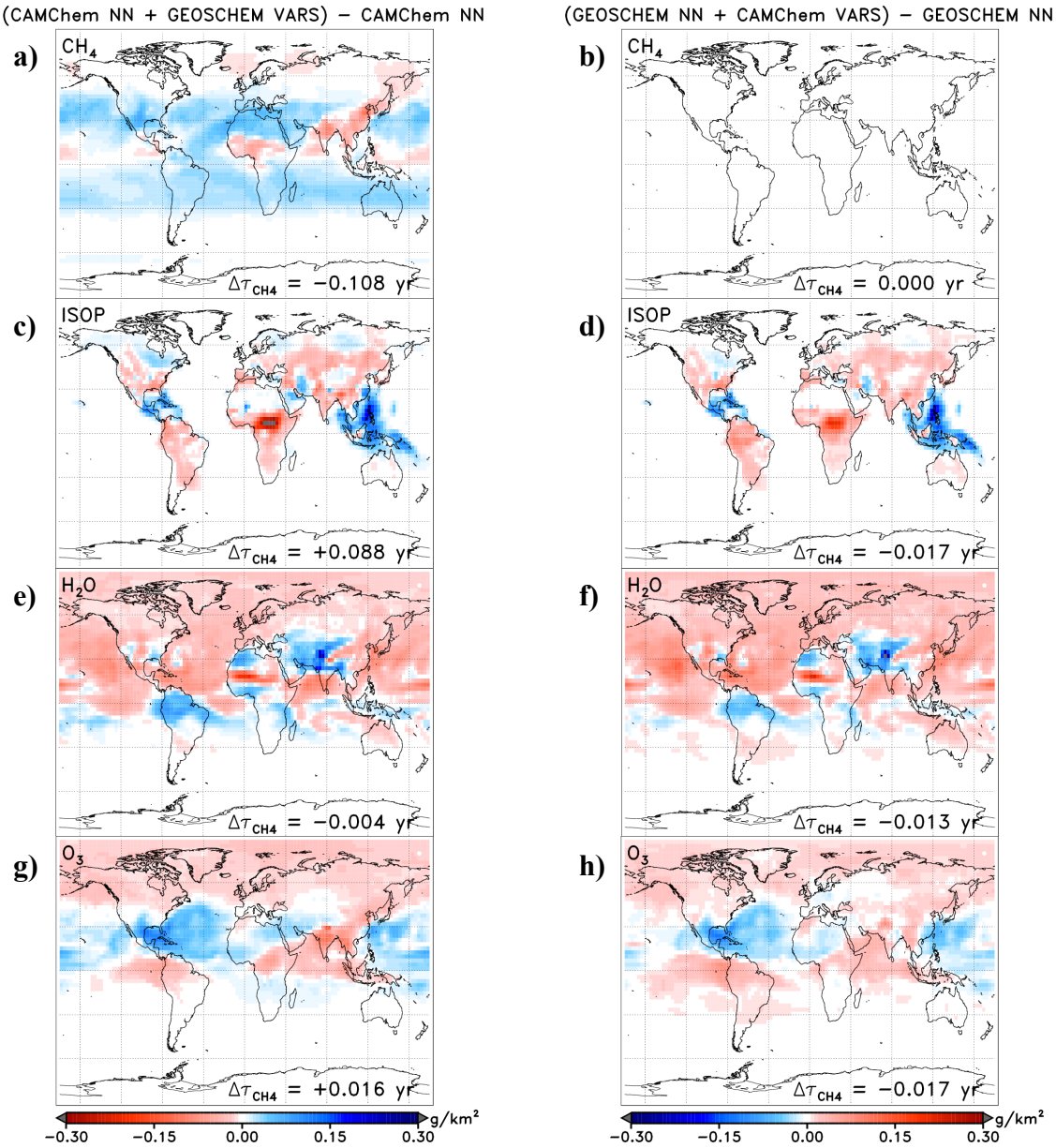

Figure 3-5. Same as Figure 3-4 except for swaps between the variables CH_4 (panels a and b), isoprene (c, d), H_2O (e, f), and O_3 (g, h), from top to bottom.

lightning NO_x could also account for the large differences in OH resulting from the NO_x swaps. Most interestingly, while there are considerable regional differences in the tropospheric mass of OH resulting from the swap of NO_x, the resulting difference in τ_{CH4} is modest. Regions of enhanced OH in one region (Central America) tend to be offset by regions of suppressed OH in other areas (India and SE Asia).

Swaps of isoprene (Figures 3-5c and d) show almost complete localization of resulting OH differences to continental source regions, due to the short lifetime of isoprene. As for NOx, the isoprene driven variations in OH could result either from differences in the implementation of isoprene emission or from alternate representations of the impact on OH of isoprene oxidation, an area of active current research [*Mao et al.*, 2013b].

Differences in OH driven by photolysis frequencies ($J(O_3 \rightarrow O(^1D))$ in Figure 3-4c and d; $J(NO_2)$ in Figure 3-4g and h) exhibit more global uniformity than differences driven by NO_x and isoprene. Variations in $J(O_3 \rightarrow O(^1D))$ generally arise from differences in overhead O_3 column, which exhibits considerable range among these 8 CTMs (not shown). The differences in $J(O_3 \rightarrow O(^1D))$ between CAM-Chem and GEOS-Chem are consistent with the direction of change in OH shown in Figures 3-4c and 3-4d. The cause of differences in $J(NO_2)$, on the other hand, is various model representations of cloud coverage. Variations in the CTM fields of overhead O_3 and clouds are manifest on a global scale, resulting in differences in OH due to photolysis frequencies that have comparable magnitude across continents and oceans. Even so, OH features are still distinguishable, such as the strong increase in OH over Indonesia in the CAM-Chem NN due to $J(NO_2)$ (Figure 3-4g). Since all models have not output a variable containing information on cloud coverage for the POLMIP archive, we can only surmise that the CAM-Chem treatment of clouds over Indonesia differs from that within GEOS-Chem.

Values of $\Delta\tau_{CH4}$ are also imprinted on each panel of Figures 3-4 and 3-5. These numbers represent the change in τ_{CH4} occurring as a result of using the

specified input from another CTM. As for the spatial distribution of OH mass differences, values of $\Delta\tau_{CH4}$ shown on the left and right hand side of each row are expected to be opposite in sign and of roughly the same magnitude. Inspection of these figures shows this expectation is generally met, further validating proper behavior of the NNs.

We also show results for the swapping of inputs between the LMDZ and TOMCAT NNs (**Figures 3-6** and **3-7**). These two CTMs exhibit the largest difference in τ_{CH4}; LMDZ has the longest lifetime (9.8 years) whereas TOMCAT has the shortest value (6.7 years) (Table 3-2). While some of the variable swaps indicate large values for $\Delta\tau_{CH4}$ (H_2O in Figure 3-7e and f; NO_x in 3-6e and f), the sum of the eight values of $\Delta\tau_{CH4}$ for swapping in one direction (0.646 years for left hand panels) or the other direction (−1.016 years) does not account for the ~2.5 year difference in τ_{CH4} between these two CTMs for the month of July. We conclude therefore that a considerable portion of the variation in OH between LMDZ and TOMCAT is therefore due to differences in chemical mechanism within these two CTMs.

Upon examination of the 2,016 tropospheric mass OH difference plots generated by our NN analysis (8 models combined with 7 possible pairs; for the 8 variables shown above plus the 9th variable temperature, times 4 months), it is important to note several points. As noted above, the pairings of tropospheric column mass OH difference plots and $\Delta\tau_{CH4}$ values for swaps of precursor fields in both directions are expected to demonstrate some level of visual and quantitative symmetry. There are however instances where this symmetry is lacking. The cause of this may be twofold. First, the chemical mechanism inherent to the respective

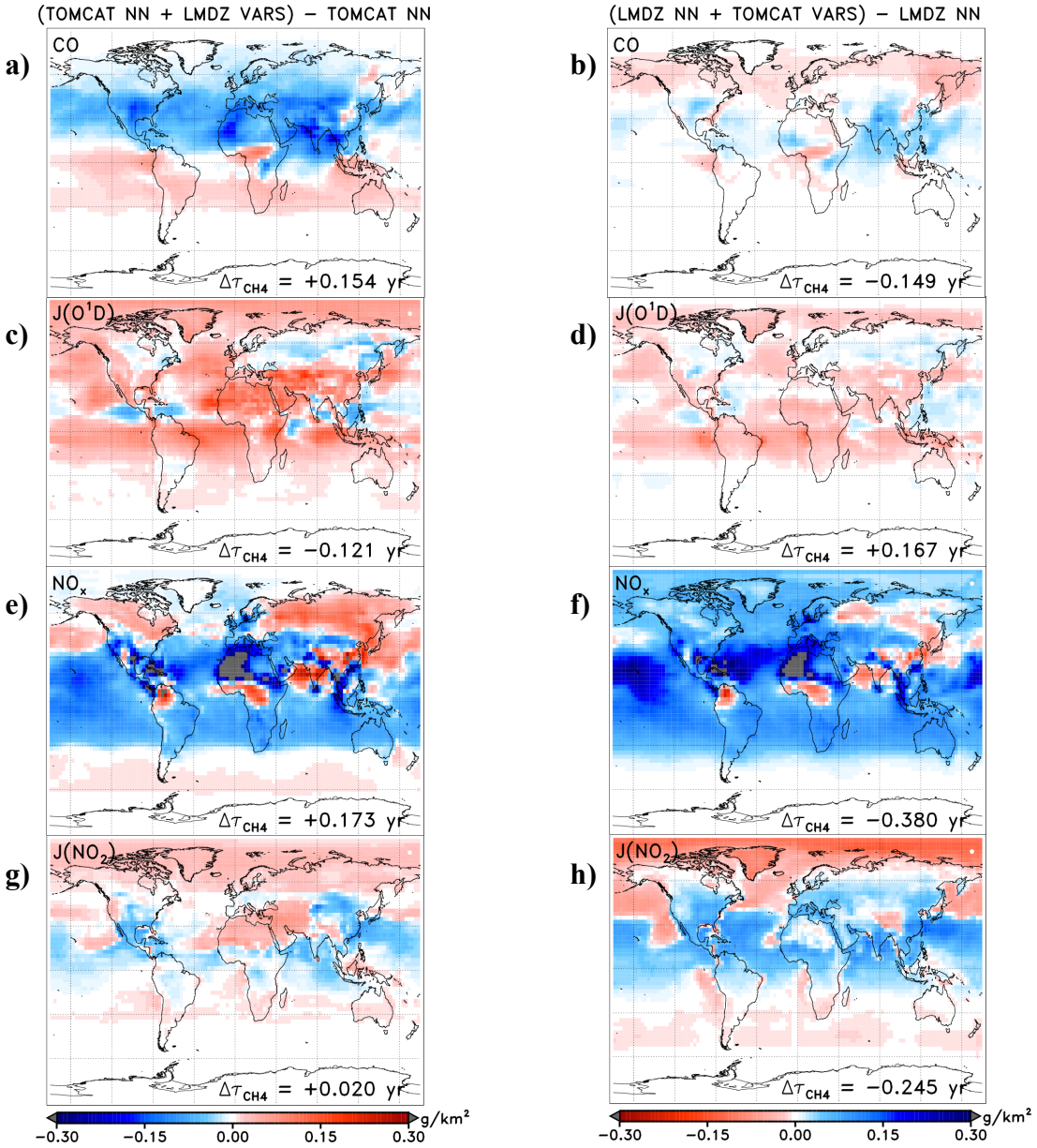

Figure 3-6. Tropospheric column mass OH differences for various inputs swapped between TOMCAT and LMDZ NNs. Left shows OH differences from TOMCAT's NN arising as a result of replacing CO (panel a), J(O_3→$O(^1D)$) (c), NO_x (e), and J(NO_2) (g), from top to bottom, with that from LMDZ; right shows the same species swaps from TOMCAT into the LMDZ NN (panels b, d, f, and h). Tropospheric columns are calculated with k_{OH+CH4}×[CH_4] weighting. Difference in τ_{CH4} between the O_3 swap run and the base run is inscribed in the lower right corner of each plot.

CTMs may exhibit differing responses to the variable being swapped. The second cause may be due to the extrapolation control method used to confine substituted variables to the range of values for which the NN was trained. If one CTM produces a wide range of tropospheric values, e.g. for CH_4, while a second confines the species

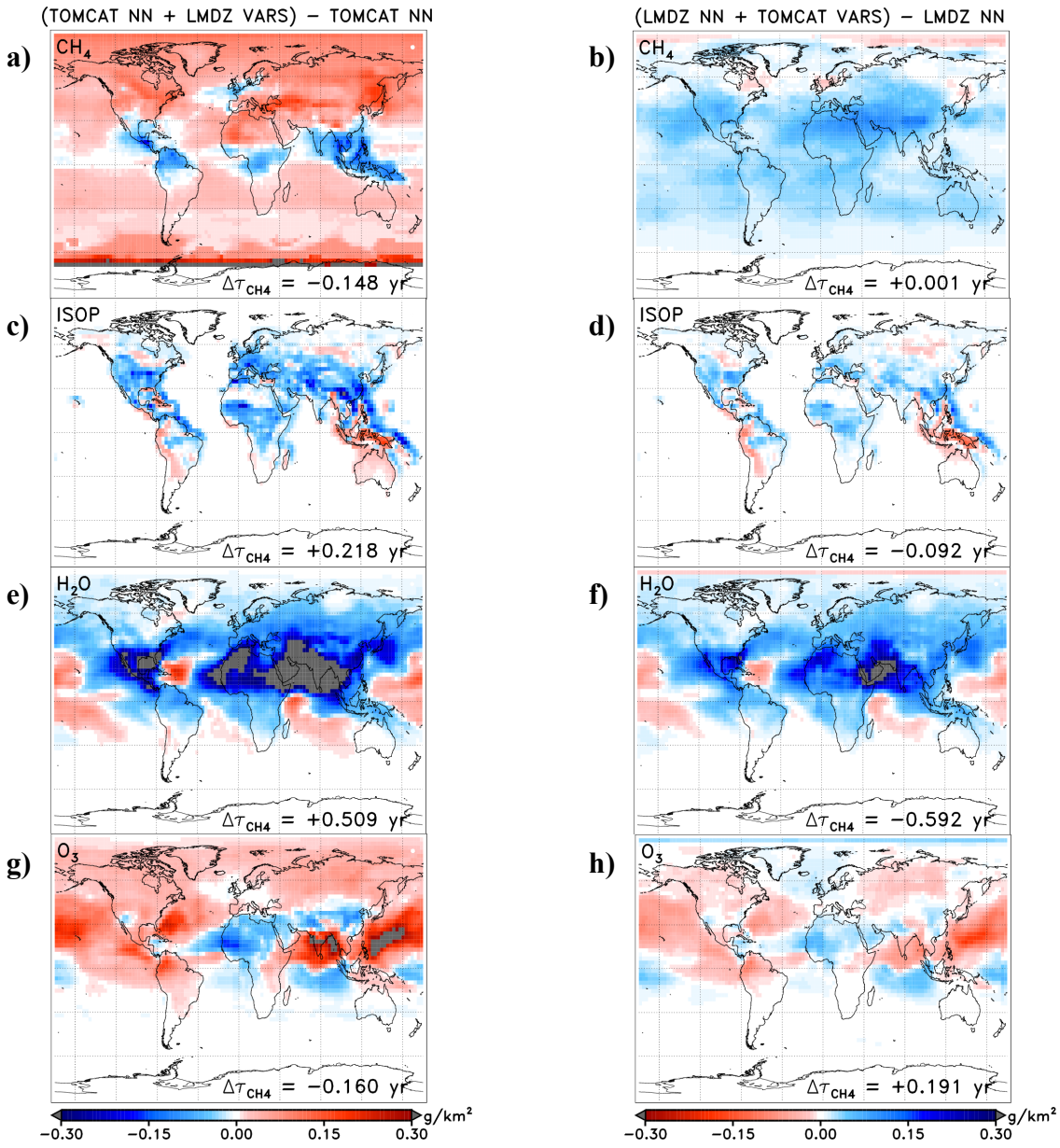

Figure 3-7. Same as Figure 3-6 except for swaps between the variables CH_4 (panels a and b), isoprene (c, d), H_2O (e, f), and O_3 (g, h), from top to bottom.

to a very narrow range, the swap in CH_4 values between the two CTMs' NNs will be asymmetric. Extrapolation control will allow the NN of the first CTM to test the full range of the field of CH_4 generated by the second CTM, whereas the CH_4 values from the first CTM will need to be heavily revised to fall within the narrow "trained range" before being input to the NN of the second CTM. An extreme case of this

phenomenon is seen in the CH_4 swap between CAM-Chem and GEOS-Chem: mixing ratios of CH_4 within GEOS-Chem are prescribed as 1740 ppb throughout the troposphere in the POLMIP archive. To prevent the extrapolation of the GEOS-Chem NN by using unfamiliar values of CH_4, all incoming CH_4 values must be set to 1740 ppb. The GEOS-Chem NN, therefore, is unable to represent the impact of CH_4 on OH, despite the fact that loss or production of OH (which depends on NO_x) via the oxidation of CH_4 is represented within the chemical mechanism of GEOS-Chem. For this reason, Figure 3-5b shows no effect of CH_4 on OH and τ_{CH4}. In order to assure scientifically meaningful results, great care must be used in NN analysis to assure the derived functions are interpolations, and not extrapolations due to the highly non-linear behavior of the basis functions. The only alternative to use the use of NNs to examine the cause of inter-model difference in modeled OH would be for each group to share the code of their chemical mechanism, which would then allow for the full range of swapped variables to be considered.

Another point to note is that regions in which strong differences in OH are calculated require two necessary conditions: 1) the variables being swapped between the respective NNs must be significantly different at the grid point, and 2) the NN must demonstrate a significant response of OH due to that variable. It is possible that differences in a swapped variable may be large, yet the response in OH is small due to the weak dependence of OH chemistry on that variable. Therefore, large differences in OH and τ_{CH4} indicate that a swapped variable is both significantly different between two CTMs and significantly impacts OH chemistry.

Table 3-3. Budgeting of τ_{CH4} between GEOS-Chem and CAM-Chem for July

		GEOS-Chem	CAM-Chem
$\tau_{CH4,\,ORIG}$[a] (years)		7.36	6.65
$\Delta\tau_{CH4}$ due to[b]:	O_3	−0.02	+0.02
	$J(O_3 \rightarrow O(^1D))$	−0.33	+0.24
	CO	−0.67	+0.45
	NO_x	+0.23	−0.20
	CH_4	+0.00	−0.11
	H_2O	−0.01	0.00
	$J(NO_2)$	−0.10	+0.05
	Isoprene	−0.02	+0.09
	Temp	0.00	0.00
$\Delta\tau_{CH4,\,TOT}$[c]		−0.92	+0.54
$\tau_{CH4,\,ORIG} + \Delta\tau_{CH4,\,TOT}$		6.44	7.19
Mechanism + non-linearities[d]		+0.21	+0.17

[a] $\tau_{CH4,\,ORIG}$ represents value of τ_{CH4} evaluated directly from the CTM
[b] $\Delta\tau_{CH4}$ calculated from output of NN when noted variable is substituted using values from the other CTM
[c] Sum of all $\Delta\tau_{CH4}$ values calculated for each input substitution
[d] "Remainder" of original τ_{CH4} difference not accounted for by NN substitutions; calculated as $\tau_{CH4,\,ORIG}$(CTM A) − [$\tau_{CH4,\,ORIG}$ (CTM B) + $\Delta\tau_{CH4,\,TOT}$ (CTM B)]

Upon performing swaps of all variables between two models, the information encompassed in the computed values of $\Delta\tau_{CH4}$ has been compiled for the purpose of budgeting differences in τ_{CH4} for particular model pairs. An example, for the GEOS-Chem and CAM-Chem CTMs, found using the July 2008 archive, is shown in **Table 3-3**. Here, the $\Delta\tau_{CH4}$ values due to all inputs are summed ($\Delta\tau_{CH4,\,TOT}$). It is often the case that the total $\Delta\tau_{CH4}$ accounts for the majority of the difference in τ_{CH4} between the parent CTMs (denoted by τ_{ORIG}). We attribute the remaining difference between ($\tau_{ORIG} + \Delta\tau_{CH4,\,TOT}$) from one model and the τ_{ORIG} of the second model to the sum of the two terms: variations in the chemical mechanisms of the two models (manifesting as differing OH sensitivities) plus differences driven by non-linearities of substituted inputs (resulting from asymmetrical extrapolation control, as described in the

previous paragraph). This term is referred to as "Mech.+Nonlin." in Table 3-3 and subsequent figures.

Table 3-3 shows that for the July 2008 POLMIP archive of GEOS-Chem and CAM-Chem, variations in the representation of CO by the respective CTMs is the largest single factor driving the 0.71 year difference in τ_{CH4}. The second most important factor is differences in the respective model's representation of $J(O_3 \rightarrow O(^1D))$. The third factor, and only other important parameter for this swap, is NO_x. The magnitude of the difference in τ_{CH4} due to mechanism plus non-linearities is nearly the same as the NOx swap. The quantification of the reasons for the difference in OH (and hence τ_{CH4}) between GEOS-Chem and CAM-Chem shown in Table 3-3 provides a roadmap for how to assess the oxidation capacity of the troposphere within these CTMs: one could, in theory, devise a means to compare fields of CO and $J(O_3 \rightarrow O(^1D))$ within these models to observations and thereby assess the computed fields. However, Table 3-3 represents just a single model pair, for a particular month. Below, we generalize Table 3-3 to represent the results from all possible model pairs, for all of the months, upon which some important conclusions will be drawn.

3.3.3 Aggregate Results for All POLMIP CTMs

The large number of comparisons conducted among 8 CTMs for 9 parameters in each of 4 months necessitates the aggregation of results to determine the primary drivers of differences in τ_{CH4}. The overall effect of one variable on the value of τ_{CH4} within a CTM is assessed by averaging the $\Delta\tau_{CH4}$ values due to substitution of that

variable from all of the other CTMs. The results of this analysis are shown in **Figure 3-8** for the four months considered and **Figure 3-9** for the average of these four months. The points show the mean and the error bars represent the standard deviation of the various swaps of the indicated variables. As for Table 3-3, the difference between the sum of the $\Delta\tau_{CH4}$ values for all of the swaps and the gap in τ_{ORIG} of the two parent CTMs is ascribed to chemical mechanism plus non-linearities (Mech.+Nonlin.). The variables are placed in order of decreasing important, with the

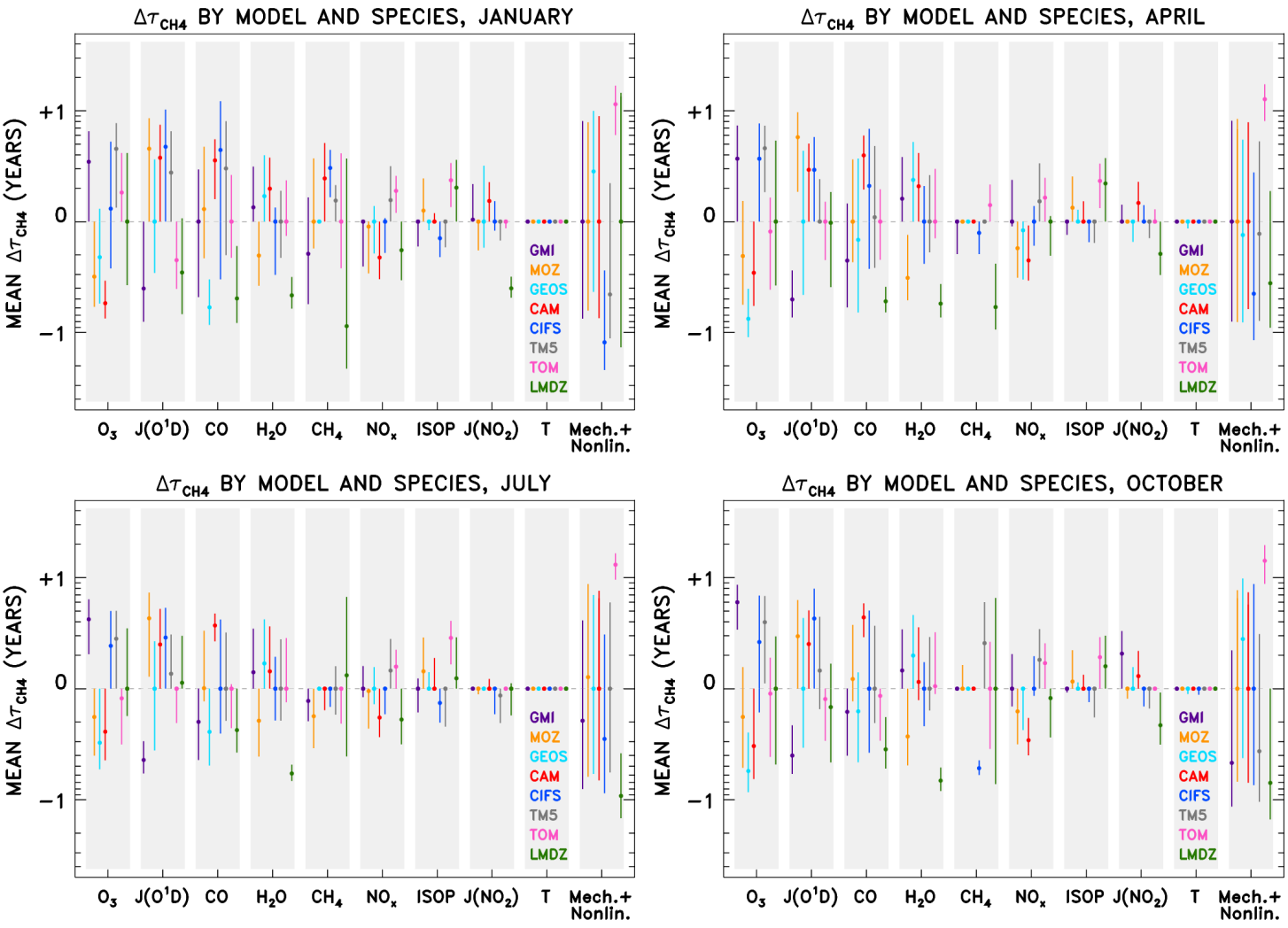

Figure 3-8. Changes in τ_{CH4} as a result of exchanging designated variable between all models, by month. Ranking of inputs along the x-axis occur in descending order of mean absolute value $\Delta\tau_{CH4}$ for all models. Error bars are standard deviation about the mean of all variable swaps between indicated model and all other models. "Mech.+Nonlin." represents the difference between parent CTM τ_{CH4} values not accounted for by the sum of $\Delta\tau_{CH4}$ values for each variable.

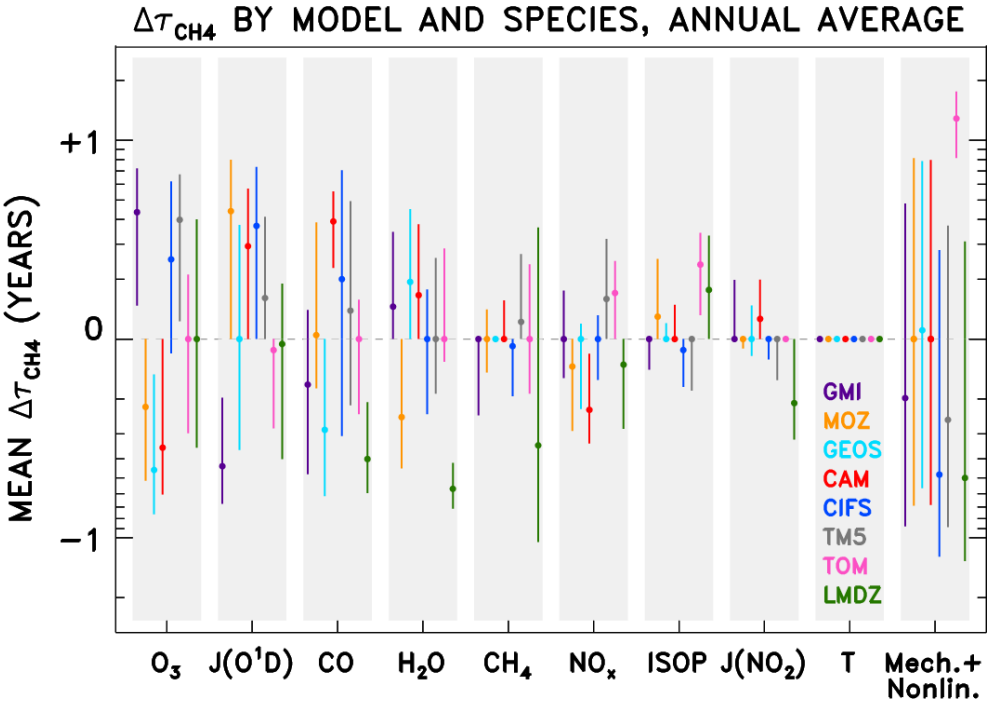

Figure 3-9. Same as Figure 3-8 except showing annual average results.

exception that Mech.+Nonlin. Appears last, representing the origin as a "remainder" term. Across all models, for the four months examined (Figure 3-8) as well as the average of these four months (Figure 3-9), O_3, $J(O_3 \rightarrow O(^1D))$, and CO consistently drive the highest mean absolute value of $\Delta\tau_{CH4}$. On average, the $\Delta\tau_{CH4}$ value resulting from model swaps of O_3 is 0.29 years, from $J(O_3 \rightarrow O(^1D))$ is 0.25 years, and from CO is 0.22 years. Water, CH_4, and NO_x rank as the fourth through sixth greatest drivers of τ_{CH4} differences, $J(NO_2)$ and isoprene occupy the seventh and eight positions, and temperature accounts for practically none of the difference in τ_{CH4}

Perhaps the largest surprise in this analysis is the small role ascribed to isoprene, despite the enormous effort being extended by the community to improve the representation of isoprene decomposition products in global models [*Crounse et al.*, 2011; *Mao et al.*, 2013b]. The small role for isoprene likely results from the short

lifetime that confines enhancements, relative to background, to the lowest few kilometer above active source regions. While the oxidation of isoprene is of great importance to surface O_3 [*Mao et al*., 2013b; *Canty et al.,* 2015; *Wolfe et al.*, 2015], it is less important for the τ_{CH4} because the reaction of CH_4 with OH takes place throughout the tropospheric column.

Inspection of the aggregated results reveals interesting patterns that provide insight into model behavior. The swaps for $J(O_3 \rightarrow O(^1D))$ show that GMI always has a lower mean data point for $\Delta\tau_{CH4}$ compared to the other models. This suggests that the $J(O_3 \rightarrow O(^1D))$ field native to GMI contributes a positive offset to τ_{CH4} from this model; i.e., when $J(O_3 \rightarrow O(^1D))$ from other models is substituted into GMI, τ_{CH4} always drops. Since τCH4 is proportional to the reciprocal of OH, this implies $J(O_3 \rightarrow O(^1D))$ from GMI is lower than this photolysis frequency in other models. This is confirmed by looking at the fields of $J(O_3 \rightarrow O(^1D))$ at a particular pressure level, 850 hPa, for each model (**Figure 3-10**).

We also provide plots showing tropospheric O_3 columns from each model (**Figure 3-11**) to further demonstrate the utility of this analysis. Figure 3-9 shows that GEOS-Chem has the lowest value of tropospheric O_3, since when O_3 is swapped from all other CTMs into the GEOS-Chem NN, OH consistently rises. The low value of O_3 within GEOS-Chem, relative to the other models, is apparent in Figure 3-11. While it is possible to compare each of these modeled fields visually or using a statistical method, the neural networking approach provides a means to analyze many variables in a consistent, quantitative, systematic manner that provides a means for assessing why τ_{CH4} varies between global chemical models.

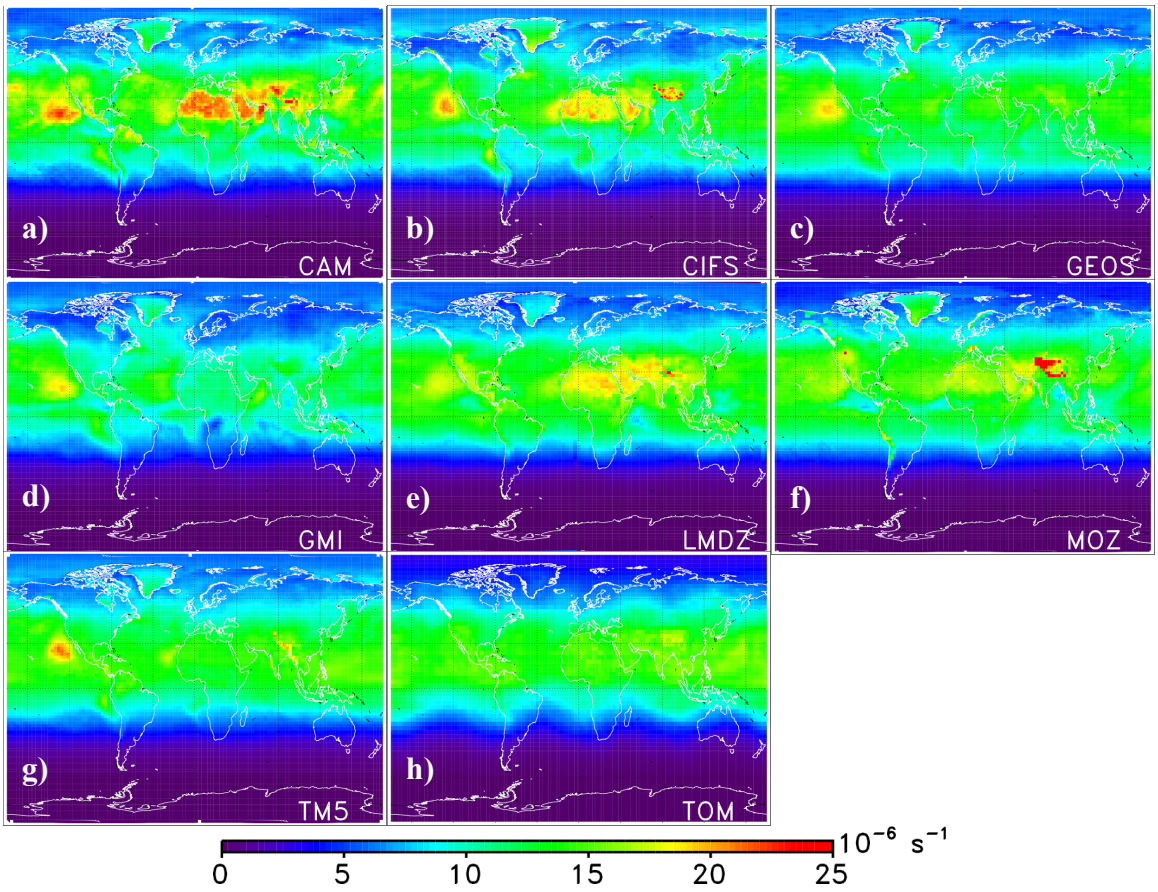

Figure 3-10. Monthly mean fields of $J(O_3 \rightarrow O(^1D))$ for July at pressure level closest to 850 hPa for the 8 POLMIP CTMs: CAM-Chem (panel a), C-IFS (b), GEOS-Chem (c), GMI-GEOS5 (d), LMDZ (e), MOZART4 (f), TM5 (g), and TOMCAT (h).

The Mech.+Nonlin. factor accounts for the largest values of $\Delta\tau_{CH4}$ across all months, with a mean absolute value of 0.38 for the average of the four months (Figure 3-9). Models that consistently have Mech.+Nonlin. data points that lie close to another model (i.e., MOZART and CAM-Chem) are presumed to have very similar chemical mechanisms. Models with that exhibit Mech.+Nonlin. data points that consistently differ from the other models, such as TOMCAT, presumably are running a different chemical mechanism than the other models. The NN analysis suggests the chemical mechanism within TOMCAT causes a reduction in τ_{CH4} of 1.29 years relative to the other 7 models and that the mechanism within LMDZ causes an

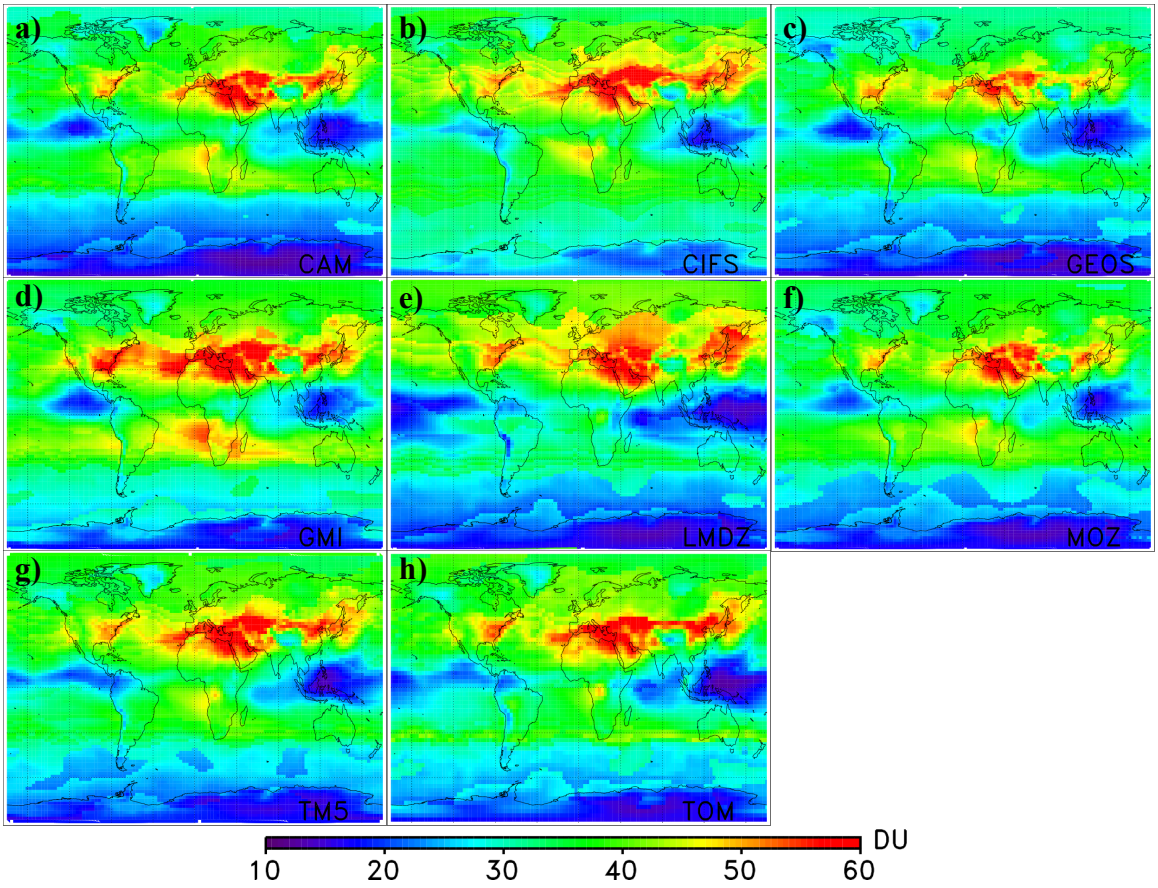

Figure 3-11. Monthly mean tropospheric O_3 columns in July for the 8 POLMIP CTMs: CAM-Chem (panel a), C-IFS (b), GEOS-Chem (c), GMI-GEOS5 (d), LMDZ (e), MOZART4 (f), TM5 (g), and TOMCAT (h). Tropopause pressures were calculated for individual models using a chemical tracer definition as defined in *Pan et al.*, [2004].

increase in τ_{CH4} of 0.5 years. As shown in Table 3-3, TOMCAT exhibits the smallest annual average value of τ_{CH4} (6.7 years) and LMDZ has the highest value (9.8 years). Our analysis suggests a considerable portion of these two outliers could be due to the chemical mechanism, provide of course that the primary driver of the Mech.+Nonlin. terms is indeed the mechanism.

The "Mech.+Nonlin." term also encompasses effects due to non-linearities either inherent within the chemical mechanism or accrued by asymmetric variable swapping. It is known, for instance, that the production or loss of OH, upon oxidation of CH_4, is a sensitive function of NO_x [Section 11.3.3 of Jacob,

Introduction to Atmospheric Chemistry]. The true dependence of OH as a function of CH_4 and NO_x may not be properly represented by summing the individual contributions from swapped CH_4 and swapped NO_x. Also as discussed in Section 3.2, the method we use to prevent NNs from extrapolating outside of the input ranges on which they are trained can result in asymmetry of the swapped variables; the extent to which this occurs can also increase the remainder Mech.+Nonlin. term. By tracking the number of swapped inputs into a given CTM's NN that invoke extrapolation control, i.e. are adjusted up or down to lie within the trained range of the NN, the TOMCAT model has the 2nd largest percentage of adjusted points (11.2%). However, the CTM with the largest number of extrapolation-controlled inputs is GEOS-Chem (17.1%), for which we see a near-zero value for the Mech.+Nonlin. term. This number may be heavily influenced by the CH_4 swaps, during which nearly all substituted values must be replaced with GEOS-Chem's constant CH_4 mixing ratio. The 3rd highest percentage of extrapolation-controlled points occurs for LMDZ, which has the lowest Mech+Nonlin. term. However, as noted above, LMDZ has the highest value for τ_{CH4}, consistent with the sign and magnitude of the Mech.+Nonlin. term.

Further analysis is needed to elucidate the contribution of chemical mechanisms within CTMs to differences in OH and hence τ_{CH4}. We suggest that, for future model intercomparison projects, each group be asked to run their mechanism in box model mode for prescribed inputs of the 9 primary drivers of OH used here, perhaps extracted from a single global model run for a diversity of atmospheric

conditions, so that the true variation of OH due to chemical mechanism can be quantified.

3.4 Discussion

We have shown that O_3, CO, and $J(O_3 \rightarrow O(^1D))$, in addition to the chemical mechanism and non-linearities, drive the greatest difference in τ_{CH4} among the CTMs that participated in POLMIP. While we identify these parameters as areas for further examination, we suggest that Figure 3-9 could serve as a useful guide to the behavior of how a particular CTM differs from others. For instance, GMI has relatively low $J(O_3 \rightarrow O(^1D))$, LMDZ has relatively low H_2O, CAM-Chem has relatively low CO, and GEOS-Chem has relatively low O_3. All results are relative to other models included in the intercomparison; evaluation of the accuracy of τ_{CH4} relative to the real atmosphere must be obtained through comparison to observations of the precursor fields, and of course measurements of OH.

Fortunately a prime opportunity to constrain τ_{CH4} using observations is forthcoming. The recently funded NASA Atmospheric Tomography Experiment (ATom) field campaign [*NOAA*, 2014] will have the DC-8 aircraft fly along transects up and down the Pacific and Atlantic Oceans, with a full chemistry payload of instruments onboard, including the measurement of OH via laser-induced fluorescence with the Airborne Tropospheric Hydrogen Oxides Sensor (ATHOS) [*Brune et al.*, 1998]. The first scientific question ATom seeks to address is "What are [the] chemical processes that control the short-lived climate forcing agents CH_4, O_3, and BC in the atmosphere?" This venture will be of great utility in diagnosing OH in

global models. Flights will take place primarily over the oceans; the background atmospheric composition sampled in these regions is likely most important in driving the τ_{CH4} differences among the models we work with here, since oceans account for the largest surface area within the band of tropical high OH. A straightforward analysis was performed in which we calculated the sum of the model grid box air mass as well as the denominator in Eq. 1 over land and over ocean separately. About 75% of the loss of CH_4 due to reaction with OH within the POLMIP CTMs occurs due to grid boxes that reside over ocean. On the other hand, there is a larger variation in OH over land (standard deviation about the mean of 15.1%) within these CTMs than over the ocean (standard deviation of 9.3%). While sampling of OH and related species over land would be preferable, it is likely the larger importance of loss of CH_4 due to reaction with OH over oceans will allow data from ATom to definitively assess and improve the representation of τ_{CH4} within CTMs.

As noted above, there is widespread recent interest in the influence of isoprene on HO_x [*Crounse et al.*, 2011; *Mao et al.*, 2012; *Taraborrelli et al.*, 2012; *Mao et al.*, 2013b]. However, our primary analysis (Figure 3-9) suggests that isoprene is not a large factor affecting τ_{CH4} differences. To look into this further, we repeated the analysis in the previous paragraph, using an "elevated isoprene" mask rather than a land mask. The mask was determined by flagging model grid points where the multi-model mean isoprene mixing ratio exceeded 0.05 ppb over land and at pressures greater than 700 hPa. Then, separately for each model, the summed air mass and summed OH terms were determined for the flagged locations. Air mass included within elevated-isoprene regimes only account for 3.3% of the total

tropospheric air mass. The OH term is enhanced relative to this value, with 8.2% of tropospheric OH residing in air with elevated isoprene. These values confirm that isoprene likely has a small role in influencing the difference in τ_{CH4} among the 8 POLMIP CTMs. The short lifetime and localized abundances of isoprene restrict its importance to the regions of biogenic origin.

A final caveat that must be noted is possible co-dependency of variables. The primary production on OH depends on O_3, $J(O_3 \rightarrow O(^1D))$, and H_2O, and these three parameters could vary in a manner that could complicate the analysis. For example, if higher photolysis (relative to other models) happens to lead to greater loss of local O_3, it is possible that the effect of these two factors cancel and primary production of OH remains unaffected. A cursory evaluation of this effect has been conducted by regressing values of $\Delta\tau_{CH4}$ due to variable swaps of O_3 against $\Delta\tau_{CH4}$ found from the variable swaps of $J(O_3 \rightarrow O(^1D))$ (**Figure 3-12**). Five models—GMI, MOZART, CAM-Chem, TOMCAT, and LMDZ—demonstrate a near-cancellation between these two factors, suggesting that net primary production is likely not driving any difference in τ_{CH4} among these 5 CTMs. This means the net effect of O_3 and $J(O_3 \rightarrow O(^1D))$ on τ_{CH4} may be null for these models, in which case differences in CO are the single largest driver of variations in τ_{CH4} between these CTMs. However, data points for the other 3 CTMs (CIFS, GEOS-Chem, TM5) lie far from the one-to-one line in Figure 3-12, suggesting the primary production of OH is quite different in these models.

Further development of this technique is encouraged to best reproduce model

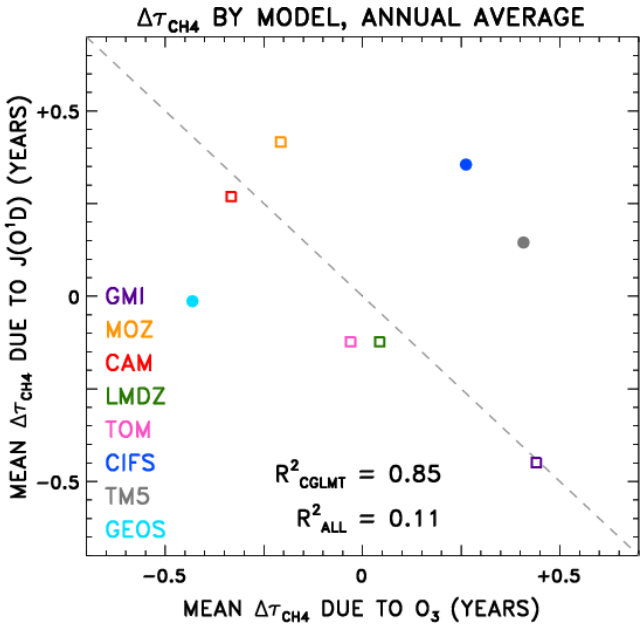

Figure 3-12. Regressions of $\Delta\tau_{CH4}$ values due to $J(O_3 \rightarrow O(^1D))$ versus O_3 based on the annually averaged results for each model. Noted on the figure are the r^2 values when considering all points ("R^2_{ALL}") as well as when considering only GMI, MOZART, CAM-Chem, LMDZ, and TOMCAT ("R^2_{CGLMT}").

OH chemistry through NN training. Persistent regions of disagreement between a NN and its CTM, such as over certain continental regions, likely indicate the exclusion of a parameter in the NN that is influencing OH chemistry in the CTM. While a strength of this technique is the ability to perform the analysis with a minimal amount of model output, it is probably worthwhile to explore the impact of inclusion of other species like HCHO, HONO, other VOCs, and lightning NO_x. Alternative inputs, such as OH chemical production and loss terms, might also be considered, with applications more directed toward studying the chemical mechanisms that drive OH. Additionally, while the NN architectures used here were thoroughly vetted in terms of minimizing errors and maintaining reasonable computation times, it is likely that more powerful computers could efficiently train neural networks with more nodes, more hidden layers, or both.

3.5 Conclusions

Neural networks were used to quantify the factors driving differences in tropospheric OH and the methane lifetime, τ_{CH4}, among the CTMs that participated in POLMIP. Annual mean values of τ_{CH4} ranged from 6.7 years for the TOMCAT model to 9.8 years for the LMDZ model. NNs were trained to reproduce monthly mean 3-D fields of OH mixing ratios for each CTM using inputs of H_2O, O_3, NO_x, CO, CH_4, isoprene, $J(O_3 \rightarrow O(^1D))$, $J(NO_2)$, pressure, latitude, and temperature. Trained NNs were then used to estimate the effect on OH of replacing individual input fields with fields from another CTM. Values of $\Delta\tau_{CH4}$ indicate to what degree a given input is influencing model differences in τ_{CH4}. Overall, O_3, CO, and $J(O_3 \rightarrow O(^1D))$ account for the largest variation of $\Delta\tau_{CH4}$ among the 8 CTMs, along with indirectly evaluated differences in model chemical mechanism and non-linearities in the variable swaps. On an annual basis and across all model pairings, O_3 accounted for an average model $\Delta\tau_{CH4}$ of 0.29 years, $J(O_3 \rightarrow O(^1D))$ accounted for that of 0.25 years, and CO accounted for 0.22 years. In 5 out of 8 CTMs, we show the effect on τ_{CH4} from variations in the primary production of HOx resulting from co-linearity of local O_3 and $J(O_3 \rightarrow O(^1D))$ tend to cancel; it is therefore possible that between these 5 CTMs, CO is the dominant factor driving inter-model spread in τ_{CH4}. While these results are representative of average $\Delta\tau_{CH4}$ values across all model pairings, it is useful to examine individual model results to understand which fields should be targeted for further examination for any one CTM.

The neural network method described here provides a computationally efficient way to approximate the OH chemistry implemented within various CTMs,

without access to the detailed chemical mechanism. Output requirements for the archive are not burdensome and multi-model intercomparisons can be conducted in a straightforward manner, provided all modeling groups archive the same chemical fields. Trained neural networks can perhaps be further developed for future evaluations of coupled climate chemistry models, as well as for comparisons of model output to global measurements of OH and related chemical compounds, such as the data that will be provided by the upcoming NASA ATom campaign.

Chapter 4: Empirical Analysis of the Change in Tropospheric OH Global Burdens Over the Last Several Decades

4.1 Introduction

The atmospheric lifetime of CH_4 is a crucial component to modeling the future effects of climate change accurately. The loss of CH_4 in the atmosphere is dominated by its reaction with hydroxyl radical (OH) in the troposphere [*Lelieveld et al.*, 1998]. Due to its important role in oxidizing CH_4 and many other atmospheric species, we strive to understand the global burden and time-varying evolution of tropospheric OH ("$[OH]^{GLOBAL}$"). Numerous modeling and chemical inversion studies point to widespread gaps in our knowledge concerning the global burden, distribution, and chemistry of $[OH]^{GLOBAL}$. For example, global models disagree on the value of the CH_4 lifetime upon reaction with tropospheric OH (τ_{CH4}) by 60-80% [*Shindell et al.*, 2006; *Fiore et al.*, 2009; *Voulgarakis et al.*, 2013], models systematically underestimate τ_{CH4} on the order of 10-15% relative to values of τ_{CH4} inferred from methyl chloroform (MCF: CH_3CCl_3) inversions [*Prather et al.*, 2012; *Voulgarakis et al.*, 2013], and other methods of observational constraint suggest that models regularly misrepresent the hemispheric distributions of OH [*Naik et al.*, 2013; *Patra et al.*, 2014; *Monks et al.*, 2015; *Strode et al.*, 2015]. Furthermore, an investigation of interannual variability in $[OH]^{GLOBAL}$ using chemical inversion of MCF data by *Montzka et al.* [2011] finds that the interannual variability in $[OH]^{GLOBAL}$ between 1998-2008 is considerably smaller than previously estimated by MCF inversions conducted by *Prinn et al.* [2005] for the time period 1978-2004 and

Bousquet et al. [2005] for 1980-2000. Studies of future $[OH]^{GLOBAL}$ likewise find divergent views on how $[OH]^{GLOBAL}$ will respond to climate change given a common emissions scenario. *Voulgarakis et al.* [2013] show that 14 global models estimate the changes in $[OH]^{GLOBAL}$ between 2000 and 2100 to be anywhere between −20.6% and +2.4% for Representative Concentration Pathway (RCP) 8.5 [*Meinshausen et al.*, 2011; *van Vuuren et al.*, 2011], in which CH_4 abundances more than double by 2100; this is the scenario for which models achieve the highest level of agreement. Given the uncertainty in how $[OH]^{GLOBAL}$ has and will continue to respond to climate change, there is a need to understand what factors have controlled $[OH]^{GLOBAL}$ over a well-constrained time period. Our goal in this study is to empirically model changes in $[OH]^{GLOBAL}$ for 1985-2011 based on satellite observations of H_2O and column O_3. We also evaluate the role that expansion of the tropics, a phenomenon not captured in global models and potentially influencing OH chemistry, has in driving $[OH]^{GLOBAL}$ variability.

Primary OH production occurs via ozone (O_3) photolysis to excited state $O(^1D)$ followed by reaction with water vapor:

$$O_3 + h\nu\ (\lambda \leq 336\ \text{nm}) \rightarrow O(^1D) + O_2\,, \qquad \textbf{(R1)}$$

$$O(^1D) + H_2O \rightarrow 2OH \qquad \textbf{(R2)}$$

Because this formation pathway depends on H_2O abundance and the actinic flux at wavelengths ≤ 336 nm, the highest OH concentrations are found in the tropical lower- and mid-troposphere. In the tropics, stratospheric column O_3 is low, allowing greater penetration of UV photons to the troposphere than in the extra-tropics. This results in a tropical maximum for tropospheric production of $O(^1D)$. Also, warm temperatures cause $[H_2O]$, where brackets indicate number density, to be highest in the tropics, but

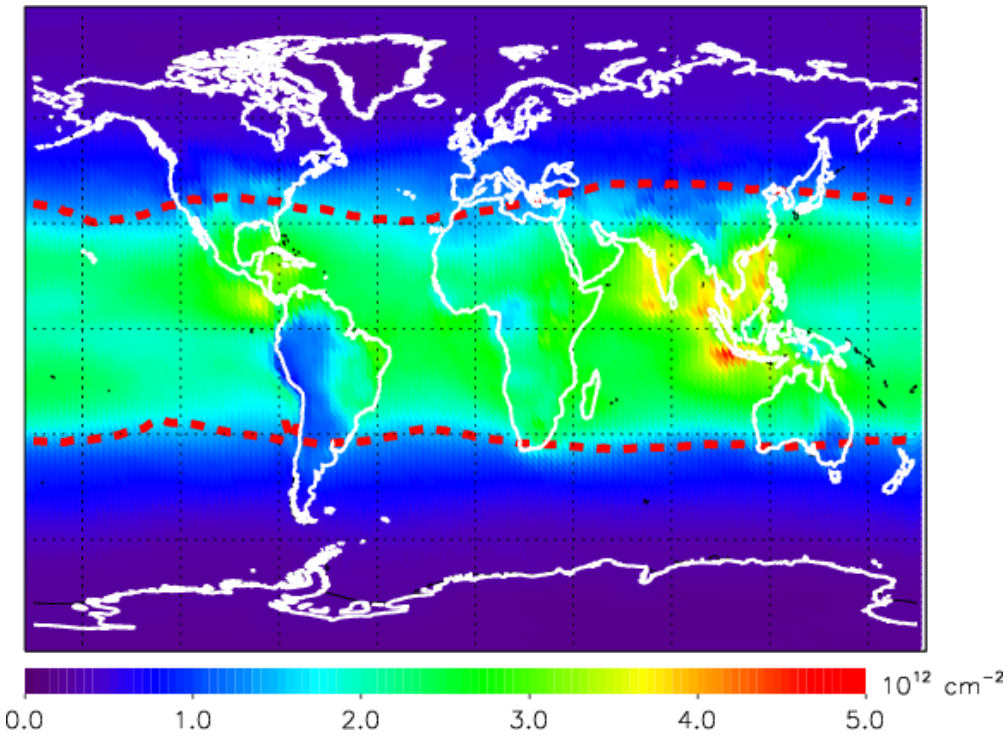

Figure 4-1. Annual average tropospheric OH columns calculated from output of the GEOS CCM model simulation using 2005 emissions upon which we base our analysis. The annual average extent of the climatological tropics are highlighted by the red dashed lines; these are calculated by finding the first latitude at which tropopause height exceeds 14 km when moving poleward from the Equator following the method of *Seidel and Randel* [2007].

decreasing pressure with respect to altitude restricts high [H_2O] to the lower to mid-troposphere. As a result, $[OH]^{GLOBAL}$ is dominated by OH in the tropics (**Figure 4-1**).

Recent evidence, based on numerous diagnostics of tropical extent, suggests the climatological tropics are expanding. This phenomenon can also be viewed as a strengthening or widening of the Hadley circulation, since the location of descent is generally regarded as the boundary between the tropics and extratropics. Numerous studies estimating the rate of tropical widening are summarized by *Seidel et al.* [2008] and further analyzed by *Davis and Rosenlof* [2012]. They include widening rates determined by analysis of observation-based tropopause heights [*Seidel and Randel*, 2007; *Lu et al.*, 2009; *Birner*, 2010], subtropical jet stream locations [*Fu et al.*, 2006;

Hu and Fu, 2007; *Archer and Caldeira*, 2008; *Fu and Lin*, 2011], meridional mass streamfunctions [*Mitas and Clement*, 2005; *Hu and Fu*, 2007], outgoing long-wave radiation [*Hu and Fu*, 2007], and total ozone (O_3) columns [*Hudson et al.*, 2006].

The findings of the observational studies of tropical widening noted above are often presented with inconsistent context; e.g., a rate of tropical widening may be presented for one hemisphere or for the global tropics, or for one decade versus a 25-year time period. To simplify interpretation of the literature, we summarize: early analyses estimated rates of expansion of the tropical belt, globally, as high as 3.0° decade^{-1} [*Seidel and Randel*, 2007]; however, refinement of methods (e.g,. avoiding subjectively-determined tropopause height thresholds) has resulted in much lower estimates of tropical widening rates [*Birner*, 2010; *Davis and Rosenlof*, 2012]. The most comprehensive analyses to date are *Davis and Rosenlof* [2012], who find that meridional mass streamfunction analyses give a robust 1.0°-1.5° decade^{-1} global rate of widening while other diagnostics suggest insignificant trends in tropical expansion, and *Allen et al.* [2014] who calculate rates of 0.35±0.09° decade^{-1} in the Northern Hemisphere and 0.17±0.10° decade^{-1} in the Southern Hemisphere (or 0.52±0.13° decade^{-1} globally). Despite the latest evidence that rates of Hadley cell expansion are lower than first suggested, concerns persist due to the inability of global models to simulate the extent of tropical widening witnessed to date [*Johanson and Fu*, 2009; *Allen et al.*, 2014]. Here we investigate the effect of tropical widening on $[OH]^{GLOBAL}$, which has yet to be considered.

The mechanism through which widening of the tropics likely affects OH chemistry is through effects on overhead O_3 amounts. Total column O_3 is lowest in

the tropics due to the upward motion of the Brewer-Dobson overturning circulation [*Seidel et al.*, 2008]. This large-scale flow pattern carries stratospheric O_3 from the tropics poleward, resulting in higher total column O_3 amounts in the extratropics and a boundary between high and low O_3 column that can be used to distinguish the extratropics from the tropics [*Hudson et al.*, 2006]. As with the Hadley circulation in the troposphere, modeling studies find that increasing greenhouse gas concentrations will result in strengthening of the Brewer-Dobson circulation [*Butchart et al.*, 2006; *Garcia and Randel*, 2008], so it logically follows that the region of low column O_3 will expand in conjunction with the climatological tropics–and this has been observed in observations of total column O_3 [*Hudson et al.*, 2006]. In the regions that transition from extratropical to tropical classification in the process of tropical expansion, lower column O_3 content will increase UV photon flux in the troposphere, which will increase the photolysis frequency of $O_3 \rightarrow O(^1D)$ and ultimately contribute to higher [OH].

We consider the effects of tropical widening and changes in overhead O_3 column on $[OH]^{GLOBAL}$ as independent factors in this analysis. The justification for doing so is that observed changes in total O_3 result from several factors not related to tropical expansion, including the decreasing atmospheric burden of halogenated compounds [*Butchart and Scaife*, 2001; *Li et al.*, 2009] and the injection of volcanic sulfate aerosols into the stratosphere [*Fahey et al.*, 1993]. We average the observed changes in O_3 column within latitudinal bins to derive the response in $[OH]^{GLOBAL}$; however, the effect of tropical expansion on OH only occurs in the much narrower latitude range over which the tropical boundary migrates. Thus, the other drivers of

stratospheric O_3 variability likely obscure the effect of tropical widening. In a multi-model comparison study, *Oman et al.* [2010] show that, while "super-recovery" of the O_3 column is expected at mid-latitudes following the decline of CFC abundances, a permanent depletion of O_3 column in the tropics is likely to occur, relative to pre-industrial times. These global-scale changes in O_3 column will likely affect $[OH]^{GLOBAL}$ and should be considered, in addition to the more local effects of tropical widening, to quantify the effect of climate change on future tropospheric composition.

In this study, we seek to empirically model the changes in $[OH]^{GLOBAL}$ that occurred between 1985 and 2011 by considering global observations of overhead O_3, H_2O, and CH_4 as well as the simulated effect of tropical expansion. The effect of each component on OH is evaluated based on fundamental principles of atmospheric chemistry, except for the effect of tropical expansion, which is simulated using estimates of the rate of tropical widening found in the literature. The resulting variability in $[OH]^{GLOBAL}$ evaluated from this analysis is then used to reconcile two seemingly disparate views of $[OH]^{GLOBAL}$ variability in the literature based on chemical inversion of methyl chloroform data.

4.2 Methods

4.2.1 GEOS CCM Model

We use a 3-D field of OH calculated by the Goddard Earth Observing System Chemistry Climate Model (GEOS CCM) as the starting scenario for the distribution

and burden of $[OH]^{GLOBAL}$. The GEOS CCM simulation is a time-slice run using prescribed boundary conditions representative of 2005 conditions. Monthly mean OH mixing ratios are output on a 2.5° longitude × 2° latitude spatial grid, with 72 vertical layers from the surface to 0.015 hPa. This version of the model combines the GEOS general circulation model [*Rienecker et al.*, 2008] with a troposphere-stratosphere chemical mechanism that includes 117 species, 322 thermal reactions, and 81 photolysis reactions, originally developed for the Global Modeling Initiative (GMI) chemical transport model [*Duncan et al.*, 2007; *Strahan et al.*, 2007]. The model is run as a CCM, i.e. using free-running meteorological variables. Further detail concerning the parameters of this particular simulation are available in *Lang et al.* [2012] (simulation name "TS2005").

4.2.2 Calculation of $[OH]^{GLOBAL}$

The calculation of $[OH]^{GLOBAL}$ requires a weighting to account for the diminishing area of higher latitude bands and the decreasing density of air at higher altitudes. In addition, a reactivity weighting is used to find a value of $[OH]^{GLOBAL}$ appropriate for oxidation of CH_4. We use mass and reaction rate weightings employed by *Lawrence et al.* [2001] (Equation 1).

$$[OH]^{GLOBAL} = \frac{\sum[\overline{OH}]_{box} \times k_{OH+CH4}(\bar{T}_{box}) \times Mass_{box}}{\sum k_{OH+CH4}(\bar{T}_{box}) \times Mass_{box}} \qquad (1),$$

Here, $[\overline{OH}]_{box}$ and $\bar{T}_{box}$ refer to average [OH] and temperature, respectively, at the eight gridpoints used to define a grid box. Summations occur for all latitudes, longitudes, and pressure levels within the troposphere. Tropopause altitudes are

calculated following the thermal tropopause definition of World Meteorological Organization [*WMO*, 1992].

4.2.3 Observational Data

Measurements of total column O_3 are obtained from the NASA Solar Backscatter Ultraviolet (SBUV) Merged Ozone Data Set (MOD), Release 3 (see *Frith et al.* [2014] and references therein). This data set combines measurements from the SBUV series of ultraviolet radiometers on board several satellites, the Total Ozone Mapping Spectrometer (TOMS) instruments that flew on board several satellites, and the Ozone Monitoring Instrument (OMI) on board the Aura satellite. Data are available for download at http://acd-ext.gsfc.nasa.gov/Data_services/merged/. Column O_3 values are provided as zonal monthly means in 5° latitude bins. The variations in total column O_3 seen in this data set are shown in **Figure 4-2**.

Water vapor data are from the Atmospheric Infrared Sounder (AIRS) instrument on-board the NASA Aqua satellite. We use the Level 3, Version 5 monthly product, which provides H_2O mixing ratios on a 1° × 1° latitude/longitude grid at 12 pressure levels ranging from 1000 to 100 hPa. Data are available for download at: http://disc.sci.gsfc.nasa.gov/AIRS/. However, since data from this satellite instrument are only available for September 2002 onward, we also analyze H_2O fields from the Modern-Era Retrospective Analysis for Research and Applications (MERRA) reanalysis data set. MERRA Version 1 monthly mean specific humidity values are extracted on a 0.625° latitude × 0.25° longitude grid for

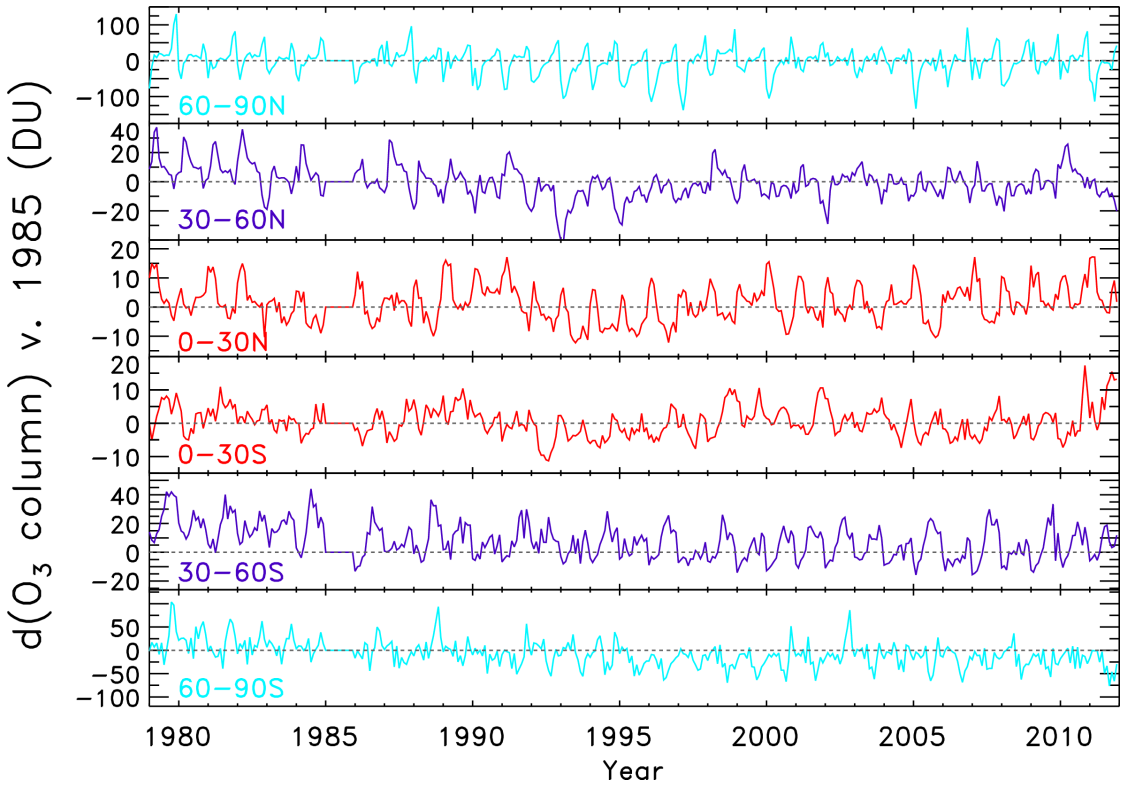

Figure 4-2. Variations in total column O_3 from the NASA merged O_3 data set, consisting of measurements from the SBUV, TOMS, and Aura OMI instruments, averaged within 30° latitude bins to represent the polar, mid-, and tropical latitudes, going north to south from top to bottom of the figure. Anomalies are calculated relative to 1985 average values.

23 pressure levels ranging from 1000 to 200 hPa. The MERRA data set extends back to 1979; so full coverage of our study period, 1985-2011, is used.

Methane data are obtained from the NOAA Global Cooperative Air Sampling Network, updated from that described by *Dlugokencky et al.* [2009]. Surface, globally averaged mixing ratios of CH_4 are provided as monthly means from data collected weekly at 46 remote measurement sites.

4.2.4 Calculation of the OH Response

4.2.4.1 Overhead O_3, H_2O, and CH_4

We start with our base 3-D field of OH mixing ratios obtained from the GEOS CCM model; the value of $[OH]^{GLOBAL}$ that we calculate from this model serves as our initial burden representative of 1985. We then calculate perturbations to this OH field and recalculate $[OH]^{GLOBAL}$ for subsequent years, for each factor we examine (overhead O_3, H_2O, CH_4, and tropical widening). Below, we describe the relationships between OH and these variables used to calculate the $[OH]^{GLOBAL}$ response.

Following a steady-state approximation for production and loss of the HO_x (=$OH+HO_2$) family of radicals, changes in [OH] are directly proportional to the square root of the change in $[O^1D]$ as well as $[H_2O]$. The effect of changes in total O_3 column on $[O^1D]$ are calculated using a radiative model [*Salawitch et al.*, 1994] with changes in $J(O^1D)$ assumed to be directly proportional to changes in $[O^1D]$. Concentrations of OH from the 3-D GEOS CCM global field are then increased or decreased proportionally to the time- and latitude-dependent calculation of $(\Delta[O^1D])^{1/2}$ and used to calculate a new $[OH]^{GLOBAL}$ value for each year.

The $[OH]^{GLOBAL}$ response to H_2O is calculated by first performing a linear least squares fit to the H_2O trends, averaged into 30° latitude bins for all pressures greater than 900 hPa (**Figure 4-3**). For a given latitude bin, that trend is used to determine a $\Delta[H_2O]$ value for the entirety of our study period (in the case of MERRA data) or for the years 2002-2011 (for AIRS H_2O data). The change for [OH] that falls

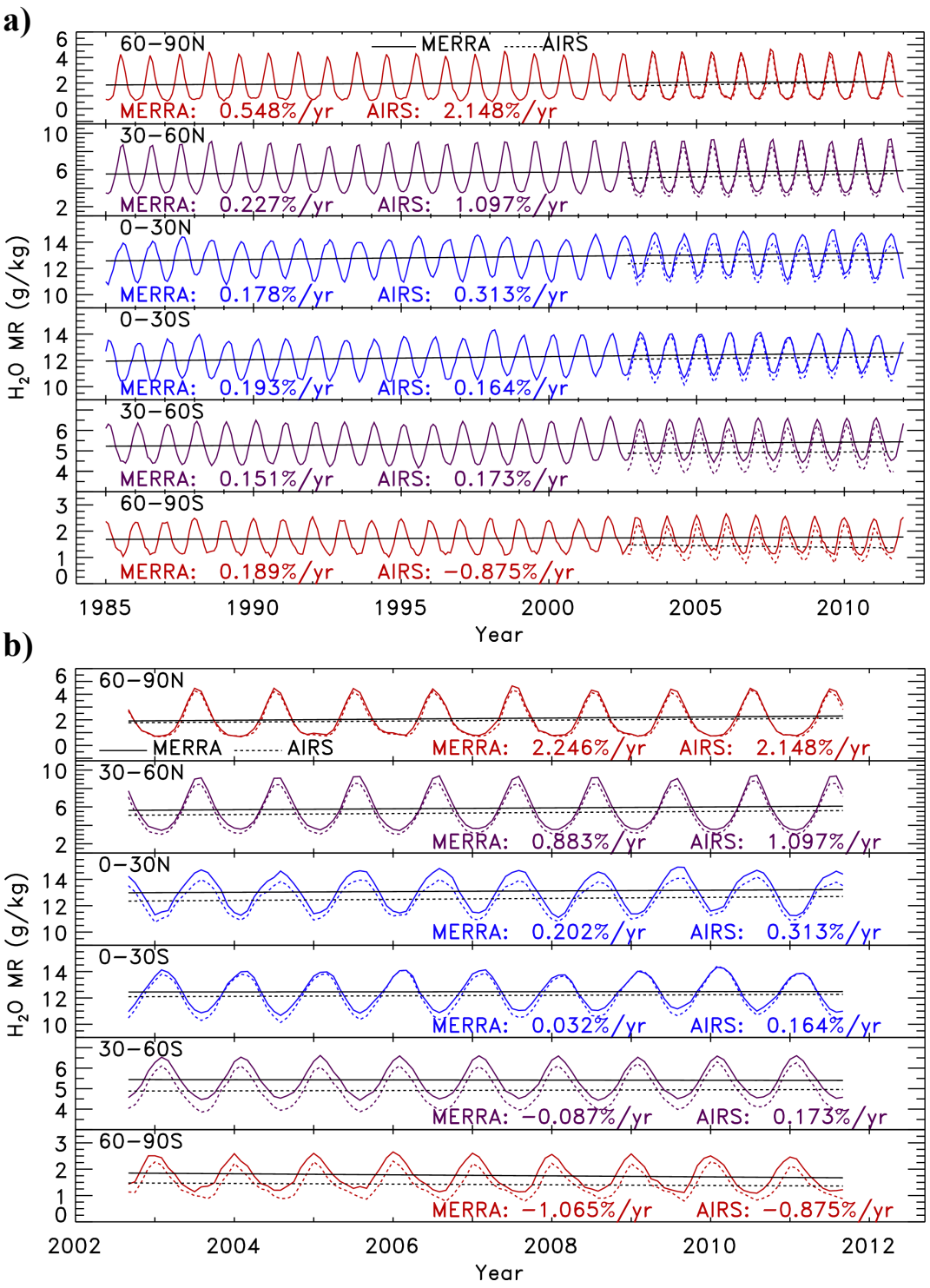

Figure 4-3. Variations in atmospheric H_2O for time periods 1985-2012 (panel a) and 2002-2012 (panel b), averaged for the same latitude bins described in Figure 4-2. Monthly mean values of water vapor are averaged for all data between the surface and 900 hPa from MERRA (solid line) and AIRS (dashed line); however, AIRS observations only extend back to September, 2002. Trends in the two data sets are calculated via linear least squares fit, with the best fit lines and slope noted in each panel.

within a given bin is calculated as $(\Delta[H_2O])^{1/2}$, from which a new $[OH]^{GLOBAL}$ value is determined.

The effect of CH_4 on $[OH]^{GLOBAL}$ is estimated using the relation from *IPCC* [2001], in which the feedback of CH_4 on OH was given as −0.32% for every 1% increase in CH_4. We use this straightforward relation to calculate a new $[OH]^{GLOBAL}$ for the monthly variations in global mean $[CH_4]$ relative to starting (1985) values.

4.2.4.2 Tropical Expansion

To simulate the change in $[OH]^{GLOBAL}$ that resulted from expansion of the tropics over the period of 1985-2011, we first have to determine the extent of the tropics in our initial 3-D field of OH from the GEOS CCM model. We use the bimodal distribution of tropopause heights, as discussed in *Seidel and Randel* [2007], to determine Hadley cell boundaries. *Seidel and Randel* [2007] determine that tropopause heights characteristic of tropical regimes occur at altitudes higher than 15 km, while extratropical tropopause heights occur below 13 km. To avoid the ambiguity of latitudes without a tropical or extratropical classification, we use the threshold of 14 km to identify the boundary between tropics and extratropics. The tropical boundary is determined as the first latitude poleward of the Equator at which tropopause height falls to < 14 km. We also tested the O_3 column [*Hudson et al.*, 2003], streamfunction [*Johanson and Fu*, 2009], and OLR [*Johanson and Fu*, 2009] definitions of tropical extent but found that averaging over the relatively short time span of 1 model year (from 12 monthly averages) was insufficient for producing smooth, unbroken tropical boundaries. We determine tropical boundaries using

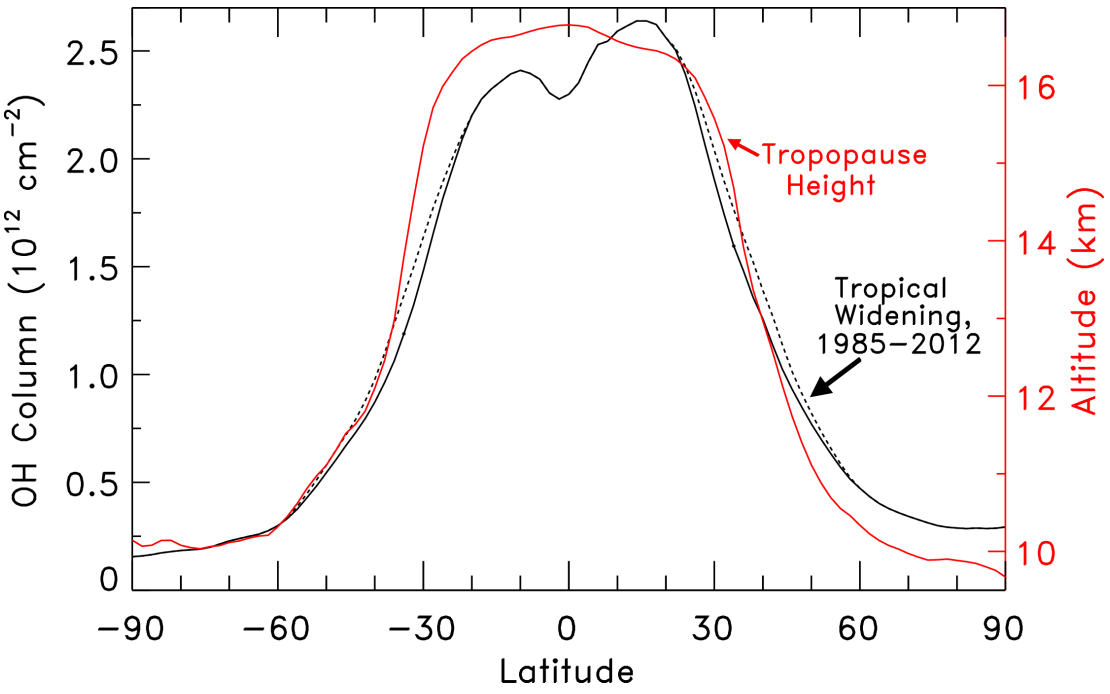

Figure 4-4. Zonal mean tropospheric OH column calculated for the base simulation of the GEOS CCM model (solid black line) and zonal mean tropopause height (red) plotted versus latitude. Also shown is our simulation of the effect on OH column values resulting from a 2°/decade (globally; 1° per hemisphere) widening of the climatological tropics for the duration of our study period.

tropopause height for each longitude, in both the Northern and Southern Hemispheres. The tropical boundaries that we identify are shown as red dashed lines in Figure 4-1.

The mechanism through which we expect tropical widening to affect $[OH]^{GLOBAL}$ is primarily through the change in overhead O_3, which in turn follows changes in the tropopause height [*Hudson et al.*, 2003]. By analyzing zonal mean values of tropospheric OH column, we clearly see the correlation of OH with tropopause height (**Figure 4-4**). We impose the effects of tropical widening by essentially widening the latitudinal distribution of tropospheric OH column values, seen in the dotted black line in Figure 4-4. This is done by placing anchor points at the lowest and highest latitudes that will bound our transition region, ±20° and ±60° for this analysis. The median tropospheric OH column value between 20° and 60° for

a given hemisphere (referred to as the midpoint) is then moved poleward by the number of degrees of tropical widening being imposed. Here, we use the rates of 0.5° decade^{-1}, 2.0° decade^{-1}, and 4.5° decade^{-1} to simulate a range of Hadley cell expansion scenarios and approximate the sensitivity of $[OH]^{GLOBAL}$ to such changes. The poleward shift of tropospheric OH columns maximizes at the midpoint and is interpolated to a shift of 0° at the anchor points. We calculate the fractional change in the tropospheric OH column at each latitude using this new distribution (dashed line, Figure 4-4) and apply this within our calculation of $[OH]^{GLOBAL}$.

4.3 Results and Discussion

The results of our $[OH]^{GLOBAL}$ analysis are shown in **Figure 4-5**. Our calculation of $[OH]^{GLOBAL}$ for the base field of OH from GEOS CCM is calculated to be 1.245×10^{6} cm^{-3}. This serves as our starting point in year 1985 (Figure 4-5, panel b). The time varying responses of $[OH]^{GLOBAL}$ to column O_3 and CH_4 are shown as green and red lines, respectively, while the overall trends in $[OH]^{GLOBAL}$ determined as a result of increases in H_2O and increases in the width of the tropics are shown as orange and purple lines, respectively. The total of the $[OH]^{GLOBAL}$ responses due to column O_3, H_2O, and tropical widening is shown as the blue line; these are considered the factors that convey a positive trend in $[OH]^{GLOBAL}$ that balances out the decrease in $[OH]^{GLOBAL}$ due to rising CH_4. The sum of all 4 responses, i.e. the blue line plus the red line in panel b, gives the total change in $[OH]^{GLOBAL}$ that emerges from this analysis (Figure 4-5, panel c).

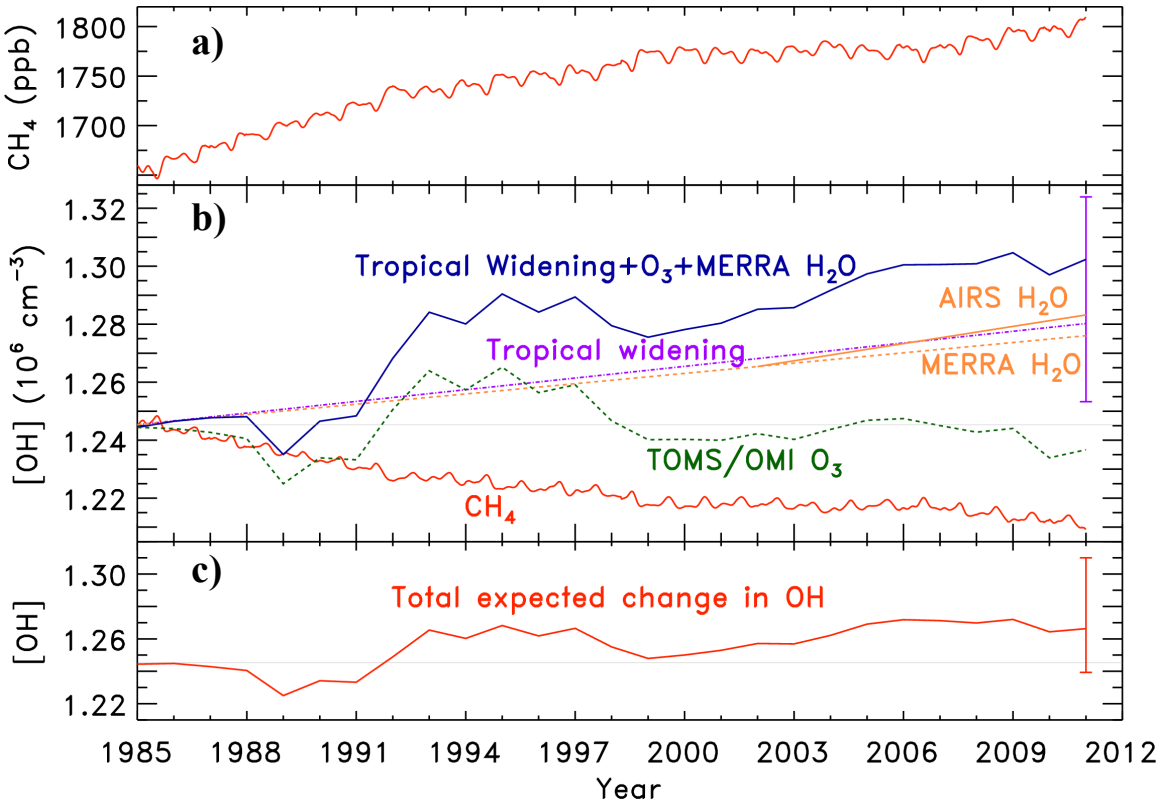

Figure 4-5. The time evolution of surface CH_4 for our study period obtained from the NOAA Global Cooperative Air Sampling Network, consistent with the data set described in *Dlugokencky, et al.* [2009], is shown in panel a). Panel b) shows our analysis of $[OH]^{GLOBAL}$ variations attributable to changes in overhead column O_3 (green dashed line), water vapor (obtained from the MERRA reanalysis, orange dashed line, and the AIRS instrument, orange solid line), CH_4 (red line), and widening of the tropics for a rate of 2°/decade globally (purple line). The error bar placed on the final point of the tropical widening line represents a range of possible $[OH]^{GLOBAL}$ values based on low and high estimates of the rate of tropical widening (0.5°/decade being the low limit, 4.5°/decade being the high). The dark blue line shows the sum of the $[OH]^{GLOBAL}$ values calculated for the column O_3, H_2O, and tropical widening effects. Panel c) shows the total expected change in $[OH]^{GLOBAL}$, calculated as the sum of the dark blue and red lines from panel b).

The overall trend in $[OH]^{GLOBAL}$ is effectively buffered by the 4 factors we examine. Higher $[OH]^{GLOBAL}$ variability prior to 1998, however, is attributable to the decrease in O_3 column that occurred as a result of the 1991 eruption of Mount Pinatubo [*Fahey et al.*, 1993]. Interestingly, our reproduction of a relatively high level of variability followed by plateauing in $[OH]^{GLOBAL}$ values may help to reconcile a debate ongoing in the literature. As mentioned in Section 4.1, *Montzka et al.* [2011] find that $[OH]^{GLOBAL}$ is well-buffered (interannual variability of ~2%)

between 1998-2008 while *Prinn et al.* [2005] and *Bousquet et al.* [2005] estimated much higher variability, on the order of 10%, for the time periods 1978-2004 and 1980-2000, respectively. *Montzka et al.* [2011] attribute the high interannual variability from previous studies to large uncertainties in the emissions of MCF and CH_4 propagating through to give errors in the calculation of $[OH]^{GLOBAL}$. However, we find that different levels of variability could have existed for the two separate time periods, pre- and post-1998.

The effects of tropical widening on OH for the evaluated rates of expansion are significant. Even for the lowest rate of global tropical expansion, 0.5° $decade^{-1}$, we find that the positive perturbation to $[OH]^{GLOBAL}$ caused by tropical widening is over 25% of the negative perturbation due to CH_4. The middle estimate of Hadley cell expansion rate, 2.0° $decade^{-1}$, causes an $[OH]^{GLOBAL}$ increase nearly equal in magnitude to the reduction in $[OH]^{GLOBAL}$ due to the CH_4 sink. While the 4.5° $decade^{-1}$ rate of tropical expansion is likely much larger than any rate we will experience, it is within reason that the extent of widening simulated using this rate will one day be achieved. Our use of the 4.5° $decade^{-1}$ over the course of this 27 year analysis results in a net 12° of tropical widening globally. If the latest evaluations of global expansion rate using mean meridional streamfunction, 1.0-1.5° $decade^{-1}$ [*Davis and Rosenlof*, 2012], prove true over the course of the next century, the result would be 10-15° widening by 2100. The resulting increase in $[OH]^{GLOBAL}$ is over twice the drop in $[OH]^{GLOBAL}$ due to CH_4 for our time period; even if drawn out over the course of a century, the upper bound of the $[OH]^{GLOBAL}$ increase due to tropical widening will likely still be a significant factor. Hence, there is a need for studies of future

$[OH]^{GLOBAL}$ to strive to account for the effects of the expanding Hadley cell, which is not currently being represented in most global models, in order to fully account for the drivers of variability in $[OH]^{GLOBAL}$.

While the causes of the expansion of the Hadley circulation are still uncertain, recent studies are beginning to untangle the mechanisms behind the observed shifts in tropical boundaries. Earlier studies attributed the widening of the tropics to cooling of the stratosphere caused by increasing greenhouse gases and stratospheric O_3 depletion [*Seidel and Randel*, 2006; *Lu et al.*, 2009]. More recently, the drivers of tropical widening have been shown to be more hemispheric in nature: formation of the O_3 hole in late austral spring is widely regarded as the driver of the Southern Hemisphere tropical expansion [*Son et al.*, 2009; *Son et al.*, 2010; *Kang et al.*, 2011; *Polvani et al.*, 2011], and *Allen et al.* [2012] found tropospheric O_3 and black carbon to be likely drivers of Northern Hemisphere Hadley cell widening. *Allen et al.* [2014] has suggested that Northern Hemisphere tropical width is most directly influenced by sea surface temperatures, which are in turn forced by aerosols. If these studies are correct, then as stratospheric O_3 recovers and developed nations strive to improve air quality by reducing emissions of aerosols, it is possible that the rate of tropical widening will slow. Regardless, we show that the shifting of tropical boundaries that has occurred and will likely continue to occur to some extent has a role in affecting tropospheric levels of OH.

4.4 Conclusions

This study uses observations of total O_3 column, H_2O, and CH_4 along with an approximation of the effect of the widening of the Hadley cell to calculate values of $[OH]^{GLOBAL}$ from 1985 to 2011. While the effect of total O_3 column on $[OH]^{GLOBAL}$ is variable and produces a net ~0 change in $[OH]^{GLOBAL}$, our estimation of the effects of rising H_2O and expansion of the tropics on $[OH]^{GLOBAL}$ is large enough to offset the drop in $[OH]^{GLOBAL}$ resulting from the rise in CH_4 over this time period. This indicates the importance of including these effects in any study seeking to understand the future evolution of $[OH]^{GLOBAL}$, the lifetime of CH_4, and atmospheric composition and climate change.

Chapter 5: Conclusion

5.1 Opportunities in Tropospheric OH Research

Numerous opportunities for further research on the oxidative capacity of troposphere remain. The questions and challenges posed in Section 1.1.3 cannot be solved by any single analysis. In addition to those presented early, other questions regarding $[OH]^{GLOBAL}$ that are growing in importance include how to observationally constrain estimates of τ_{CH4} moving forward. Because MCF has been banned and its atmospheric burden has been declining precipitously, we will soon find that concentrations of MCF fall below instrument limits of detection.

The opportunity to develop the forthcoming observational metrics of $[OH]^{GLOBAL}$ presents itself now. *Liang et al.* [2015] has proposed to use interhemispheric gradients in HCFC and HFC concentrations to first evaluate emissions of the compounds, then determine their lifetimes and values of $[OH]^{GLOBAL}$. Given the increased interest in these compounds [*Velders et al.*, 2012], there is a strong likelihood that widespread observations of HCFCs and HFCs will be available to make this endeavor possible. Additionally, the radioisotope ^{14}CO has been used to infer OH abundances in the past, though on limited spatial and temporal scales due to lack of observations [*Manning et al.*, 2005]. The suggestion that the measurement of ^{14}CO has recently become "practical" [*Manning et al.*, 2005] may result in more widespread adoption of this observation over more regular time intervals; if that is the case, then ^{14}CO may also pose a valid alternative to MCF.

Evaluation of these and perhaps other methods of observationally constraining τ_{CH4} is one research topic that is presently ready to be undertaken.

Another prime opportunity to make strides in the scientific understanding of $[OH]^{GLOBAL}$ exists in an upcoming field campaign. The Atmospheric Tomography (ATom) project [*NOAA*, 2014], designed to sample background atmospheric conditions and understand the processes controlling the short-term climate forcers O_3, CH_4, and black carbon, was recently funded under NASA's Earth Venture call for proposals. The NASA DC-8 aircraft will conduct transects up and down the Pacific and Atlantic Oceans with extensive vertical profiling for each of 4 seasons over a 4-year period starting at the end of 2016. Measurements will consist of over 100 distinct chemical, aerosol, radiative, and physical variables. The temporal and spatial scales over which the experiment will be conducted are unprecedented, and the chemical payload that will be equipped will enable observational constraint of τ_{CH4} in ways that were never before possible. Both OH and HO_2 will be measured on-board, as will be O_3, H_2O, CO, NO_x, numerous hydrocarbons, spectral actinic flux, and nearly every other variable that influences OH.

While ATom holds great promise for the science that will be conducted with the resulting data set, the selection of this campaign also indicates the recognition that OH and mean tropospheric composition are priority research topics within the atmospheric community. For such a large-scale project to be competitively-selected indicates the shared value of the scientific objectives targeted by the proposal. As a result, scientific interest in the research topic of $[OH]^{GLOBAL}$ will likely continue far into the future.

5.2 Outstanding Questions in the Science of Tropospheric OH

Research opportunities clearly abound for studying $[OH]^{GLOBAL}$ and τ_{CH4}; however, several outstanding questions remain that are not so straightforward to address. The first is simply, what is the true value of τ_{CH4}? Disagreement between model evaluations and MCF-based calculations of τ_{CH4} suggest that either the models are biased low or the MCF analysis is biased high. However, our use of data collected during the CONTRAST campaign in the tropical Western Pacific suggests that models are actually overestimating τ_{CH4}. While this conclusion may apply to too small a spatial and temporal scale to meaningfully evaluate $[OH]^{GLOBAL}$, it still raises the question of which estimate of τ_{CH4} represents the true atmosphere, and for what reasons is the other estimate biased?

The second outstanding question with which the atmospheric chemistry community will have to grapple is, how will OH burdens change in the future? As stratospheric O_3 levels recover following the decline in atmospheric halogen burdens [*Oman et al.*, 2010], $J(O^1D)$ will decrease, causing a relative decrease in OH concentrations. On the other hand, as many countries strive to improve air quality, atmospheric burdens of CO will likely see a decrease. Reducing the CO sink could in turn cause a rise in OH. As was demonstrated in Chapter 4, the effect of the widening of the tropics could influence a significant positive trend in OH, though the prospects for tropical widening in the future are highly uncertain. Also highly uncertain are the future emission of CH_4. The Representative Concentration Pathways (RCPs), developed to project emissions of various greenhouse gases for use in modeling forecast studies, show CH_4 concentrations plateauing at ~1500 ppb in one scenario

and increasing to ~3500 ppb in another by year 2300 [*Meinshausen et al.*, 2011]. With such large uncertainties in so many factors that affect OH chemistry, a wide scope of approaches should be taken to model future $[OH]^{GLOBAL}$.

Section 1.1.3 presented previous work that reveals practically no level of agreement between models in how $[OH]^{GLOBAL}$ will evolve over the next century [*Voulgarakis et al.*, 2013]. Without an understanding of present-day τ_{CH4} or of its recent trends, the path forward may seem bleak. However, selection of major efforts, such as ATom, to add significant observational constraint to our knowledge of present-day τ_{CH4} will do much to propel the science forward. From there, methodical, observation-based attribution of the factors driving variations in $[OH]^{GLOBAL}$ can be made, and careful diagnosis of model processes can follow. Only at this point will future projections of the oxidizing capacity of the troposphere be truly meaningful.

Bibliography

Abram, J. P., D. J. Creasey, D. E. Heard, J. D. Lee, and M. J. Pilling (2000), Hydroxyl radical and ozone measurements in England during the solar eclipse of 11 August 1999, *Geophys Res Lett*, *27*(21), 3437-3440, doi:10.1029/2000gl012164.

Allen, R. J., J. R. Norris, and M. Kovilakam (2014), Influence of anthropogenic aerosols and the Pacific Decadal Oscillation on tropical belt width, *Nature Geosci*, *7*(4), 270-274, doi:10.1038/ngeo2091.

Allen, R. J., S. C. Sherwood, J. R. Norris, and C. S. Zender (2012), Recent Northern Hemisphere tropical expansion primarily driven by black carbon and tropospheric ozone, *Nature*, *485*(7398), 350-354, doi:10.1038/nature11097.

Allison, T. C. (2015), Application of an Artificial Neural Network to the Prediction of OH Radical Reaction Rate Constants for Evaluating Global Warming Potential, *J Phys Chem B*, doi:10.1021/acs.jpcb.5b09558.

Anderson, D. C., et al. (2016), A pervasive role for biomass burning in tropical high ozone/low water structures, *Nature Commun*, *7*, doi:10.1038/ncomms10267.

Apel, E. C., A. J. Hills, R. Lueb, S. Zindel, S. Eisele, and D. D. Riemer (2003), A fast-GC/MS system to measure C-2 to C-4 carbonyls and methanol aboard aircraft, *J Geophys Res-Atmos*, *108*(D20), 17, doi:10.1029/2002jd003199.

Archer, C. L., and K. Caldeira (2008), Historical trends in the jet streams, *Geophys Res Lett*, *35*(8), 6, doi:10.1029/2008gl033614.

Aschmann, J., B. M. Sinnhuber, E. L. Atlas, and S. M. Schauffler (2009), Modeling the transport of very short-lived substances into the tropical upper troposphere and lower stratosphere, *Atmos Chem Phys*, *9*(23), 9237-9247.

Ashfold, M. J., N. R. P. Harris, E. L. Atlas, A. J. Manning, and J. A. Pyle (2012), Transport of short-lived species into the Tropical Tropopause Layer, *Atmos Chem Phys*, *12*(14), 6309-6322, doi:10.5194/acp-12-6309-2012.

Atkinson, R. (1987), A Structure-Activity Relationship for the Estimation of Rate Constants for the Gas-Phase Reactions of OH Radicals with Organic-Compounds, *Int J Chem Kinet*, *19*(9), 799-828, doi:10.1002/kin.550190903.

Atkinson, R., and A. C. Lloyd (1984), Evaluation of kinetic and mechanistic data for modeling of photochemical smog, *J Phys Chem Ref Data*, *13*(2), 315-444.

Bell, M. L., F. Dominici, and J. M. Samet (2005), Meta-analysis of ozone and mortality, *Epidemiology*, *16*(5), S35-S35, doi:10.1097/00001648-200509000-00075.

Berntsen, T. K., I. S. A. Isaksen, G. Myhre, J. S. Fuglestvedt, F. Stordal, T. A. Larsen, R. S. Freckleton, and K. P. Shine (1997), Effects of anthropogenic emissions on tropospheric ozone and its radiative forcing, *J Geophys Res-Atmos*, *102*(D23), 28101-28126, doi:10.1029/97jd02226.

Birner, T. (2010), Recent widening of the tropical belt from global tropopause statistics: Sensitivities, *J Geophys Res*, *115*(D23), doi:10.1029/2010jd014664.

Bousquet, P., D. A. Hauglustaine, P. Peylin, C. Carouge, and P. Ciais (2005), Two decades of OH variability as inferred by an inversion of atmospheric transport and chemistry of methyl chloroform, *Atmos Chem Phys*, *5*, 2635-2656.

Brioude, J., R. W. Portmann, J. S. Daniel, O. R. Cooper, G. J. Frost, K. H. Rosenlof, C. Granier, A. R. Ravishankara, S. A. Montzka, and A. Stohl (2010), Variations in ozone depletion potentials of very short-lived substances with season and emission region, *Geophys Res Lett*, *37*, 5, doi:10.1029/2010gl044856.

Brune, W. H., et al. (1998), Airborne in-situ OH and HO2 observations in the cloud-free troposphere and lower stratosphere during SUCCESS, *Geophys Res Lett*, *25*(10), 1701-1704.

Butchart, N., and A. A. Scaife (2001), Removal of chlorofluorocarbons by increased mass exchange between the stratosphere and troposphere in a changing climate, *Nature*, *410*(6830), 799-802, doi:10.1038/35071047.

Butchart, N., et al. (2006), Simulations of anthropogenic change in the strength of the Brewer-Dobson circulation, *Climate Dynamics*, *27*(7-8), 727-741, doi:10.1007/s00382-006-0162-4.

Canty, T. P., L. Hembeck, T. P. Vinciguerra, D. C. Anderson, D. L. Goldberg, S. F. Carpenter, D. J. Allen, C. P. Loughner, R. J. Salawitch, and R. R. Dickerson (2015), Ozone and NOx chemistry in the eastern US: evaluation of CMAQ/CB05 with satellite (OMI) data, *Atmos Chem Phys*, *15*(19), 10965-10982, doi:10.5194/acp-15-10965-2015.

Carpenter, L. J. a. S. R. L. A., J. B. Burkholder, C. Clerbaux, B. D. Hall, R. Hossaini, J. C. Laube, and S. A. Yvon-Lewis (2014), Ozone-Depleting Substances (ODSs) and Other Gases of Interest to the Montreal Protocol, Chapter 1 in Scientific Assessment of Ozone Depletion: 2014*Rep.*, World Meteorological Organization, Geneva, Switzerland.

Cazorla, M., G. M. Wolfe, S. A. Bailey, A. K. Swanson, H. L. Arkinson, and T. F. Hanisco (2015), A new airborne laser-induced fluorescence instrument for in situ detection of formaldehyde throughout the troposphere and lower stratosphere, *Atmos Meas Tech*, *8*(2), 541-552, doi:10.5194/amt-8-541-2015.

Chameides, W. L., R. W. Lindsay, J. Richardson, and C. S. Kiang (1988), The role of biogenic hydrocarbons in urban photochemical smog - atlanta as a case-study, *Science*, *241*(4872), 1473-1475, doi:10.1126/science.3420404.

Claeys, M., et al. (2004), Formation of secondary organic aerosols through photooxidation of isoprene, *Science*, *303*(5661), 1173-1176, doi:10.1126/science.1092805.

Crosson, E. R. (2008), A cavity ring-down analyzer for measuring atmospheric levels of methane, carbon dioxide, and water vapor, *Appl Phys B-Lasers O*, *92*(3), 403-408, doi:10.1007/s00340-008-3135-y.

Crounse, J. D., F. Paulot, H. G. Kjaergaard, and P. O. Wennberg (2011), Peroxy radical isomerization in the oxidation of isoprene, *Phys Chem Chem Phys*, *13*(30), 13607-13613, doi:10.1039/c1cp21330j.

Davis, S. M., and K. H. Rosenlof (2012), A Multidiagnostic Intercomparison of Tropical-Width Time Series Using Reanalyses and Satellite Observations, *J. Clim.*, *25*(4), 1061-1078, doi:10.1175/jcli-d-11-00127.1.

Dlugokencky, E. J., et al. (2009), Observational constraints on recent increases in the atmospheric CH4burden, *Geophys Res Lett*, *36*(18), doi:10.1029/2009gl039780.

Duncan, B., D. Portman, I. Bey, and C. Spivakovsky (2000), Parameterization of OH for efficient computation in chemical tracer models, *J Geophys Res-Atmos*, *105*(D10), 12259-12262, doi:10.1029/1999jd901141.

Duncan, B. N., S. E. Strahan, Y. Yoshida, S. D. Steenrod, and N. Livesey (2007), Model study of the cross-tropopause transport of biomass burning pollution, *Atmos Chem Phys*, *7*(14), 3713-3736.

Ellingsen, K., et al. (2008), Global ozone and air quality: a multi-model assessment of risks to human health and crops, *Atmos. Chem. Phys. Discuss.*, *8*(1), 2163-2223, doi:10.5194/acpd-8-2163-2008.

Elshorbany, Y. F., et al. (2012), HOx budgets during HOxComp: A case study of HOx chemistry under NOx-limited conditions, *J Geophys Res-Atmos*, *117*, 16, doi:10.1029/2011jd017008.

Emmerson, K. M., and M. J. Evans (2009), Comparison of tropospheric gas-phase chemistry schemes for use within global models, *Atmos Chem Phys*, *9*(5), 1831-1845, doi:10.5194/acp-9-1831-2009.

Emmons, L. K., et al. (2015), The POLARCAT Model Intercomparison Project (POLMIP): overview and evaluation with observations, *Atmos Chem Phys*, *15*(12), 6721-6744, doi:10.5194/acp-15-6721-2015.

EPA (2015), National Ambient Air Quality Standards (NAAQS), available at http://www3.epa.gov/ttn/naaqs/criteria.html.

Fahey, D. W., et al. (1993), Insitu measurements constraining the role of sulfate aerosols in midlatitude ozone depletion, *Nature*, *363*(6429), 509-514, doi:10.1038/363509a0.

Fernandez, R. P., R. J. Salawitch, D. E. Kinnison, J. F. Lamarque, and A. Saiz-Lopez (2014), Bromine partitioning in the tropical tropopause layer: implications for stratospheric injection, *Atmos Chem Phys*, *14*(24), 13391-13410, doi:10.5194/acp-14-13391-2014.

Fiore, A. M., et al. (2009), Multimodel estimates of intercontinental source-receptor relationships for ozone pollution, *J Geophys Res-Atmos*, *114*, 21, doi:10.1029/2008jd010816.

Forster, P. a. V. R. C. L. A., et al. (2007), Changes in Atmospheric Constituents and in Radiative Forcing. In: Climate Change 2007: The Physical Science Basis. Contribution of Working Group I to the Fourth Assessment Report of the Intergovernmental Panel on Climate Change [Solomon, S., D. Qin, M. Manning, Z. Chen, M. Marquis, K.B. Averyt, M.Tignor and H.L. Miller (eds.)]*Rep.*, Cambridge, United Kingdom and New York, NY, USA.

Frith, S. M., N. A. Kramarova, R. S. Stolarski, R. D. McPeters, P. K. Bhartia, and G. J. Labow (2014), Recent changes in total column ozone based on the SBUV Version 8.6 Merged Ozone Data Set, *J Geophys Res-Atmos*, *119*(16), 9735-9751, doi:10.1002/2014jd021889.

Fu, Q., C. M. Johanson, J. M. Wallace, and T. Reichler (2006), Enhanced mid-latitude tropospheric warming in satellite measurements, *Science*, *312*(5777), 1179-1179, doi:10.1126/science.1125566.

Fu, Q., and P. Lin (2011), Poleward Shift of Subtropical Jets Inferred from Satellite-Observed Lower-Stratospheric Temperatures, *J. Clim.*, *24*(21), 5597-5603, doi:10.1175/jcli-d-11-00027.1.

Fueglistaler, S., H. Wernli, and T. Peter (2004), Tropical troposphere-to-stratosphere transport inferred from trajectory calculations, *J Geophys Res-Atmos*, *109*(D3), 16, doi:10.1029/2003jd004069.

Galloway, J. N., G. E. Likens, and M. E. Hawley (1984), Acid precipitation - natural versus anthropogenic components, *Science*, *226*(4676), 829-831, doi:10.1126/science.226.4676.829.

Gao, R. S., K. H. Rosenlof, D. W. Fahey, P. O. Wennberg, E. J. Hintsa, and T. F. Hanisco (2014), OH in the tropical upper troposphere and its relationships to solar radiation and reactive nitrogen, *J Atmos Chem*, *71*(1), 55-64, doi:10.1007/s10874-014-9280-2.

Garcia, R. R., and W. J. Randel (2008), Acceleration of the Brewer-Dobson circulation due to increases in greenhouse gases, *J. Atmos. Sci.*, *65*(8), 2731-2739, doi:10.1175/2008jas2712.1.

Gardner, M. W., and S. R. Dorling (1998), Artificial neural networks (the multilayer perceptron) - A review of applications in the atmospheric sciences, *Atmos. Environ.*, *32*(14-15), 2627-2636, doi:10.1016/s1352-2310(97)00447-0.

Gerbig, C., S. Schmitgen, D. Kley, A. Volz-Thomas, K. Dewey, and D. Haaks (1999), An improved fast-response vacuum-UV resonance fluorescence CO instrument, *J Geophys Res-Atmos*, *104*(D1), 1699-1704, doi:10.1029/1998jd100031.

Gettelman, A., P. H. Lauritzen, M. Park, and J. E. Kay (2009), Processes regulating short-lived species in the tropical tropopause layer, *J Geophys Res-Atmos*, *114*, 14, doi:10.1029/2009jd011785.

Guenther, A. B., P. R. Zimmerman, P. C. Harley, R. K. Monson, and R. Fall (1993), Isoprene and monoterpene emission rate variability - model evaluations and sensitivity analyses, *J Geophys Res-Atmos*, *98*(D7), 12609-12617, doi:10.1029/93jd00527.

Hanisco, T. F., et al. (2001), Sources, sinks, and the distribution of OH in the lower stratosphere, *J Phys Chem A*, *105*(9), 1543-1553, doi:10.1021/jp002334g.

Hatsushika, H., and K. Yamazaki (2003), Stratospheric drain over Indonesia and dehydration within the tropical tropopause layer diagnosed by air parcel trajectories, *J Geophys Res-Atmos*, *108*(D19), 13, doi:10.1029/2002jd002986.

Hauglustaine, D. A., and G. P. Brasseur (2001), Evolution of tropospheric ozone under anthropogenic activities and associated radiative forcing of climate, *J Geophys Res-Atmos*, *106*(D23), 32337-32360, doi:10.1029/2001jd900175.

Hauglustaine, D. A., J. Lathiere, S. Szopa, and G. A. Folberth (2005), Future tropospheric ozone simulated with a climate-chemistry-biosphere model, *Geophys Res Lett*, *32*(24), L24807, doi:10.1029/2005gl024031.

Heard, D. E., and M. J. Pilling (2003), Measurement of OH and HO2 in the troposphere, *Chemical Reviews*, *103*(12), 5163-5198, doi:10.1021/cr020522s.

Heaton, J. (2011), Introduction to the math of neural networks, edited, Heaton Research, Inc., St. Louis.

Hoffmann, T., J. R. Odum, F. Bowman, D. Collins, D. Klockow, R. C. Flagan, and J. H. Seinfeld (1997), Formation of organic aerosols from the oxidation of biogenic hydrocarbons, *J. Atmos. Chem.*, *26*(2), 189-222, doi:10.1023/a:1005734301837.

Hofmann, D. J., and S. Solomon (1989), Ozone destruction through heterogeneous chemistry following the eruption of el chichon, *J Geophys Res-Atmos*, *94*(D4), 5029-5041, doi:10.1029/JD094iD04p05029.

Horii, C. V., J. W. Munger, S. C. Wofsy, M. Zahniser, D. Nelson, and J. B. McManus (2006), Atmospheric reactive nitrogen concentration and flux budgets at a Northeastern US forest site, *Agricultural and Forest Meteorology*, *136*(3-4), 159-174, doi:10.1016/j.agrformet.2006.03.005.

Hossaini, R., M. P. Chipperfield, W. Feng, T. J. Breider, E. Atlas, S. A. Montzka, B. R. Miller, F. Moore, and J. Elkins (2012), The contribution of natural and anthropogenic very short-lived species to stratospheric bromine, *Atmos Chem Phys*, *12*(1), 371-380, doi:10.5194/acp-12-371-2012.

Houghton, J. T., e. al., and (Eds.) (1996), Climate Change 1995. The science of climate change, *Cambridge University Press, UK*, 572.

Hu, Y., and Q. Fu (2007), Observed poleward expansion of the Hadley circulation since 1979, *Atmos Chem Phys*, *7*(19), 5229-5236.

Hudson, R. D., M. F. Andrade, M. B. Follette, and A. D. Frolov (2006), The total ozone field separated into meteorological regimes - Part II: Northern Hemisphere mid-latitude total ozone trends, *Atmos Chem Phys*, *6*, 5183-5191.

Hudson, R. D., A. D. Frolov, M. F. Andrade, and M. B. Follette (2003), The total ozone field separated into meteorological regimes. Part I: defining the regimes, *J. Atmos. Sci.*, *60*(14), 1669-1677, doi:10.1175/1520-0469(2003)060<1669:ttofsi>2.0.co;2.

IPCC (2001), Climate Change 2001: The Scientific Basis, *Rep.*, Cambridge University Press, Cambridge, UK.

IPCC (2013), Climate Change 2013: The Physical Science Basis, *Rep.*, Cambridge University Press, Cambridge, UK.

Jacob, D. J. (1999), Introduction to Atmospheric Chemistry, edited, p. Chapter 11, Princeton University Press, Princeton, New Jersey.

Jacob, D. J., et al. (1996), Origin of ozone and NOx in the tropical troposphere: A photochemical analysis of aircraft observations over the South Atlantic basin, *J Geophys Res-Atmos*, *101*(D19), 24235-24250, doi:10.1029/96jd00336.

Jaeglé, L., D. J. Jacob, W. H. Brune, D. Tan, I. C. Faloona, A. J. Weinheimer, B. A. Ridley, T. L. Campos, and G. W. Sachse (1998), Sources of HOx and production of ozone in the upper troposphere over the United States, *Geophys Res Lett*, *25*(10), 1709-1712.

Jain, A. K., J. C. Mao, and K. M. Mohiuddin (1996), Artificial neural networks: A tutorial, *Computer*, *29*(3), 31-+, doi:10.1109/2.485891.

Jenkin, M. E., S. M. Saunders, and M. J. Pilling (1997), The tropospheric degradation of volatile organic compounds: A protocol for mechanism development, *Atmos. Environ.*, *31*(1), 81-104, doi:10.1016/s1352-2310(96)00105-7.

Jenkin, M. E., J. C. Young, and A. R. Rickard (2015), The MCM v3.3 degradation scheme for isoprene, *Atmos. Chem. Phys. Discuss.*, *15*(6), 9709-9766, doi:10.5194/acpd-15-9709-2015.

Johanson, C. M., and Q. Fu (2009), Hadley Cell Widening: Model Simulations versus Observations, *J. Clim.*, *22*(10), 2713-2725, doi:10.1175/2008jcli2620.1.

Johnson, C. E., W. J. Collins, D. S. Stevenson, and R. G. Derwent (1999), Relative roles of climate and emissions changes on future tropospheric oxidant concentrations, *J Geophys Res-Atmos*, *104*(D15), 18631-18645, doi:10.1029/1999jd900204.

Kang, S. M., L. M. Polvani, J. C. Fyfe, and M. Sigmond (2011), Impact of Polar Ozone Depletion on Subtropical Precipitation, *Science*, *332*(6032), 951-954, doi:10.1126/science.1202131.

Kovacs, T. A., and W. H. Brune (2001), Total OH loss rate measurement, *J. Atmos. Chem.*, *39*(2), 105-122, doi:10.1023/a:1010614113786.

Krol, M., and J. Lelieveld (2003), Can the variability in tropospheric OH be deduced from measurements of 1,1,1-trichloroethane (methyl chloroform)?, *J Geophys Res-Atmos*, *108*(D3), 11, 4125, doi:10.1029/2002jd002423.

Kruger, K., and B. Quack (2013), Introduction to special issue: the TransBrom Sonne expedition in the tropical West Pacific, *Atmos Chem Phys*, *13*(18), 9439-9446, doi:10.5194/acp-13-9439-2013.

Lamarque, J. F., et al. (2012), CAM-chem: description and evaluation of interactive atmospheric chemistry in the Community Earth System Model, *Geoscientific Model Development*, *5*(2), 369-411, doi:10.5194/gmd-5-369-2012.

Lang, C., D. W. Waugh, M. A. Olsen, A. R. Douglass, Q. Liang, J. E. Nielsen, L. D. Oman, S. Pawson, and R. S. Stolarski (2012), The impact of greenhouse gases on past changes in tropospheric ozone, *J Geophys Res-Atmos*, *117*, 13, doi:10.1029/2012jd018293.

Lary, D. J., L. A. Remer, D. MacNeill, B. Roscoe, and S. Paradise (2009), Machine Learning and Bias Correction of MODIS Aerosol Optical Depth, *IEEE Geosci Remote S*, *6*(4), 694-698, doi:10.1109/lgrs.2009.2023605.

Law, K., et al. (2014), Arctic Air Pollution: New Insights From POLARCAT-IPY, edited, Bull. Amer. Meteor. Soc.

Lawrence, M. G., P. Jockel, and R. von Kuhlmann (2001), What does the global mean OH concentration tell us?, *Atmos Chem Phys*, *1*, 37-49.

Lelieveld, J., P. J. Crutzen, and F. J. Dentener (1998), Changing concentration, lifetime and climate forcing of atmospheric methane, *Tellus Ser. B-Chem. Phys. Meteorol.*, *50*(2), 128-150.

Lelieveld, J., W. Peters, F. J. Dentener, and M. C. Krol (2002), Stability of tropospheric hydroxyl chemistry, *J Geophys Res-Atmos*, *107*(D23), 11, 4715, doi:10.1029/2002jd002272.

Levy, H. (1971), Normal atmosphere - large radical and formaldehyde concentrations predicted, *Science*, *173*(3992), 141-&.

Levy, H. (1973), Tropospheric budgets for methane, carbon-monoxide, and related species, *J Geophys Res*, *78*(24), 5325-5332.

Li, F., R. S. Stolarski, and P. A. Newman (2009), Stratospheric ozone in the post-CFC era, *Atmos Chem Phys*, *9*(6), 2207-2213.

Liang, Q., E. Atlas, D. Blake, M. Dorf, K. Pfeilsticker, and S. Schauffler (2014), Convective transport of very short lived bromocarbons to the stratosphere, *Atmos Chem Phys*, *14*(11), 5781-5792, doi:10.5194/acp-14-5781-2014.

Liang, Q., M. Chipperfield, J. Daniel, J. Burkholder, M. Rigby, and G. Velders (2015), Can we use ground-based measurements of HCFCs and HFCs to

derive their emissions, lifetimes, and the global OH abundance?, paper presented at American Geophysical Union Fall Meeting, San Francisco, CA, December 14.

Logan, J. A., M. J. Prather, S. C. Wofsy, and M. B. McElroy (1981), Tropospheric Chemistry - A Global Perspective, *J Geophys Res-Oceans and Atmos*, *86*(NC8), 7210-7254, doi:10.1029/JC086iC08p07210.

Lu, J., C. Deser, and T. Reichler (2009), Cause of the widening of the tropical belt since 1958, *Geophys Res Lett*, *36*, 5, doi:10.1029/2008gl036076.

Manning, M. R., D. C. Lowe, R. C. Moss, G. E. Bodeker, and W. Allan (2005), Short-term variations in the oxidizing power of the atmosphere, *Nature*, *436*(7053), 1001-1004, doi:10.1038/nature03900.

Mao, J., et al. (2009), Airborne measurement of OH reactivity during INTEX-B, *Atmos Chem Phys*, *9*(1), 163-173.

Mao, J., et al. (2012), Insights into hydroxyl measurements and atmospheric oxidation in a California forest, *Atmos Chem Phys*, *12*(17), 8009-8020, doi:10.5194/acp-12-8009-2012.

Mao, J., S. Fan, D. J. Jacob, and K. R. Travis (2013a), Radical loss in the atmosphere from Cu-Fe redox coupling in aerosols, *Atmos Chem Phys*, *13*(2), 509-519, doi:10.5194/acp-13-509-2013.

Mao, J. Q., F. Paulot, D. J. Jacob, R. C. Cohen, J. D. Crounse, P. O. Wennberg, C. A. Keller, R. C. Hudman, M. P. Barkley, and L. W. Horowitz (2013b), Ozone and organic nitrates over the eastern United States: Sensitivity to isoprene chemistry, *J Geophys Res-Atmos*, *118*(19), 11256-11268, doi:10.1002/jgrd.50817.

Mauldin, R. L., et al. (2001), Measurements of OH aboard the NASA P-3 during PEM-Tropics B, *J Geophys Res-Atmos*, *106*(D23), 32657-32666.

McElroy, M. B., R. J. Salawitch, S. C. Wofsy, and J. A. Logan (1986), Reductions of Antarctic Ozone Due to Synergistic Interactions of Chlorine and Bromine, *Nature*, *321*(6072), 759-762, doi:10.1038/321759a0.

Meinshausen, M., et al. (2011), The RCP greenhouse gas concentrations and their extensions from 1765 to 2300, *Climatic Change*, *109*(1-2), 213-241, doi:10.1007/s10584-011-0156-z.

Millet, D. B., et al. (2010), Global atmospheric budget of acetaldehyde: 3-D model analysis and constraints from in-situ and satellite observations, *Atmos Chem Phys*, *10*(7), 3405-3425, doi:10.5194/acp-10-3405-2010.

Mitas, C. M., and A. Clement (2005), Has the Hadley cell been strengthening in recent decades?, *Geophys Res Lett*, *32*(3), doi:10.1029/2004gl021765.

Molina, M. J., and F. S. Rowland (1974), Stratospheric sink for chlorofluoromethanes: chlorine atomc-atalysed destruction of ozone, *Nature*, *249*(5460), 810-812.

Monks, S. A., et al. (2015), Multi-model study of chemical and physical controls on transport of anthropogenic and biomass burning pollution to the Arctic, *Atmos Chem Phys*, *15*(6), 3575-3603, doi:10.5194/acp-15-3575-2015.

Montzka, S. A., M. Krol, E. Dlugokencky, B. Hall, P. Jockel, and J. Lelieveld (2011), Small Interannual Variability of Global Atmospheric Hydroxyl, *Science*, *331*(6013), 3, doi:10.1126/science.1197640.

Montzka, S. A., C. M. Spivakovsky, J. H. Butler, J. W. Elkins, L. T. Lock, and D. J. Mondeel (2000), New observational constraints for atmospheric hydroxyl on global and hemispheric scales, *Science*, *288*(5465), 500-503, doi:10.1126/science.288.5465.500.

Murray, L. T., J. A. Logan, and D. J. Jacob (2013), Interannual variability in tropical tropospheric ozone and OH: The role of lightning, *J Geophys Res-Atmos*, *118*(19), 11468-11480, doi:10.1002/jgrd.50857.

Naik, V., et al. (2013), Preindustrial to present-day changes in tropospheric hydroxyl radical and methane lifetime from the Atmospheric Chemistry and Climate Model Intercomparison Project (ACCMIP), *Atmos Chem Phys*, *13*(10), 5277-5298, doi:10.5194/acp-13-5277-2013.

Newell, R. E., and S. Gould-Stewart (1981), A Stratospheric Fountain?, *J. Atmos. Sci.*, *38*(12), 2789-2796, doi:10.1175/1520-0469(1981)038<2789:asf>2.0.co;2.

Newton, R., G. Vaughan, H. M. A. Ricketts, L. L. Pan, A. J. Weinheimer, and C. Chemel (2015), Ozonesonde profiles from the West Pacific Warm Pool, *Atmos. Chem. Phys. Discuss.*, *15*(12), 16655-16696, doi:10.5194/acpd-15-16655-2015.

Nicely, J. M., et al., *in preparation*, (2016a), Quantifying The Causes of Differences in Tropospheric OH within Global Models, *J Geophys Res*.

Nicely, J. M., et al., *in preparation*, (2016b), An Observationally Constrained Evaluation of the Oxidative Capacity in the Tropical Western Pacific, *J Geophys Res*.

NOAA (2014), ATom selected for funding under the NASA EVS-2 program, edited, NOAA Earth System Research Laboratory News and Events, available at http://www.esrl.noaa.gov/csd/news/2014/160_1125.html

Olson, J. R. (2004), Testing fast photochemical theory during TRACE-P based on measurements of OH, HO2, and CH2O, *J Geophys Res*, *109*(D15), doi:10.1029/2003jd004278.

Oman, L. D., et al. (2010), Multimodel assessment of the factors driving stratospheric ozone evolution over the 21st century, *J Geophys Res-Atmos*, *115*, D24306, doi:10.1029/2010jd014362.

Pan, L. L., et al., submitted (2016), The CONvective TRansport of Active Species in the Tropics (CONTRAST) Experiment, *B Am Meteorol Soc*.

Pan, L. L., et al. (2015), Bimodal distribution of free tropospheric ozone over the tropical western Pacific revealed by airborne observations, *Geophys Res Lett*, *42*(18), 7844-7851, doi:10.1002/2015gl065562.

Pan, L. L., W. J. Randel, B. L. Gary, M. J. Mahoney, and E. J. Hintsa (2004), Definitions and sharpness of the extratropical tropopause: A trace gas perspective, *J Geophys Res-Atmos*, *109*(D23), 11, doi:10.1029/2004jd004982.

Patra, P. K., et al. (2014), Observational evidence for interhemispheric hydroxyl-radical parity, *Nature*, *513*(7517), 219-223, doi:10.1038/nature13721.

Plumb, A. R., R. S. Stolarski (lead authors), M. I. Hegglin, M. J. Prather, and C. M. Volk (2013), The Theory of Estimating Lifetimes Using Models and Observations, Chapter 2 in Lifetimes of Stratospheric Ozone-Depleting Substances, Their Replacements, and Related Species, *Rep.*

Polvani, L. M., D. W. Waugh, G. J. P. Correa, and S.-W. Son (2011), Stratospheric Ozone Depletion: The Main Driver of Twentieth-Century Atmospheric Circulation Changes in the Southern Hemisphere, *J. Clim.*, *24*(3), 795-812, doi:10.1175/2010jcli3772.1.

Prather, M., et al. (2001), Atmospheric chemistry and greenhouse gases, in *Climate Change 2001: The Scientific Basis. Contribution of Working Group I to the Third Assessment Report of the Intergovernmental Panel on Climate Change*, edited by J. T. Houghton et al., edited, pp. 239-287, Cambridge Univ. Press, Cambridge, U.K.

Prather, M. J., C. D. Holmes, and J. Hsu (2012), Reactive greenhouse gas scenarios: Systematic exploration of uncertainties and the role of atmospheric chemistry, *Geophys Res Lett*, *39*, 5, doi:10.1029/2012gl051440.

Prather, M. J., and D. J. Jacob (1997), A persistent imbalance in HOx and NOx photochemistry of the upper troposphere driven by deep tropical convection, *Geophys Res Lett*, *24*(24), 3189-3192, doi:10.1029/97gl03027.

Prinn, R. G., et al. (2005), Evidence for variability of atmospheric hydroxyl radicals over the past quarter century, *Geophys Res Lett*, *32*(7), 4, doi:10.1029/2004gl022228.

Raub, J. A., M. Mathieu-Nolf, N. B. Hampson, and S. R. Thom (2000), Carbon monoxide poisoning - a public health perspective, *Toxicology*, *145*(1), 1-14, doi:10.1016/s0300-483x(99)00217-6.

Rex, M., et al. (2014), A tropical West Pacific OH minimum and implications for stratospheric composition, *Atmos Chem Phys*, *14*(9), 4827-4841, doi:10.5194/acp-14-4827-2014.

Ridley, B. A., and F. E. Grahek (1990), A small, low flow, high-sensitivity reaction vessel for NO chemiluminescence detectors, *J Atmos Ocean Tech*, *7*(2), 307-311, doi:10.1175/1520-0426(1990)007<0307:aslfhs>2.0.co;2.

Rienecker, M. M., et al. (2008), The GEOS-5 Data Assimilation System - Documentation of Versions 5.0.1, 5.1.0, and 5.2.0*Rep.*, 1-118 pp.

Rudolph, J. (1995), The tropospheric distribution and budget of ethane, *J Geophys Res-Atmos*, *100*(D6), 11369-11381, doi:10.1029/95jd00693.

Salawitch, R. J., et al. (2010), A new interpretation of total column BrO during Arctic spring, *Geophys Res Lett*, *37*(21), n/a-n/a, doi:10.1029/2010gl043798.

Salawitch, R. J., et al. (1994), The distribution of hydrogen, nitrogen, and chlorine radicals in the lower stratosphere - implications for changes in O_3 due to emission of NO_y from supersonic aircraft, *Geophys Res Lett*, *21*(23), 2547-2550, doi:10.1029/94gl02781.

Sander, S. P., et al. (2011), Chemical Kinetics and Photochemical Data for Use in Atmospheric Studies, Evaluation No. 17*Rep.*, Jet Propulsion Laboratory, Pasadena, CA.

Saunders, S. M., K. J. Hughes, M. J. Pilling, D. L. Baulch, and P. I. Smurthwaite (1993), *Reactions of Hydroxyl Radicals with Selected Hydrocarbons of Importance in Atmospheric Chemistry*, 88-99 pp., Spie - Int Soc Optical Engineering, Bellingham, doi:10.1117/12.140209.

Saunders, S. M., M. E. Jenkin, R. G. Derwent, and M. J. Pilling (2003), Protocol for the development of the Master Chemical Mechanism, MCM v3 (Part A):

tropospheric degradation of non-aromatic volatile organic compounds, *Atmos Chem Phys*, *3*, 161-180.

Seidel, D. J., Q. Fu, W. J. Randel, and T. J. Reichler (2008), Widening of the tropical belt in a changing climate, *Nature Geosci*, *1*(1), 21-24, doi:10.1038/ngeo.2007.38.

Seidel, D. J., and W. J. Randel (2006), Variability and trends in the global tropopause estimated from radiosonde data, *J Geophys Res-Atmos*, *111*(D21), D21101, doi:10.1029/2006jd007363.

Seidel, D. J., and W. J. Randel (2007), Recent widening of the tropical belt: Evidence from tropopause observations, *J Geophys Res-Atmos*, *112*(D20), D20113, doi:10.1029/2007jd008861.

Shetter, R. E., and M. Muller (1999), Photolysis frequency measurements using actinic flux spectroradiometry during the PEM-Tropics mission: Instrumentation description and some results, *J Geophys Res-Atmos*, *104*(D5), 5647-5661, doi:10.1029/98jd01381.

Shindell, D. T., et al. (2006), Multimodel simulations of carbon monoxide: Comparison with observations and projected near-future changes, *J Geophys Res-Atmos*, *111*(D19), 24, doi:10.1029/2006jd007100.

Singh, H. B. (1977), Atmospheric halocarbons - evidence in favor of reduced average hydroxyl radical concentration in troposphere, *Geophys Res Lett*, *4*(3), 101-104, doi:10.1029/GL004i003p00101.

Singh, H. B., et al. (2004), Analysis of the atmospheric distribution, sources, and sinks of oxygenated volatile organic chemicals based on measurements over the Pacific during TRACE-P, *J Geophys Res-Atmos*, *109*(D15), 20, doi:10.1029/2003jd003883.

Singh, H. B., A. Tabazadeh, M. J. Evans, B. D. Field, D. J. Jacob, G. Sachse, J. H. Crawford, R. Shetter, and W. H. Brune (2003), Oxygenated volatile organic chemicals in the oceans: Inferences and implications based on atmospheric observations and air-sea exchange models, *Geophys Res Lett*, *30*(16), 5, doi:10.1029/2003gl017933.

Son, S.-W., N. F. Tandon, L. M. Polvani, and D. W. Waugh (2009), Ozone hole and Southern Hemisphere climate change, *Geophys Res Lett*, *36*(15), n/a-n/a, doi:10.1029/2009gl038671.

Son, S. W., et al. (2010), Impact of stratospheric ozone on Southern Hemisphere circulation change: A multimodel assessment, *J Geophys Res-Atmos*, *115*, 18, doi:10.1029/2010jd014271.

SPARC (2013), SPARC Report on Lifetimes of Stratospheric Ozone-Depleting Substances, Their Replacements, and Related Species, *Rep.*, 256 pp, SPARC Office.

Spivakovsky, C. M., et al. (2000), Three-dimensional climatological distribution of tropospheric OH: Update and evaluation, *J Geophys Res-Atmos*, *105*(D7), 8931-8980, doi:10.1029/1999jd901006.

Spivakovsky, C. M., S. C. Wofsy, and M. J. Prather (1990), A numerical-method for parameterization of atmospheric chemistry - computation of tropospheric OH, *J Geophys Res-Atmos*, *95*(D11), 18433-18439, doi:10.1029/JD095iD11p18433.

Stevenson, D. S., et al. (2006), Multimodel ensemble simulations of present-day and near-future tropospheric ozone, *J Geophys Res-Atmos*, *111*(D8), 23, doi:10.1029/2005jd006338.

Stevenson, D. S., C. E. Johnson, W. J. Collins, R. G. Derwent, and J. M. Edwards (2000), Future estimates of tropospheric ozone radiative forcing and methane turnover - the impact of climate change, *Geophys Res Lett*, *27*(14), 2073-2076, doi:10.1029/1999gl010887.

Strahan, S. E., B. N. Duncan, and P. Hoor (2007), Observationally derived transport diagnostics for the lowermost stratosphere and their application to the GMI chemistry and transport model, *Atmos Chem Phys*, *7*(9), 2435-2445.

Strode, S. A., B. N. Duncan, E. A. Yegorova, J. Kouatchou, J. R. Ziemke, and A. R. Douglass (2015), Implications of carbon monoxide bias for methane lifetime and atmospheric composition in chemistry climate models, *Atmos. Chem. Phys.*, *15*(20), 11789-11805, doi:10.5194/acp-15-11789-2015.

Tan, D., et al. (2001), OH and HO2 in the tropical Pacific: Results from PEM-Tropics B, *J Geophys Res-Atmos*, *106*(D23), 32667-32681, doi:10.1029/2001jd900002.

Taraborrelli, D., M. G. Lawrence, J. N. Crowley, T. J. Dillon, S. Gromov, C. B. M. Gross, L. Vereecken, and J. Lelieveld (2012), Hydroxyl radical buffered by isoprene oxidation over tropical forests, *Nature Geosci*, *5*(3), 190-193, doi:10.1038/ngeo1405.

UNEP (2010), Report of the 22nd Meeting of the Parties to the Montreal Protocol, Annex III, Declaration on the Global Transition Away from HCFCs and CFCs*Rep.*, UNEP, Nairobi, Kenya.

van Vuuren, D. P., et al. (2011), The representative concentration pathways: an overview, *Climatic Change*, *109*(1-2), 5-31, doi:10.1007/s10584-011-0148-z.

Velders, G. J. M., A. R. Ravishankara, M. K. Miller, M. J. Molina, J. Alcamo, J. S. Daniel, D. W. Fahey, S. A. Montzka, and S. Reimann (2012), Preserving Montreal Protocol Climate Benefits by Limiting HFCs, *Science*, *335*(6071), 922-923, doi:10.1126/science.1216414.

Vernier, J. P., et al. (2011), Major influence of tropical volcanic eruptions on the stratospheric aerosol layer during the last decade, *Geophys Res Lett*, *38*, 8, doi:10.1029/2011gl047563.

Voulgarakis, A., et al. (2013), Analysis of present day and future OH and methane lifetime in the ACCMIP simulations, *Atmos Chem Phys*, *13*(5), 2563-2587, doi:10.5194/acp-13-2563-2013.

Wennberg, P. O., T. F. Hanisco, L. Jaegle, D. J. Jacob, E. J. Hintsa, E. J. Lanzendorf, J. G. Anderson, R. S. Gao, E. R. Keim, S. G. Donnelly, L. A. Del Negro, D. W. Fahey, S. A. McKeen, R. J. Salawitch, C. R. Webster, R. D. May, R. L. Herman, M. H. Proffitt, J. J. Margitan, E. L. Atlas, S. M. Schauffler, F. Flocke, C. T. McElroy, T. P. Bui (1998), Hydrogen radicals, nitrogen radicals, and the production of O_3 in the upper troposphere, *Science*, *279*(5347), 49-53, doi:10.1126/science.279.5347.49.

Wennberg, P. O. (2006), Atmospheric chemistry - Radicals follow the sun, *Nature*, *442*(7099), 145-146, doi:10.1038/442145a.

Wennberg, P. O., S. Peacock, J. T. Randerson, and R. Bleck (2004), Recent changes in the air-sea gas exchange of methyl chloroform, *Geophys Res Lett*, *31*(16), L16112, doi:10.1029/2004gl020476.

Wiedinmyer, C., S. K. Akagi, R. J. Yokelson, L. K. Emmons, J. A. Al-Saadi, J. J. Orlando, and A. J. Soja (2011), The Fire INventory from NCAR (FINN): a high resolution global model to estimate the emissions from open burning, *Geoscientific Model Development*, *4*(3), 625-641, doi:10.5194/gmd-4-625-2011.

WMO (1992), International Meteorological Vocabulary*Rep. 182*, Geneva, Switzerland.

WMO (2011), Scientific Assessment of Ozone Depletion: 2010*Rep.*, 516 pp, Global Ozone Research and Monitoring Project, Geneva, Switzerland.

Wolfe, G. M., and J. A. Thornton (2011), The Chemistry of Atmosphere-Forest Exchange (CAFE) Model - Part 1: Model description and characterization, *Atmos Chem Phys*, *11*(1), 77-101, doi:10.5194/acp-11-77-2011.

Wolfe, G. M., et al. (2015), Quantifying sources and sinks of reactive gases in the lower atmosphere using airborne flux observations, *Geophys Res Lett*, *42*(19), 8231-8240, doi:10.1002/2015gl065839.

Wolter, K., and M. Timlin (1993), Monitoring ENSO in COADS with a seasonally adjusted principal component index, paper presented at 17th Climate Diagnostics Workshop, NOAA/NMC/CAC, NSSL, Oklahoma Clim. Survey, CIMMS and the School of Meteor., Univ. of Oklahoma, Norman, OK, 01/1993.

Wolter, K., and M. Timlin (1998), Measuring the strength of ENSO events: How does 1997/98 rank?, *Weather*, *53*(9), 315-324, doi:10.1002/j.1477-8696.1998.tb06408.x.

Worden, H. M., et al. (2013), Decadal record of satellite carbon monoxide observations, *Atmos Chem Phys*, *13*(2), 837-850, doi:10.5194/acp-13-837-2013.

Ziemke, J. R., S. Chandra, L. D. Oman, and P. K. Bhartia (2010), A new ENSO index derived from satellite measurements of column ozone, *Atmos Chem Phys*, *10*(8), 3711-3721.

Zondlo, M. A., M. E. Paige, S. M. Massick, and J. A. Silver (2010), Vertical cavity laser hygrometer for the National Science Foundation Gulfstream-V aircraft, *J Geophys Res-Atmos*, *115*, 14, doi:10.1029/2010jd014445.